

**INVESTIGATION OF THE PROTONATION SITES IN  
POLYFUNCTIONAL ANALYTES UPON ATMOSPHERIC PRESSURE  
IONIZATION IN MASS SPECTROMETRY AND STUDIES OF THE  
REACTIVITIES OF RADICALS IN THE GAS PHASE AND SOLUTION**

by

**Rashmi Kumar**

**A Dissertation**

*Submitted to the Faculty of Purdue University*

*In Partial Fulfillment of the Requirements for the degree of*

**Doctor of Philosophy**



Department of Chemistry

West Lafayette, Indiana

August 2020

**THE PURDUE UNIVERSITY GRADUATE SCHOOL  
STATEMENT OF COMMITTEE APPROVAL**

**Dr. Hilkka I. Kenttämäa, Chair**

Department of Chemistry

**Dr. Kavita Shah**

Department of Chemistry

**Dr. Julia Laskin**

Department of Chemistry

**Dr. Suzanne Bart**

Department of Chemistry

**Approved by:**

Dr. Christine A. Hrycyna

*To my beloved family,*

*Indira, Manas and Basundhara Kumar*

*You have always showed me light when there was darkness, always encouraged me to do the right thing and taught me the value of hard work and dedication*

## ACKNOWLEDGMENTS

I would like to first acknowledge my research advisor, Professor Hilkka I. Kenttämä. Her constant hard work and dedication to graduate students taught me the value of tenacity and perseverance. She taught me how to become a strong, independent and meticulous researcher. She not only guided me with my research but with great care and patience also trained me on how to effectively communicate in a clear and concise manner. My success during my doctoral program reflects her effort and dedication to teach me. She has always been very understanding and guided me during difficult times. I am sincerely grateful for her constant enthusiasm and inspiration.

Past and present Kenttämä group members have contributed greatly to my success in graduate school. First, I would like to thank Dr. John Nash for his efforts in calculations and providing me with helpful insights regarding my research. I would like to thank Dr. Joann Max for training me on different mass spectrometers. I would also like to thank Jacob Milton and Dr. Mckay Easton for teaching me calculations. I am also grateful to Leah Easterling for teaching me techniques in chromatographic separations. I would also like to thank Dr. Raghavendhar Kotha, Dr. Mckay Easton, Dr. Priya Murria, Dr. Hanyu Zhu, Dr. Yuan Jiang, Dr. Chunfen Jin, Dr. Joann Max, Laurance Cain, Dr. Ravikiran Yerabolu, Dr. Xueming Dong and Dr. John Kong for their support, mentorship and advice during the first few years in the graduate school. I have immensely enjoyed working with Jacob Milton, Yuyang Zhang, Dr. Duanchen Ding, Dr. Jeremy Manheim, Dr. Edouard Niyonsaba, Xin Ma, Dr. Katherine Wehde, Lan Xu, Dr. Zaikuan Yu, Leah Easterling, Hao-Ran Lei, Jifa Zhang, Erlu Feng, Brent Modereger, Judy Kuan-Yu Liu, Victoria Boulos, Wan Tan Jeff Zhang, Lauren Blaudeau, Jacob Guthrie, Kawthar Alzarieni, Ruth Anyaeche, Yue Fu and Wanru Li. I would like to thank all of them for being supportive and helpful.

I would like to thank Dr. Kavita Shah and Dr. Julia Laskin for their advice, help and support during my time in the graduate school. I would also like to thank Dr. Suzanne Bart for being in my committee. I am grateful to have them as my committee members.

I would also like express my sincere gratitude to my mom, dad, sister and grandparents for their unconditional love, support and encouragement. I would like to specially thank my mom who is a wonderful and strong woman herself and have always encouraged me to be independent, strong-willed and kind. Her motto “try your best and leave the rest” has kept me moving even in the most difficult times. I would also like to thank Patricia Herrera for her sincere friendship and

admirable kindness. I would like to specially thank Suyash Gupta and his family for their care and support in this journey through graduate school.

## TABLE OF CONTENTS

LIST OF TABLES .....	10
LIST OF FIGURES .....	11
ABSTRACT .....	16
CHAPTER 1. INTRODUCTION .....	17
1.1 Introduction.....	17
1.2 Thesis Overview .....	18
1.3 References.....	20
CHAPTER 2. INSTRUMENTATION AND EXPERIMENTAL DETAILS OF LINEAR QUADRUPOLE ION TRAP MASS SPECTROMETERS AND HIGH RESOLUTION ORBITRAP MASS SPECTROMETERS.....	22
2.1 Introduction.....	22
2.2 Linear Quadrupole Ion Trap (LQIT).....	23
2.2.1 Ion Source Box and API Stack .....	24
2.2.1.1 Electrospray Ionization (ESI) .....	25
2.2.1.2 Atmospheric Pressure Chemical Ionization (APCI).....	26
2.2.2 Ion Optics Region.....	27
2.2.3 Ion Trapping .....	29
2.2.4 Ion trapping in the Radial (x and y plane) .....	30
2.2.4.1 Ion Trapping in the Axial (z) Direction.....	33
2.2.4.2 Role of Helium as a Buffer Gas.....	34
2.2.5 Isolation of Ions .....	34
2.2.6 Ion Activation .....	34
2.2.7 Collision-activated Dissociation (CAD).....	36
2.2.8 Ion-molecule Reactions .....	36
2.2.9 Ion Ejection for Detection .....	38
2.2.10 Ion Detection .....	39
2.3 Orbitrap.....	40
2.3.1 Injection of Ions into the Orbitrap .....	41
2.3.2 Trajectories of Ions in the Orbitrap .....	42

2.3.3	Detection of Ions in the Orbitrap .....	43
2.4	Octupole Collision Cell.....	44
2.5	References.....	46
CHAPTER 3. EFFECTS OF RESIDUAL WATER IN A LINEAR QUADRUPOLE ION TRAP ON THE PROTONATION SITES OF 4-AMINOBENZOIC ACID.....		50
3.1	Introduction.....	50
3.2	Experimental.....	52
3.2.1	Chemicals .....	52
3.2.2	Sample Preparation.....	52
3.2.3	Instrumentation.....	53
3.2.3.1	In-Source CAD (ISCAD) .....	53
3.2.3.2	Medium-energy CAD (MCAD) (commercially known as HCD).....	53
3.2.3.3	CAD in the Ion Trap (ITCAD).....	53
3.2.3.4	Computational Studies.....	54
3.3	Results and Discussions.....	54
3.4	Conclusions.....	63
3.5	References.....	66
CHAPTER 4. THE EFFECTS OF ANALYTE CONCENTRATION ON THE PROTONATION SITES OF 4-AMINOBENZOIC ACID UPON APCI AS REVEALED BY GAS-PHASE ION- MOLECULE REACTIONS .....		69
4.1	Introduction.....	69
4.2	Experimental.....	71
4.2.1	Chemicals .....	71
4.2.2	Sample Preparation.....	71
4.2.3	Instrumentation.....	71
4.3	Results and Discussions.....	72
4.4	Conclusions.....	84
4.5	References.....	85
CHAPTER 5. MEASUREMENT OF THE PROTON AFFINITIES OF A SERIES OF MONO- AND BIRADICALS OF PYRIDINE .....		89
5.1	Introduction.....	89

5.2	Experimental .....	90
5.2.1	Chemicals .....	90
5.2.2	Sample Preparation .....	90
5.2.3	Instrumentation .....	90
5.2.3.1	Ion-Molecule Reactions in Linear Quadrupole Ion Trap .....	90
5.2.3.2	Ion-Molecule Reactions in Fourier Transform Ion Cyclotron Resonance (FT-ICR) Mass Spectrometer .....	91
5.3	Computational Methods.....	92
5.4	Results and Discussion .....	92
5.4.1	Proton Affinity Measurements for Reference Bases. ....	93
5.4.2	Proton Affinity Measurements for Monoradicals.....	100
5.4.3	Proton Affinity Measurements for Biradicals.....	103
5.4.4	Calculated Proton Affinities for Mono- and Biradicals.....	106
5.5	Conclusions.....	109
5.6	References.....	110
CHAPTER 6. COMPARISON OF SOLUTION AND GAS-PHASE REACTIONS OF 1,4-DIDEHYDROPHENAZINE BIRADICAL WITH VARIOUS NEUTRAL REAGENTS.....		113
6.1	Introduction.....	113
6.2	Experimental .....	114
6.2.1	Chemicals .....	115
6.2.2	Experimental Section.....	116
6.3	Results and Discussion .....	117
6.3.1	Reactivity of para-Benzyne Toward Tetrahydrofuran in the Gas Phase and in Solution 117	
6.3.2	Reactivity of para-Benzyne Toward Dimethyldisulfide in the Gas phase and in Solution.....	122
6.3.3	Reactivity of para-Benzyne Toward Allyl Iodide in the Gas Phase and in Solution 125	
6.4	Conclusions.....	130
6.5	References.....	131
VITA.....		135

PUBLICATIONS..... 136

## LIST OF TABLES

Table 5.1 Structures of Reference Bases 1 and 2, Proton Affinities (PA) of the bases, a $\Delta$ PA, and Proton Transfer Observations and Abundance Ratios Determined in a Linear Quadrupole Ion Trap Mass Spectrometer (LQIT).....	96
Table 5.2 . Observation of Proton Transfer Reactions between Protonated Reference Bases 1 and Neutral Reference Bases 2 (introduced into the ion trap), Both with Known PA, in the LQIT. The Ratio of the Abundance of the Protonated Reference bases 2 to the Sum of the Abundances of All Ions After All the Protonated Base 1 Had Reacted Away.....	97
Table 5.3 Structures of Reference Bases 1 and 2, Proton Affinities (PA) of the reference bases, a $\Delta$ PA, and Proton Transfer Observations Determined b in an FT-ICR Mass Spectrometer .....	100
Table 5.4. Reference Bases, Their Proton Affinities (PA) and Abundance Ratios b Determined in a LQIT. The Average of the PA Values of the Reference Bases Whose Ratios Are Given in Bold Was Averaged with the PA Value of the Reference Base Observed to Undergo a Nearly Thermoneutral Reaction ( $0.4 < \text{Ratio} < 0.6$ ; Underlined in Below Table) to Determine the Final PA (Given in Red) for Each Monoradical .....	102
Table 5.5. Structures of Reference Bases, Proton Affinities (PA) of the Bases,a Proton Transfer Observations When Using the Fourier-transform Ion Cyclotron Resonance Mass Spectrometer, b and the Linear Quadrupole Ion Trap Mass Spectrometer,c and the Final PA (in Bold Red) .....	107
Table 5.6 Calculated <sup>a,b,c</sup> Proton Affinities (PA) for Mono- and Biradicals at Different Levels of Theory and Differences Between Calculated and Experimental Values ( $\Delta$ PA).....	108

## LIST OF FIGURES

- Figure 2.1. Various components of a Thermo Scientific LQIT mass spectrometer with operational pressures (in yellow boxes) for each region of the instrument. The evacuation rates (in green boxes) of rough and turbomolecular pumps are also shown. .... 24
- Figure 2.2 A schematic of an ESI source. Analyte solution passes through the ESI needle. The N<sub>2</sub> sheath gas flows coaxially through the needle while the N<sub>2</sub> auxiliary gas flows alongside the ESI needle and converges with the sheath gas at the tip of the needle. The sheath and auxiliary gases together generate a spray plume of a fine mist of droplets. .... 25
- Figure 2.3 One of the proposed mechanisms for ESI is illustrated above. A) Large droplets exit the ESI needle and the solvent molecules keep evaporating from the droplets while they are travelling towards the inlet. B) As the droplets decrease in size, the electrostatic repulsions between the ions eventually exceeds the surface tension of the droplets, causing the droplets to break into smaller droplets. C) Solvent evaporation eventually results in the release of analyte ions from the droplet into the gas phase<sup>15</sup> ..... 26
- Figure 2.4 APCI ionization process in positive ion mode. Analyte ions are formed by reaction between solvent ions and analytes. .... 27
- Figure 2.5 Opposite rods are supplied with RF voltage of same phase whereas the voltage applied to adjacent poles is 180 ° out-of-phase<sup>19</sup> ..... 28
- Figure 2.6 A DC voltage gradient facilitates the transmission of ions in the axial direction through the ion optics region.<sup>15</sup> ..... 29
- Figure 2.7 The lengths of the front, center and back sections of the ion trap are indicated. Slits in the central electrode are also shown. .... 30
- Figure 2.8 Mathieu stability diagram describing the a and q values of the ion motion inside the trap. The circles of different colors and sizes represent ions of different m/z ratios. The ions will have stable trajectories in the overlapping regions. The unstable regions of the ions are also indicated. .... 32
- Figure 2.9 Application of three DC trapping potentials to the ion trap, one for each section, creates a potential energy well. This potential energy well regulates the axial (z-axis) motion of ions. Larger DC potential is applied to the front (DC 1) and back sections (DC 2) than to the center section (DC 3). The circles indicate ions trapped in the potential well ..... 33
- Figure 2.10 (A) Mathieu stability diagram showing ions of different m/z values with stable trajectories. (B) The RF amplitude is increased until the ion of interest (indicated using a blue circle) has a q value of 0.83 accompanied by ejection of the smallest ion (i.e., red circle) from the ion trap. (C) A tailored RF waveform is applied to the x-rods at all frequencies except for the secular frequency of the motion of the ion of interest (i.e., blue circle). The black arrow drawn from the green circle denotes an unstable trajectory when the tailored RF waveform is applied. This process results in isolation of the desired ion.<sup>15</sup> ..... 35

Figure 2.11 Inlet manifold for introduction of helium/reagent gas mixtures. The valves shown above are open to the manifold which allows the diluted reagent/helium mixture into the ion trap via a control valve. <sup>19</sup> .....	37
Figure 2.12 The Brauman double-well potential energy surface for a simple ion-molecule reaction in the gas phase. <sup>19</sup> .....	38
Figure 2.13 (A) The q values of the ions also increase with increasing main RF amplitude. (B) When the q value of the smallest ion (purple as shown above) reaches 0.88, a supplementary RF voltage is applied to the x-electrodes. The frequency of motion of the ions whose q value is 0.88 will be in resonance with the frequency of the supplementary RF voltage applied to the x-electrodes (C) These ions (purple circles) gain kinetic energy. The ions then move away from the center of the ion trap, exit via slits in the x-electrodes and strike the conversion dynode. <sup>15</sup> .....	39
Figure 2.14 Schematic of an LQIT coupled to an orbitrap mass spectrometer (Thermo LTQ-Orbitrap XL). The pressures in different areas are also indicated. The red arrows represent the ion pathways from the C-trap into the orbitrap. <sup>15</sup> .....	40
Figure 2.15 (A) Ions enter the orbitrap slightly off center (B) The electric field in the orbitrap causes ions to oscillate around and along the inner electrode. Ions with same m/z value move in tight packets (shown as thin rings). (C) The outer electrode measures the image current for the motion of the ion packets. (D) The frequency of the harmonic oscillations is proportional to the m/z value of the ions.....	41
Figure 2.16 Red line indicates the injection of ion packets into the orbitrap off-center by the C-trap. The image current produced by the axial oscillation (z-axis) of the ions is measured by the outer electrode <sup>19</sup> .....	43
Figure 2.17 (A) A DC offset potential between the C-trap and the MCAD cell accelerates ions into the MCAD cell and induces their fragmentation. (B) Typical offset potentials applied to eject ions from the MCAD cell back into the C-trap. The ions are then transferred into the orbitrap for analysis. Only transfer of ions from the linear quadrupole ion trap via the C trap into the MCAD cell and then back into the C-trap is illustrated. The black circle represents a positively charged isolated ion while the blue and orange circles represent positively charged fragment ions generated by fragmentation of the isolated ion <sup>15</sup> .....	45
Figure 3.1 ISCAD mass spectra (collision energy 30 V) measured for all the ions ionized using ESI in a) 3-1 (v/v) methanol-water and b) 1-1 (v/v) acetonitrile-water. The ions were detected using electron multipliers located outside the linear quadrupole ion trap. ....	55
Figure 3.2 High resolution MCAD mass spectra (collision energy 13 eV) recorded for protonated 4-aminobenzoic acid, ionized using ESI in a) 3-1 (v/v) methanol-water and b) 1-1 (v/v) acetonitrile-water. ....	57
Figure 3.3 ITCAD mass spectra (collision energy 30 arbitrary units) recorded for protonated 4-aminobenzoic acid, ionized using ESI in a) 3-1 (v/v) methanol-water and b) 1-1 (v/v) acetonitrile-water. Ion of m/z 77 corresponds to loss of NH <sub>3</sub> from the ion of m/z 94.....	58
Figure 3.4 ITCAD products (collision energy: 35 arbitrary units) of protonated 4-aminobenzoic acid detected by high-resolution orbitrap when using a) 3-1 (v/v) methanol-water and b) 1-1 (v/v) acetonitrile-water solvent systems. ....	59

Figure 3.5 Water and oxygen were detected in the linear quadrupole ion trap when the molecular ions of carbon dioxide (ionized using APCI) were isolated and allowed to react with residual molecules in the ion trap for 30 ms. As N <sub>2</sub> has a greater ionization energy (15.6 eV) than CO <sub>2</sub> (13.8 eV), N <sub>2</sub> in the ion trap were not detected using this method .....	60
Figure 3.6 ITCAD mass spectra (collision energy 30 arbitrary units; detection method: external electron multipliers) recorded in the presence of extra water for protonated 4-aminobenzoic acid (ionized by ESI by using a) 3-1 (v/v) methanol-water and b) 1-1 (v/v) acetonitrile-water solvent systems).....	61
Figure 3.7 Potential energy surfaces and transition state structures calculated at the M06-2X/6-311++G(d, p) level of theory for (A) loss of H <sub>2</sub> O from the O-protomer, (B) loss of CO <sub>2</sub> from the O-protomer and (C) loss of CO <sub>2</sub> from the N-protomer.....	65
Figure 4.1 MS <sup>2</sup> spectra measured after 300 ms gas-phase ion-molecule reactions between TMMS and protonated 4-aminobenzoic acid (dissolved in methanol) ionized using positive ion mode APCI. The MS/MS spectra were collected at analyte concentrations of a) 10 <sup>-9</sup> M, b) 10 <sup>-8</sup> M, c) 10 <sup>-7</sup> M, d) 10 <sup>-6</sup> M, e) 10 <sup>-5</sup> M and f) 10 <sup>-4</sup> M .....	74
Figure 4.2 Mass spectra recorded after 300 ms gas-phase ion-molecule reactions between TMMS and a) protonated benzoic acid b) protonated aniline c) protonated methyl-4-aminobenzoate and d) protonated 4-chloroaniline. The indicated ratio corresponds to the sum of the abundances of all the product ions divided by the abundance of the reactant ions after reaction time of 300 ms. ....	76
Figure 4.3 Mass spectra measured for methanol solutions of 4-aminobenzoic acid (MW 137 Da) ionized using positive ion mode APCI at concentrations of a) 10 <sup>-5</sup> M and b) 10 <sup>-4</sup> M. Ion of m/z 275 corresponds to a protonated dimer of 4-aminobenzoic acid. Ion of m/z 170 corresponds to a methanol adduct of protonated 4-aminobenzoic acid. ....	78
Figure 4.4 Possible structures of the proton-bound dimer of 4-aminobenzoic acid. O1, O2 and O3 correspond to structures where the carbonyl oxygen is protonated (calculated <sup>15</sup> to be more stable in the gas phase) while N1, N2 and N3 correspond to structures where the amino nitrogen is protonated (calculated <sup>15</sup> to be more stable in water). ....	79
Figure 4.5 a) MS <sup>3</sup> spectrum measured after isolation of the gaseous proton bound dimer ([2M+H] <sup>+</sup> ; m/z 275) of protonated 4-aminobenzoic acid formed in the ion trap followed by CAD (collision energy: 10 arbitrary units) generates protonated 4-aminobenzoic acid ([M+H] <sup>+</sup> ; m/z 138).b) Isolation of protonated 4-aminobenzoic acid (m/z 138) followed by 300 ms reactions with trimethoxymethylsilane (MS <sup>4</sup> )......	81
Figure 4.6 MS <sup>2</sup> spectra measured after the gas-phase ion-molecule reactions for 300 ms between TMMS and protonated 4-aminobenzoic acid (dissolved in 1-1 (v/v) acetonitrile-water) ionized using positive ion mode APCI. The MS/MS spectra were collected at concentrations of a) 10 <sup>-9</sup> M, b) 10 <sup>-8</sup> M, c) 10 <sup>-7</sup> M, d) 10 <sup>-6</sup> M, e) 10 <sup>-5</sup> M and f) 10 <sup>-4</sup> M .....	83
Figure 4.7 Mass spectra measured for solutions of 4-aminobenzoic acid in 1-1 (v/v) acetonitrile-water ionized using APCI for analyte concentrations a) 10 <sup>-5</sup> M and b) 10 <sup>-4</sup> M. ACN indicates acetonitrile. Ion of m/z 83 corresponds to a protonated dimer of acetonitrile.....	84

Figure 5.1 Mass spectra ( $MS^2$ ) recorded in the LQIT after (a) 500 ms and (b) 1000 ms exothermic proton transfer from protonated dimethylcarbonate to 2-methylfuran (introduced into the ion trap using manifold).....	94
Figure 5.2 Mass spectra ( $MS^2$ ) recorded in the LQIT after (a) 100 ms and (b) 600 ms endothermic proton transfer from protonated N, N-dimethylformamide to dicyclopropylketone (introduced into the ion trap through the reagent mixing manifold) .....	95
Figure 5.3 Mass spectra ( $MS^3$ ) recorded using the LQIT after (a) 30 ms and (b) 150 ms reaction of protonated 2,6-didehydropyridine with N-ethylacetamide. Proton transfer is exothermic. ....	104
Figure 5.4 Mass spectra ( $MS^3$ ) recorded using the LQIT after (a) 5 ms and (b) 10 ms reaction of protonated 2,3-didehydropyridine with N-methylformamide. Proton transfer is endothermic ..	105
Figure 6.1 Mass spectra showing gas-phase ion-molecule reaction products when protonated 1,4-didehydrophenazine biradical was allowed to react with tetrahydrofuran (introduced through manifold) for a) 1 s and b) 5 s.....	118
Figure 6.2 Figure showing mass spectra measured a) for ionized photolysis products when THF was irradiated for 30 mins, b) in dark control experiments and c) when 2,3-diethynylquinoxaline was subjected to photon-induced Bergman cyclization induced using an UV irradiation of 253 nm for 30 mins in the presence of THF .....	120
Figure 6.3 Figure showing mass spectra measured for thermally induced (60 °C) Bergman cyclization of 2,3-diethynylquinoxaline in presence of THF after a) 1 hour, b) 3 hours and c) 5 hours.....	121
Figure 6.4 Mass spectra measured after protonated 1,4-didehydrophenazine biradical was allowed to react with dimethyldisulfide for a) 1 s and b) 10 s in the gas phase.....	123
Figure 6.5 Figure showing mass spectra measured a) after DMDS was irradiated for 45 mins, b) in dark control experiments and c) after 2,3-diethynylquinoxaline was subjected to photon-induced Bergman cyclization induced using an UV irradiation of 253 nm for 45 mins in the presence of DMDS.....	124
Figure 6.6 Mass spectra measured after protonated 1,4-didehydrophenazine biradical was allowed to react with allyl iodide for a) 1 s and b) 10 s in the gas phase.....	126
Figure 6.7 Figure showing mass spectra measured a) after allyl iodide was irradiated for 30 mins, b) in dark control experiments and c) after 2,3-diethynylquinoxaline was subjected to photon-induced Bergman cyclization induced using UV irradiation of 253 nm for 30 mins in the presence of allyl iodide .....	127
Figure 6.8 Mass spectra measured after product ion of m/z 687 was subjected to CAD at a collision energy of 12 (arbitrary units) .....	128
Figure 6.9 Figure showing mass spectra measured after heat-induced (60 °C) Bergman cyclization of 2,3-diethynylquinoxaline in the presence of allyl iodide after a) 4 hours, b) 8 hours and c) 12 hours.....	128

Figure 6.10. a) Figure showing mass spectra after product ion of  $m/z$  433 obtained upon heat-induced Bergman cyclization of 2,3-diethynylquinoxaline in the presence of allyl iodide was subjected to CAD. b) Mass spectrum measured after fragment ion of  $m/z$  179 was isolated and allowed to react with allyl iodide for 10 s in the ion trap. .... 130

## ABSTRACT

High resolution tandem mass spectrometry ( $MS^n$ ) coupled with various separation techniques, such as high-performance liquid chromatography (HPLC) and gas chromatography (GC), is widely used to analyze mixtures of unknown organic compounds. In a mass spectrometric analysis, analytes of interest are at first transferred into the gas phase, ionized (protonated or deprotonated) and introduced into the instrument. Tandem mass spectrometric experiments may then be used to gain insights into structure and reactivity of the analyte ions in the gas phase. The tandem mass spectral data are often compared to those reported in external databases. However, the tandem mass spectra obtained for protonated analytes may be markedly different from those in external databases because protonation site manifested during a mass spectrometric experiment can be affected by the ionization technique, ionization solvents and condition of the ion source. This thesis focuses on investigating the effects of instrumental conditions and analyte concentrations on the protonation sites of 4-aminobenzoic acid. Reactivities of radical species were also investigated. A modified bracketing method was developed and proton affinities of a series of mono- and biradicals of pyridine were measured. In another study, a *para*-benzyne analog was generated in both solution and the gas phase and its reactivities towards various neutral reagents in the gas phase were compared to those in solution.

Chapter 2 discusses the fundamental aspects of the instruments used in this research. In chapter 3, the effects of residual moisture in linear quadrupole ion trap on the protonation sites of 4-aminobenzoic acid are considered. Chapter 4 focuses on the use of gas-phase ion-molecule reactions with trimethoxymethylsilane (TMMS) for the identification of the protonation sites of 4-aminobenzoic acid. Further, the effects of analyte concentration on the protonation sites of 4-aminobenzoic acid are considered. Chapter 5 introduces a modified bracketing method for the experimental determination of proton affinities of a series of pyridine-based mono- and biradicals. In chapter 6, successful generation of *para*-benzynes in solution is discussed. The reactivity of a *para*-benzyne analog, 1,4-didehydrophenazine, is compared to its reactivity in the gas phase.

# CHAPTER 1. INTRODUCTION

## 1.1 Introduction

Mass spectrometry (MS) is one of the most widely used analytical tools for the characterization of complex mixtures of organic compounds, such as those important in fuel research, petroleomics and pharmaceutical research.<sup>1-4</sup> Mass spectrometers have evolved tremendously over the years and are well known for their versatility, sensitivity and fast data acquisition. High-resolution mass spectrometric methods can be used for the determination of the chemical formulas of analytes. Tandem mass spectrometry ( $MS^n$ ) is one of the most commonly used techniques to obtain structural information for ionized analytes directly in mixtures. Combination of high-resolution mass spectrometry along with tandem mass spectrometry makes mass spectrometric analysis a powerful technique for characterization of unknown analytes.

A mass spectrometric analysis requires at least four steps: sample evaporation, compound ionization, ion separation and ion detection. The analyte solution is brought into the gas phase by evaporation and often is ionized nearly simultaneously. The ions are then separated according to their mass-to-charge ratios. Separation of the ions can be achieved, for example, by using a constant magnetic field that separates ions based on the frequency of ion motion, by using a flight tube that enables separation of the ions based on their flight times, or by using a scanning magnetic field that separates ions based on their momentum. Once the ions are separated, they are detected and their abundances are determined.

Commonly used  $MS^n$  approaches involve collision-activated dissociation (CAD) or ion-molecule reactions of isolated ions. In CAD experiments, the isolated ions are subjected to energetic collisions with a target gas, which lead to fragmentation of the ions. The fragment ions are then detected and analyzed for gaining structural information on the ions of interest.<sup>5,6</sup> In ion-molecule reaction experiments, isolated analyte ions of interest are allowed to react with a reagent gas to produce diagnostic reaction products. The common tandem mass spectrometers include triple quadrupole mass spectrometers, linear quadrupole ion trap mass spectrometers and Fourier-transform ion cyclotron resonance mass spectrometers. In this dissertation, a linear quadrupole ion trap (LQIT) mass spectrometer was utilized.

## 1.2 Thesis Overview

The research discussed in this thesis can be classified into three different areas: investigation of factors affecting protonation sites in polyfunctional analytes, determination of proton affinities of a series of pyridine-based mono- and biradicals, and investigation of the reactivity of a *para*-benzyne analog both in the gas phase and in solution. Chapter 2 depicts the fundamental aspects of the mass spectrometry ionization methods and instrumentation used for this research. The instruments described in chapter 2 include linear quadrupole ion traps (LQIT) and a LQIT coupled to a high-resolution orbitrap mass analyzer.

Chapter 3 discusses the effects of residual water in the ion trap of the LQIT instrument on the protonation sites of 4-aminobenzoic acid. Polyfunctional analytes, such as aminobenzoic acids, with multiple protonation sites with similar proton affinities, are often difficult to analyze accurately because the proton can reside on multiple sites and the different protomers can generate different mass spectra.<sup>7,8</sup> The most basic site of 4-aminobenzoic acid in solution is the amino nitrogen whereas calculations indicate that in the gas phase, the most basic site is the carbonyl oxygen.<sup>7</sup> Several previously published studies have demonstrated that different solvents used during electrospray ionization (ESI) can influence the manifested protonation site.<sup>7,9</sup> When 3-1 (v/v) methanol-water was used as the ionization solvent the carbonyl oxygen was the predominant site of protonation whereas when 1-1 (v/v) acetonitrile-water was used as the ionization solvent, the amino nitrogen was the predominant site of protonation.<sup>7</sup> In this study, the protonation sites of 4-aminobenzoic acid protonated via ESI were investigated using several fragmentation techniques in an LQIT/orbitrap mass spectrometer. CAD in the ion trap was observed to result in scrambling of the protonation sites, irrespective of the ionization solvents used.

Chapter 4 discusses the effect of analyte concentration on the protonation sites of 4-aminobenzoic acid using positive mode APCI as the ionization technique. A previous study demonstrated that TMMS forms stable adducts with protonated compounds with amino groups whereas it reacts with protonated compounds with carboxylic acid groups to generate an adduct that has lost a methanol molecule.<sup>10</sup> The selective reactivity of TMMS towards amino and carboxylic acid functional groups were exploited to identify the protonation sites of 4-aminobenzoic acid upon APCI. When using methanol as the ionization solvent, O-protomer was the major protomer formed at low analyte concentrations whereas N-protomer was the major protomer formed at high analyte concentrations. In contrast, when 1-1 (v/v) acetonitrile-water was

used as the ionization solvent, N-protomer was the major protomer formed, irrespective of the analyte concentration.

In chapter 5, measurement of proton affinities of a series of pyridine-based mono- and biradicals is discussed. Due to the high reactivity of radicals, traditional methods for measuring proton affinities (Cooks' kinetic method,<sup>11</sup> equilibrium method<sup>12</sup> and traditional bracketing method<sup>13,14</sup>) could not be used for this study. Hence, a modified bracketing technique was developed for both LQIT and FT-ICR mass spectrometers to determine the proton affinities based on proton transfer reactions from the protonated radicals to reference bases in the gas phase. The gas-phase proton affinity values measured are in agreement with calculated values. The proton affinity values were found to increase as the distance between the basic nitrogen atom and the radical site increased. Among the monoradicals, 4-dehydropyridine had the largest proton affinity whereas among the biradicals 3,5-didehydropyridine biradicals had the largest proton affinity.

In chapter 6, a *para*-benzyne analog (1,4-didehydrophenazine) was successfully generated both in solution and in the gas phase. In solution, 1,4-didehydrophenazine (dissolved in the compound selected as the reagent) was generated by photon-induced and heat-induced Bergman cyclization of 2,3-diethynylquinoxaline. The photon-induced Bergman cyclization was faster than the heat-induced Bergman cyclization. The generated neutral biradical was then allowed to react with reagents commonly used in gas-phase studies of radical cations: allyl iodide, dimethyldisulfide and tetrahydrofuran. The products were analyzed using off-line high-resolution tandem mass spectrometry. In the gas phase, protonated 1,4-didehydrophenazine was generated by CAD of the protonated precursor 1,4-diiodophenazine in the ion trap of the LQIT. The biradical was allowed to react with the same reagents (allyl iodide, dimethyldisulfide and tetrahydrofuran) in the gas phase. Products formed in the gas-phase ion-molecule reactions were recorded and compared to the products obtained with the same reagents in solution. Surprisingly, both tetrahydrofuran and dimethyldisulfide generated the same products both in the gas phase and the solution, in spite of the fact that the biradical was protonated in the gas phase but neutral in solution. However, allyl iodide generated different products in solution and in the gas phase.

### 1.3 References

- (1) Geoghegan, K. F.; Kelly, M. A. Biochemical Applications of Mass Spectrometry in Pharmaceutical Drug Discovery. *Mass Spectrom. Rev.* **2005**, *24* (3), 347–366. <https://doi.org/10.1002/mas.20019>.
- (2) Herrero, M.; Simó, C.; García-Cañas, V.; Ibáñez, E.; Cifuentes, A. Foodomics: MS-Based Strategies in Modern Food Science and Nutrition. *Mass Spectrom. Rev.* **2012**, *31* (1), 49–69.
- (3) Marshall, A. G.; Rodgers, R. P. Petroleomics: Chemistry of the Underworld. *Proc. Natl. Acad. Sci.* **2008**, *105* (47), 18090–18095. <https://doi.org/10.1073/pnas.0805069105>.
- (4) Richardson, S. D. Mass Spectrometry in Environmental Sciences. *Chem. Rev.* **2001**, *101* (2), 211–254. <https://doi.org/10.1021/cr990090u>.
- (5) McLuckey, S. A.; Goeringer, D. E. Special Feature: Tutorial Slow Heating Methods in Tandem Mass Spectrometry. *J. Mass Spectrom.* **1997**, *32* (5), 461–474.
- (6) Musselman, B. D. K. Busch, G. Glish and S. Mcluckey. Mass Spectrometry/Mass Spectrometry: Techniques and Applications of Tandem Mass Spectrometry, VCH Publishing, New York, 1988. Mass Spectrometry/Mass Spectrometry. *Biomed. Environ. Mass Spectrom.* **1989**, *18* (10), 942–942.
- (7) Tian, Z.; Kass, S. R. Gas-Phase versus Liquid-Phase Structures by Electrospray Ionization Mass Spectrometry. *Angew. Chem. Int. Ed.* **2009**, *48* (7), 1321–1323.
- (8) Warnke, S.; Seo, J.; Boschmans, J.; Sobott, F.; Scrivens, J. H.; Bleiholder, C.; Bowers, M. T.; Gewinner, S.; Schöllkopf, W.; Pagel, K.; von Helden, G. Protomers of Benzocaine: Solvent and Permittivity Dependence. *J. Am. Chem. Soc.* **2015**, *137* (12), 4236–4242.
- (9) Campbell, J. L.; Yang, A. M.-C.; Melo, L. R.; Hopkins, W. S. Studying Gas-Phase Interconversion of Tautomers Using Differential Mobility Spectrometry. *J. Am. Soc. Mass Spectrom.* **2016**, *27* (7), 1277–1284.
- (10) Yerabolu, R.; Kong, J.; Easton, M.; Kotha, R. R.; Max, J.; Sheng, H.; Zhang, M.; Gu, C.; Kenttämaa, H. I. Identification of Protonated Sulfone and Aromatic Carboxylic Acid Functionalities in Organic Molecules by Using Ion–Molecule Reactions Followed by Collisionally Activated Dissociation in a Linear Quadrupole Ion Trap Mass Spectrometer. *Anal. Chem.* **2017**, *89* (14), 7398–7405. <https://doi.org/10.1021/acs.analchem.7b00817>.
- (11) Cooks, R. G.; Patrick, J. S.; Kotiaho, T.; McLuckey, S. A. Thermochemical Determinations by the Kinetic Method. *Mass Spectrom. Rev.* **1994**, *13* (4), 287–339.
- (12) Meot-Ner (Mautner), M. The Proton Affinity Scale, and Effects of Ion Structure and Solvation. *Int. J. Mass Spectrom.* **2003**, *227* (3), 525–554.

- (13) Wiseman, A.; Sims, L. A.; Snead, R.; Gronert, S.; Maclagan, R. G. A. R.; Meot-Ner Mautner, M. Protonation Energies of 1-5-Ring Polycyclic Aromatic Nitrogen Heterocyclics: Comparing Experiment and Theory. *J. Phys. Chem. A* **2015**, *119* (1), 118–126.
- (14) Meot-Ner, M. Entropy-Driven Proton-Transfer Reactions. *J. Phys. Chem.* **1991**, *95* (17), 6580–6585.

## CHAPTER 2. INSTRUMENTATION AND EXPERIMENTAL DETAILS OF LINEAR QUADRUPOLE ION TRAP MASS SPECTROMETERS AND HIGH RESOLUTION ORBITRAP MASS SPECTROMETERS

### 2.1 Introduction

Mass spectrometry is a powerful and versatile analytical technique which has immense applications in the fields of proteomics<sup>1</sup>, pharmaceutical sciences<sup>2</sup>, forensics<sup>3</sup>, petroleomics<sup>4</sup> and environmental sciences.<sup>5</sup> Improvement in mass spectrometric analyses can be attributed to the rapid development of various instruments, ionization techniques and ionization methods.<sup>6-8</sup>

A complete mass spectrometric analysis involves three main steps: a) solvent evaporation and ionization, b) separation of ions based on mass to charge ratio ( $m/z$ ) and c) detection of ions. Currently used ionization techniques include electrospray ionization (ESI),<sup>9</sup> atmospheric pressure chemical ionization (APCI),<sup>10</sup> atmospheric pressure photoionization (APPI)<sup>11</sup> and field ionization (FI)<sup>12</sup>. It is crucial to choose ionization techniques that are best suited for the nature of samples to be analyzed.<sup>13</sup> Tandem mass spectrometers like linear quadrupole ion traps are equipped with MS<sup>n</sup> capabilities which can be utilized to obtain structural information on analyte ions of interest. Usually in tandem mass spectrometric experiments, ions of interest are isolated and allowed to either a) fragment by colliding with neutral gases (often nitrogen, helium or argon), a technique known as collision-activated dissociation (CAD) or b) react with neutral reagents introduced into the ion trap using home-built manifold, a technique referred to as gas-phase ion-molecule reactions. Based on the fragmentation patterns obtained in CAD experiments or the products obtained after gas-phase ion-molecule reactions, the structure and the functional groups present in analyte ions can be deduced.

There are two types of tandem mass spectrometric instruments: a) scanning mass spectrometers where steps (ion isolation and activation) leading to MS<sup>n</sup> experiments are performed in different parts of the instrument or tandem-in-space and b) trapping mass spectrometers where all the steps of MS<sup>n</sup> experiments are performed in the same region of the instrument but at different times or tandem-in-time. All the experimental studies discussed in this dissertation were performed in a trapping mass spectrometer, specifically linear quadrupole ion trap (LQIT). In some of the experiments LQIT coupled with an orbitrap was also used. The details of the instrumentation and

fundamental aspects of MS<sup>n</sup> experiments performed on this instrument are discussed later in this chapter.

## 2.2 Linear Quadrupole Ion Trap (LQIT)

One of the most widely used tandem mass spectrometers are linear quadrupole ion traps (LQIT) with versatile applications both in academia<sup>14</sup> and industries.<sup>15</sup> In the studies discussed in this dissertation a Thermo Scientific LQIT mass spectrometer was used. The schematics of the instrument used is shown in **Figure 2.1**.<sup>16</sup>

There are four major regions in LQIT:

- a) **Ion source box** which operates at 760 Torr and houses the API source (electrospray ionization (ESI) or atmospheric pressure chemical ionization (APCI) probes).
- b) **Atmospheric pressure ionization (API) stack** which is maintained at a pressure of approximately 1 Torr. This was done by using two Edwards E2M30 rotary-vane mechanical pumps with an evacuation rate of 650 L/min.
- c) **Ion optics region** which is maintained at a pressure  $0.5 - 1 \times 10^{-5}$  Torr. This was achieved by a triple ported Leybold TW220/150/15S turbomolecular pump. Evacuation rates of 25 L/s, 300 L/s and 400L/s were maintained for the first, second and third inlets respectively.
- d) **Ion trap region** which is maintained at a pressure of approximately  $1 \times 10^{-5}$  Torr by the third inlet of the turbomolecular pump. A cathode ionization gauge monitored the pressure of this region.

The different regions of LQIT and the methods of their operation are discussed in detail sequentially.

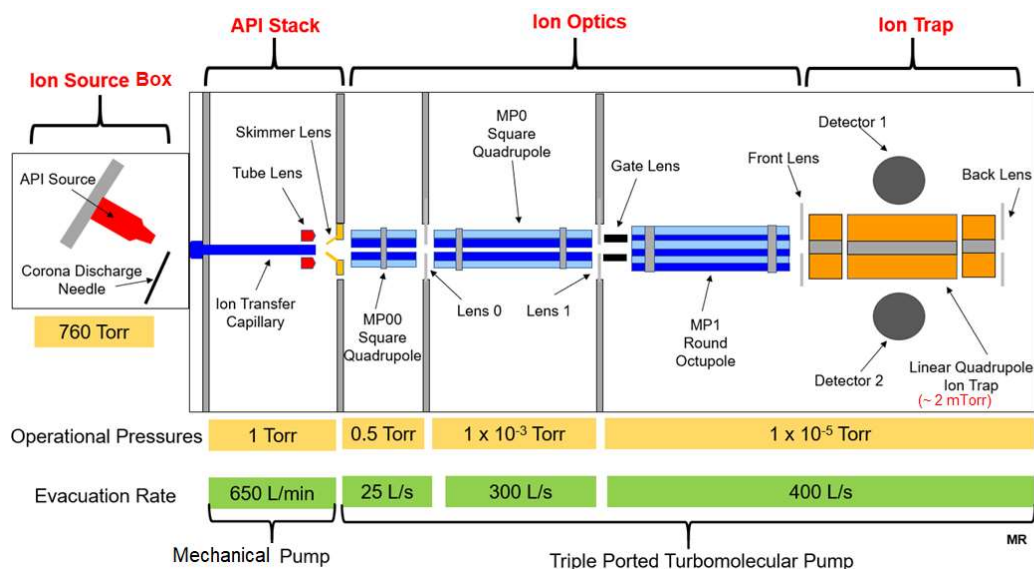


Figure 2.1. Various components of a Thermo Scientific LQIT mass spectrometer with operational pressures (in yellow boxes) for each region of the instrument. The evacuation rates (in green boxes) of rough and turbomolecular pumps are also shown.

### 2.2.1 Ion Source Box and API Stack

The ion source box is equipped with an ionization source (either an ESI or an APCI source) that facilitated the evaporation and ionization of analytes before entering the API stack. The principles and mechanisms of ESI and APCI are discussed in sections 2.2.1.1 and 2.2.1.2, respectively. After successful evaporation and ionization, the ions were guided into the ion trap by the generation of a potential difference of 0 - 20 V between the ion source box and the API stack. Nitrogen was used as sheath and auxiliary gas in order to guide the ions into the ion trap via an ion transfer capillary. The ion transfer capillary was heated to facilitate desolvation of the ions. A DC offset voltage (0 – 20V) applied to the ion transfer capillary enabled the transmission of the ions into the transfer capillary. The voltage applied to tube lens redirects these ions into the ion optics region via an off-center orifice of the skimmer cone. The skimmer cone orifice is set off-center to prevent neutral molecules from entering the ion optics region.

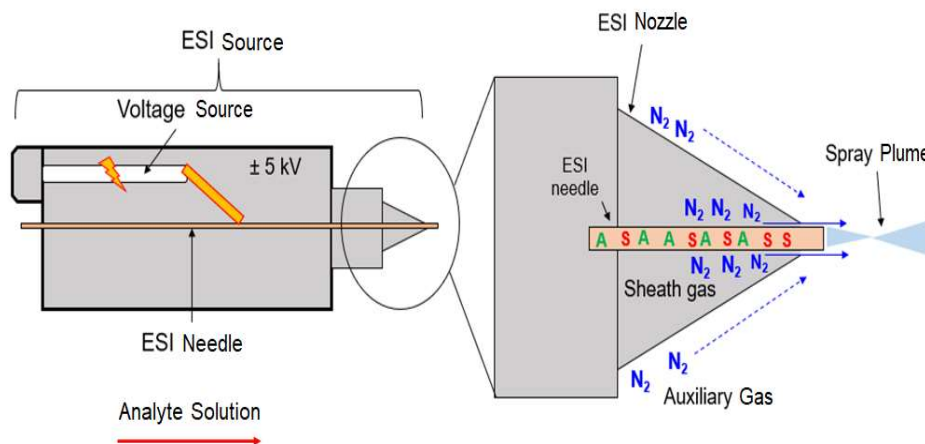


Figure 2.2 A schematic of an ESI source. Analyte solution passes through the ESI needle. The N<sub>2</sub> sheath gas flows coaxially through the needle while the N<sub>2</sub> auxiliary gas flows alongside the ESI needle and converges with the sheath gas at the tip of the needle. The sheath and auxiliary gases together generate a spray plume of a fine mist of droplets.

### 2.2.1.1 Electro spray Ionization (ESI)

ESI is one of the most widely used methods for evaporation and ionization of polar and thermally labile analytes, such as drug metabolites, peptides and proteins. John Fenn and Koichi Tanaka shared a Nobel Prize in 2002 for their development of electrospray ionization.<sup>9</sup> It is believed that in some cases, ionization may occur in the solution before introduction of the analytes into the ESI source, while in other cases, the ionization occurs during the ESI process.<sup>17</sup> All ESI sources are equipped with capillary needle. The analyte solutions are passed through the needle and sprayed as a plume (**Figure 2.2**). The mechanism of ESI is still under debate, however, one of the most commonly accepted mechanisms can be described as follows. A voltage of 1 – 5 kV applied to the tip of the needle generates charges on the surface of droplets. The droplets move towards the inlet of the mass spectrometer following the vacuum drag. The solvent evaporates during this process, generating smaller droplets. Shrinking of the droplet size increases the charge density on the surface of the droplets. The charge density increases on the droplet surface until the repulsive electrostatic forces exceed the surface tension of the solvent. This causes the droplet to divide into smaller droplets.<sup>18</sup> This process occurs repeatedly until the volume of the droplets becomes extremely small and the increased electrostatic repulsion between the ionized analytes causes ejection of the ionized analytes from the droplets into the gas phase (**Figure 2.3**).

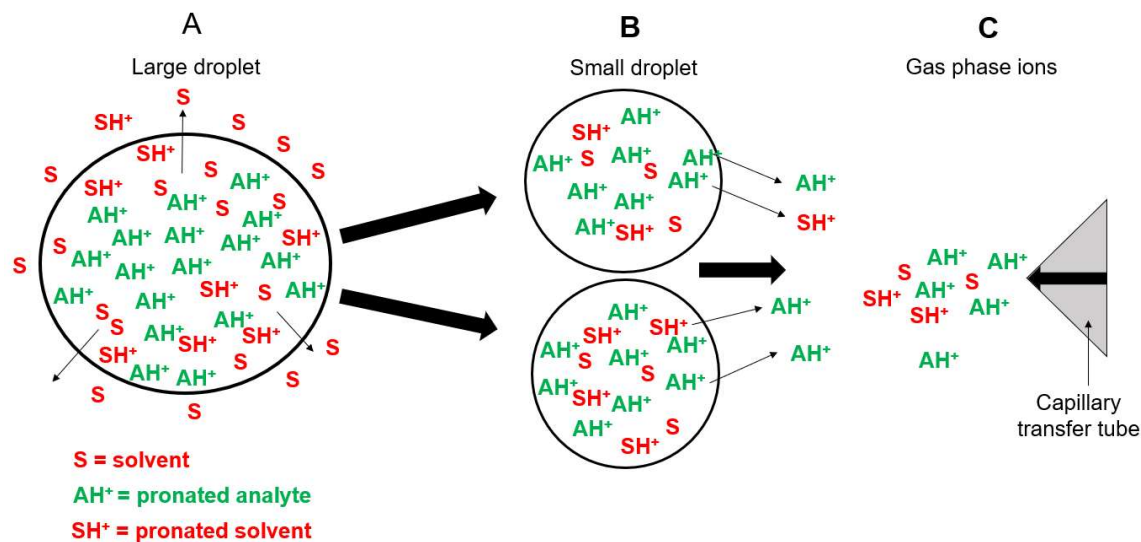


Figure 2.3 One of the proposed mechanisms for ESI is illustrated above. A) Large droplets exit the ESI needle and the solvent molecules keep evaporating from the droplets while they are travelling towards the inlet. B) As the droplets decrease in size, the electrostatic repulsions between the ions eventually exceeds the surface tension of the droplets, causing the droplets to break into smaller droplets. C) Solvent evaporation eventually results in the release of analyte ions from the droplet into the gas phase<sup>15</sup>

### 2.2.1.2 Atmospheric Pressure Chemical Ionization (APCI)

APCI is one of the most widely used methods for the evaporation/ionization of non-volatile, nonpolar analytes, such as hydrocarbons and other analytes that are not efficiently evaporated and ionized by ESI. APCI is predominantly believed to follow a gas-phase ionization mechanism.<sup>13</sup>

An APCI source is usually equipped with a capillary usually held at a temperature of 300 – 500 °C. N<sub>2</sub> is commonly used as the sheath and auxiliary gases that are blown through or outside the capillary, respectively. Analyte solutions are introduced into the capillary. The sheath and auxiliary gases also act as nebulization gases. In the presence of a nebulization gas a mist of fine droplets of analyte and solvent molecules are formed near the corona discharge needle (**Figure 2.4**).<sup>19</sup> The corona discharge needle is usually maintained at a potential of 2.0 – 4.0 kV which ionizes the nebulization gas (N<sub>2</sub>) to produce primary ions (N<sub>2</sub><sup>+</sup>). These primary ions undergo a complex series of reactions to generate protonated solvent molecules, as shown in **Scheme 2.1** for water. The solvent ions react with analyte molecules to form protonated analyte molecules. A schematic showing the cascade of ion-molecule reactions initiated by the corona discharge to generate analyte ions is shown in **Scheme 2.1**.<sup>20</sup>

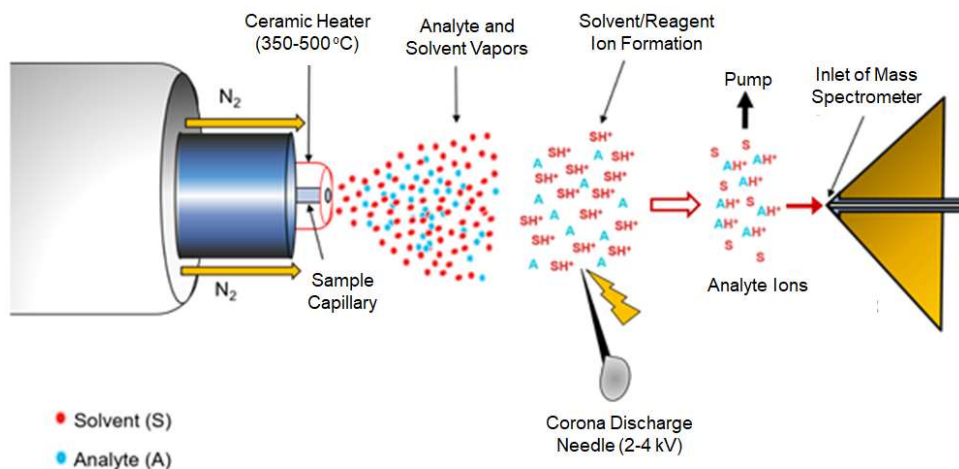
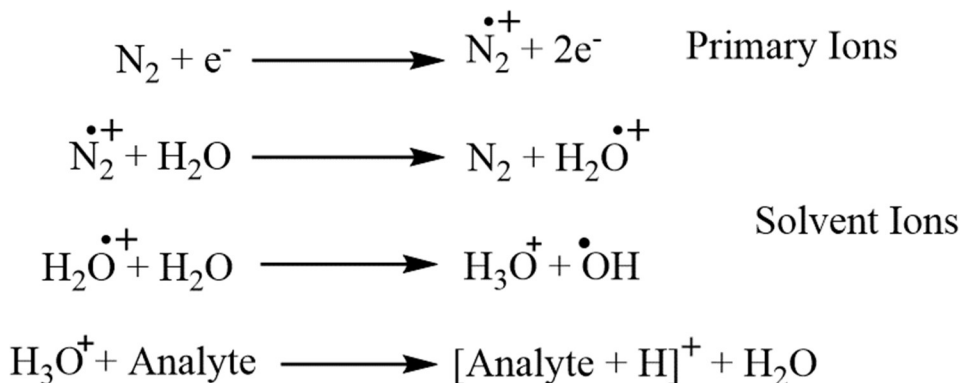


Figure 2.4 APCI ionization process in positive ion mode. Analyte ions are formed by reaction between solvent ions and analytes.



Scheme 2.1 Mechanism for the generation of protonated analytes in positive ion mode when using water as a solvent in APCI ionization.

### 2.2.2 Ion Optics Region

The ions generated in the API source are then moved into the API stack which enables transfer and desolvation of the ions on their way to the ion optics region. After exiting the API stack, the ions enter the ion optics region and pass through four lenses (lens 0, lens 1, gate lens and front lens) without contacting any of the solid internal parts of the mass spectrometer. A DC voltage applied to each lens, along with an RF voltage, enable focusing of the ions through several ion guides. The ion guides are referred to as MP00, MP0 and MP1. MP00 and MP0 are square quadrupole ion guides while Q1 is a round-rod octupole ion guide (**Figure 2.6**).<sup>21</sup> RF frequency

applied to the opposite poles of the electrodes restrict the motion of the ions in the x-and y-direction. Adjacent rods in the multipole are supplied with an rf-voltage with the same amplitude and frequency but the opposite rods are supplied with an rf-voltage that is  $180^\circ$  out of phase (**Figure 2.5**). This generates an oscillating RF field between the rods, causing ions to move in a circular oscillatory fashion.

Lenses in between the ion guides facilitate ion to transfer from one ion guide into another. Ions exiting multipole Q00 have almost zero kinetic energy in the z-direction due to the high pressure in this region. A DC potential gradient created by applying different DC voltages to the ion guides accelerate the ions and facilitates the transfer of the ions towards the ion trap. Figure 2.6 shows a typical DC potential gradient applied to the ion guides.

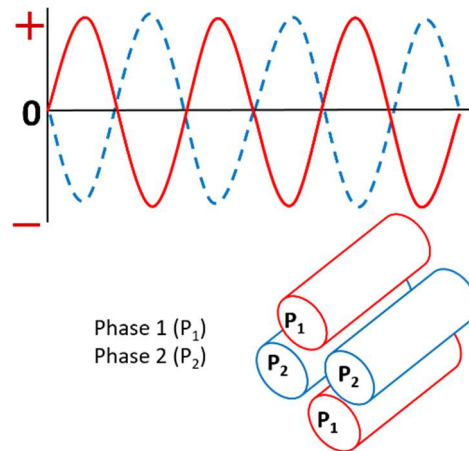


Figure 2.5 Opposite rods are supplied with RF voltage of same phase whereas the voltage applied to adjacent poles is  $180^\circ$  out-of-phase <sup>19</sup>

### 2.2.3 Ion Trapping

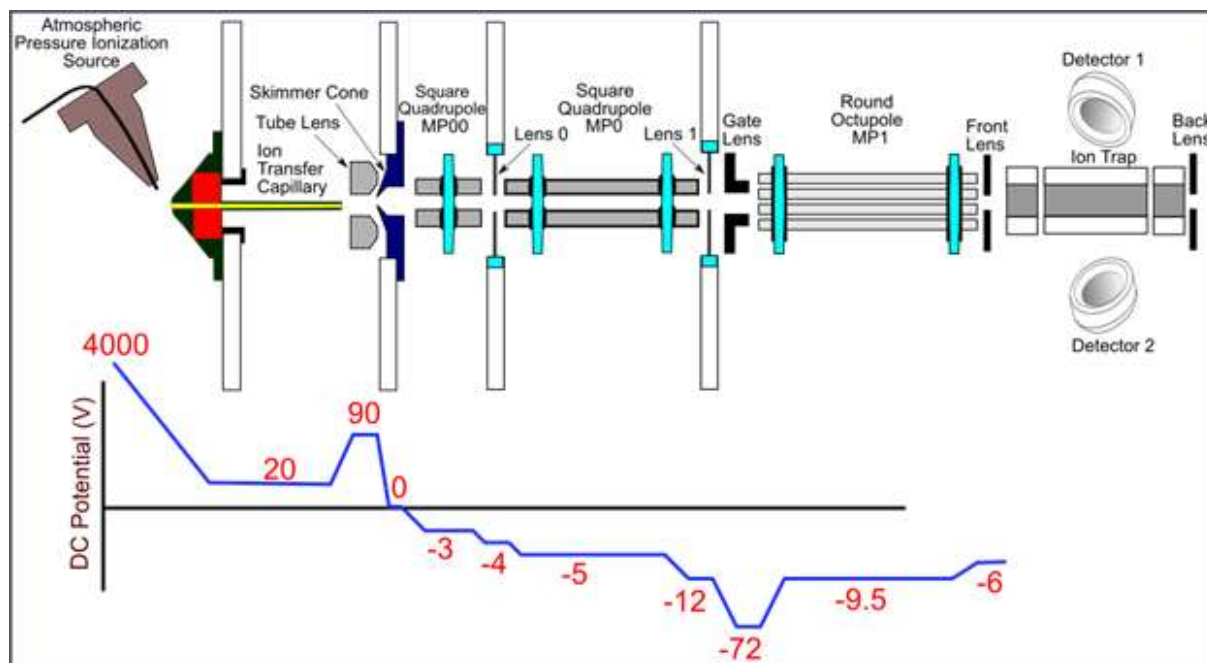


Figure 2.6 A DC voltage gradient facilitates the transmission of ions in the axial direction through the ion optics region.<sup>15</sup>

The ion trap is comprised of four hyperbolic electrodes and two lenses, one in the front and one in the back. The hyperbolic electrodes are partitioned into three sections (front, center and back). The central electrodes contain slits to allow ejection of ions for detection (**Figure 2.7**). Ions enter the ion trap via the front lens. RF voltages of the same frequency and amplitude are applied to opposite electrodes while RF voltages 180 ° out of phase are applied to adjacent electrodes. This allows trapping of ions in the x-y direction (radial motion). DC voltages applied to the front, back and center parts of the electrodes (DC1, DC2 and DC3) enables trapping of the ions axially. The use of helium as a buffer gas cooled the ions and restricted the ions' motion to the center of the ion trap. The details of the ion trapping are discussed below.

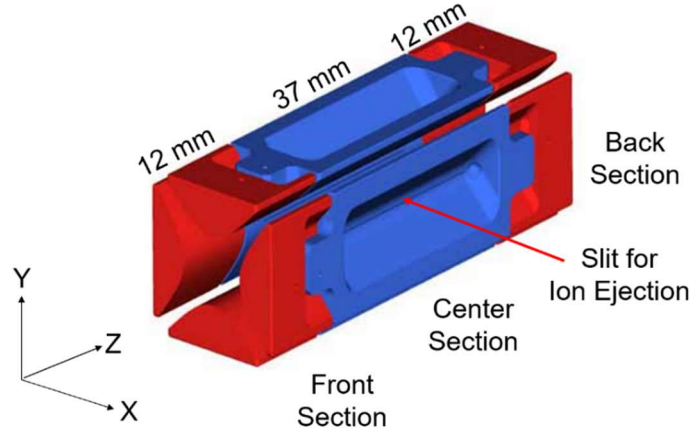


Figure 2.7 The lengths of the front, center and back sections of the ion trap are indicated. Slits in the central electrode are also shown.

#### 2.2.4 Ion trapping in the Radial (x and y plane)

A quadrupolar potential is generated by applying RF and DC potentials to the front, center and back parts of all the electrodes. This quadrupolar potential trapped the ions in the radial direction in the quadrupole ion trap.<sup>22</sup> The quadrupolar potential ( $\Phi$ ) can be defined as

$$\Phi = \Phi_0 (\lambda x^2 + \sigma y^2 + \gamma z^2) / r_0^2 \quad (2.1)$$

where  $\Phi_0$  is the applied electric potential,  $\lambda$ ,  $\sigma$  and  $\gamma$  are the weighing constants for  $x$ ,  $y$  and  $z$  coordinates respectively and  $r_0$  is a constant. The value of  $r_0$  depends upon whether the quadrupole was a mass filter or an ion trap. All differential equations within an electrical field must satisfy the Laplace transform.<sup>22</sup> Hence the following equation for the weighing constants must be valid:

$$\lambda + \sigma + \gamma = 0 \quad (2.2)$$

In the case of a LQIT,  $\lambda = \sigma = 1$  while  $\gamma = -2$ .<sup>22</sup> Substituting the values of these constants, equation 2.1 can be written as

$$\Phi_{x,y,z} = \Phi_0 (x^2 + y^2 - 2z^2) / r_0^2 \quad (2.3)$$

Utilizing the standard transformations  $x = r \cos\theta$ ,  $y = r \sin\theta$  and  $z = z$ , equation 2.3 can be expressed as

$$\Phi_{r,z} = \Phi_0 (r^2 \cos^2\theta + r^2 \sin^2\theta - 2z^2) / r_0^2 \quad (2.4)$$

After applying the trigonometric identity  $\cos^2\theta + \sin^2\theta = 1$ , equation 2.4 can be redefined as<sup>22</sup>

$$\Phi_{r,z} = \Phi_0 (r^2 - 2z^2) / r_0^2 \quad (2.5)$$

The quadrupolar potential  $\Phi_0$  depends on the RF potential ( $V \cos \Omega t$ , where  $V$  is the amplitude of the RF voltage with an angular frequency of  $\Omega$ , expressed in  $\text{rad s}^{-1}$ ) and the DC potential ( $U$  where  $U$  is the DC voltage). Hence  $\Phi_0$  can be expressed as

$$\pm \Phi_0 = \pm (U - V \cos \Omega t) \quad (2.6)$$

Substituting  $\Phi_0$ , defined by equation 2.6 into equation 2.3, followed by differentiating with respect to  $x$ , the quadrupole potential becomes

$$\frac{\delta \Phi}{\partial x} = \frac{2x}{r_0^2} (U + V \cos \Omega t) \quad (2.7)$$

Therefore, the forces exerted upon an ion (with mass  $m$  and charge  $z$ ) in the  $x$ - and  $y$ -directions within a quadrupolar field can be expressed as

$$F_x = m \frac{d^2 x}{dt^2} = -ze \frac{d\Phi}{dx} \quad (2.8)$$

$$F_y = m \frac{d^2 y}{dt^2} = -ze \frac{d\Phi}{dy} \quad (2.9)$$

where  $e$  corresponds to the charge of an electron ( $1.602 \times 10^{-19}$  Coulombs).

Substituting equation 2.7 into equation 2.8, the force experienced by the ion in the  $x$ -direction can be written as

$$\frac{d^2 x}{dt^2} + \frac{2ze}{mr_0^2} (U - V \cos \Omega t)x = 0 \quad (2.10)$$

Similarly, in the  $y$ -direction the force can be redefined as<sup>23,24</sup>

$$\frac{d^2 y}{dt^2} + \frac{2ze}{mr_0^2} (U - V \cos \Omega t)y = 0 \quad (2.11)$$

The motion of ions and their stable trajectories in LQIT can be defined using equations 2.10 and 2.11, which resemble the Mathieu equation shown below:

$$\frac{d^2 u}{d\xi^2} + (a_u + 2q_u \cos 2\xi)u = 0 \quad (2.12)$$

where parameter  $\xi$  can be defined as

$$\xi = \frac{\Omega t}{2} \quad (2.13)$$

Substituting parameter  $\xi$  in equations 2.10 and 2.11, the following Mathieu expressions result:

$$q_u = q_x = (-)q_y = \frac{4zeV}{mr_0^2 \Omega^2} \quad (2.14)$$

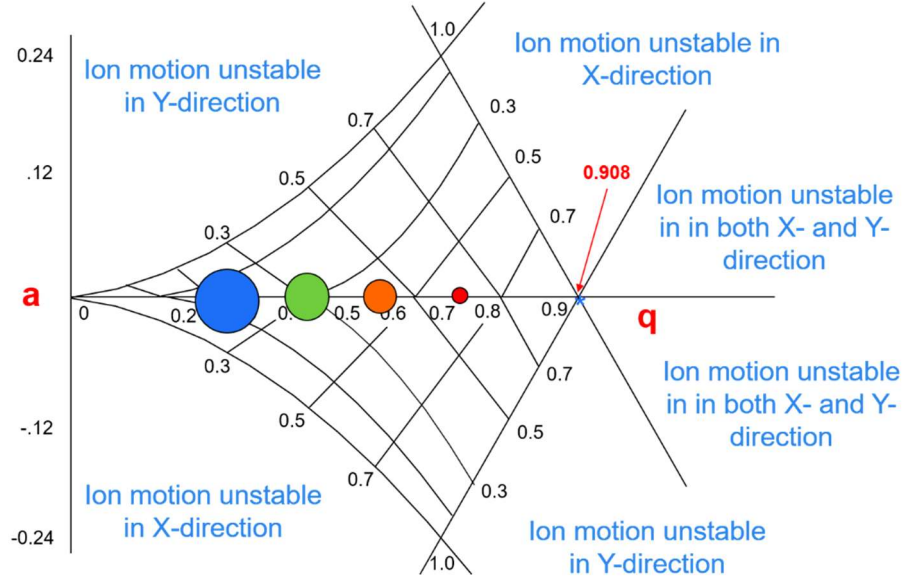


Figure 2.8 Mathieu stability diagram describing the  $a$  and  $q$  values of the ion motion inside the trap. The circles of different colors and sizes represent ions of different  $m/z$  ratios. The ions will have stable trajectories in the overlapping regions. The unstable regions of the ions are also indicated.

$$a_u = a_x = (-)a_y = \frac{8zeU}{mr_o^2\Omega^2} \quad (2.15)$$

where  $q_u$  and  $a_u$  are Mathieu stability parameters, describing the motion of the ion and the stabilities of the ion motions inside LQIT. As evident from equations 2.14 and 2.15, the mass of the ion is inversely proportional to the Mathieu stability parameters  $q_u$  and  $a_u$ .

The stability region of Mathieu stability diagram is shown in **Figure 2.8**. Any ions with a and  $q$  values within this region will have stable trajectories in LQIT whereas the ions with a and  $q$  values outside this region will have unstable trajectories and cannot be trapped. When  $a_u$  is set to 0, the motion of the ions in the ion trap can be manipulated by varying the RF potential amplitude, which in turn increases the  $q_u$  values. When the value of  $q_u$  reaches 0.908, the trajectories of the ions in both x- and y-directions become unstable, leading to ejection of the ions. It is noteworthy that since the mass of the ions and  $q_u$  are inversely proportional to each other, ions are ejected in the order of increasing  $m/z$  values, with the ions of lowest  $m/z$  values ejected first.

In LQIT each ion oscillates at a particular frequency ( $\omega_u$ ) and this frequency can be expressed by the following equation:

$$\omega_u = \frac{\beta_u\Omega}{2} \quad (2.16)$$

Where  $\Omega$  is the angular frequency of the RF frequency applied to the rods of the ion trap,  $\beta_u$  is the Dehmelt approximation<sup>25</sup> for  $q_u$  values less than 0.4.  $\beta_u$  can be expressed as:

$$\beta_u = \sqrt{\left(a_u + \frac{1}{2}q_u^2\right)} \quad (2.17)$$

As evident from equation 2. 17, the maximum value for  $\beta_u$  is 1. Hence the maximum plausible secular frequency for an ion is half of the RF angular frequency ( $\Omega$ ) applied to the electrodes. It is noteworthy that the secular frequency of ion motion is directly proportional to its  $q_u$  value and inversely proportional to its  $m/z$  value. Hence ions with smaller  $m/z$  values have larger  $q_u$  values and oscillate at higher secular frequencies compared to ions with larger  $m/z$  values.

### 2.2.4.1 Ion Trapping in the Axial (z) Direction

DC voltages applied to the front, back and center parts of the electrodes (DC1, DC2 and DC3) enables trapping of the ions axially (**Figure 2.10**). A low DC potential applied to DC1 and DC2 enables the ions to enter the ion trap. The ions are then confined axially in the ion trap by

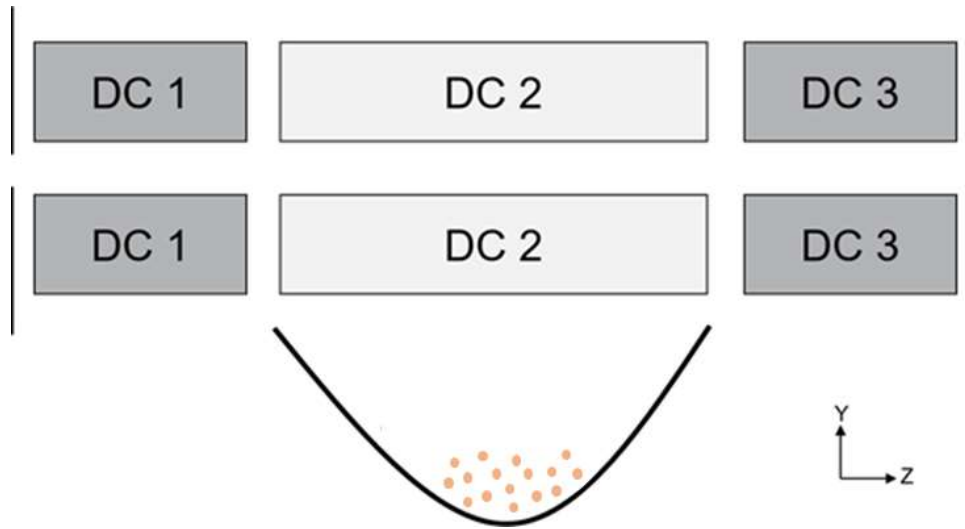


Figure 2.9 Application of three DC trapping potentials to the ion trap, one for each section, creates a potential energy well. This potential energy well regulates the axial (z-axis) motion of ions. Larger DC potential is applied to the front (DC 1) and back sections (DC 2) than to the center section (DC 3). The circles indicate ions trapped in the potential well

raising the DC potentials of the front and back electrodes (D1 and D3, respectively). A lower potential applied to the central electrode D2 creates a potential energy well that enables trapping of the ions into the center of the ion trap in the z-direction (**Figure 2.9**).

#### **2.2.4.2 Role of Helium as a Buffer Gas**

Helium was used as a buffer gas inside the ion trap. Ions undergo frictional collisions with helium, which decreases the kinetic energy of the isolated ions and localizes the ions into the center of the ion trap in z-direction. This process increases the sensitivity of the analysis.<sup>26</sup>

#### **2.2.5 Isolation of Ions**

Ion isolation is the first step of tandem mass spectrometry experiments ( $MS^n$ ). Ion isolation involves trapping the ion of interest while ejecting all other ions from the ion trap. Ions of specific  $m/z$  values oscillate at their unique frequencies, as discussed above, which is exploited to eject unwanted ions from the ion trap. First, the RF amplitude is increased in such a manner that the ion of interest has a  $q_u$  value of 0.803. This results in ions of lower  $m/z$  values to be ejected due to their higher  $q_u$  values (**Figure 2.10**).<sup>15</sup> A dipolar excitation with frequencies 5 – 500 kHz (except the frequency corresponding to the ion of interest) is then applied to the x-electrodes. This process results in successful ejection of all other ions but the ion of interest.

#### **2.2.6 Ion Activation**

After ion isolation, the q-value of the isolated ion is adjusted to 0.25 by changing the amplitude of the main RF field. Then a supplementary RF potential with a frequency equal to the secular frequency of the isolated ions is applied to the x- electrodes. This causes dipolar excitation and acceleration of the isolated ions.<sup>24</sup>

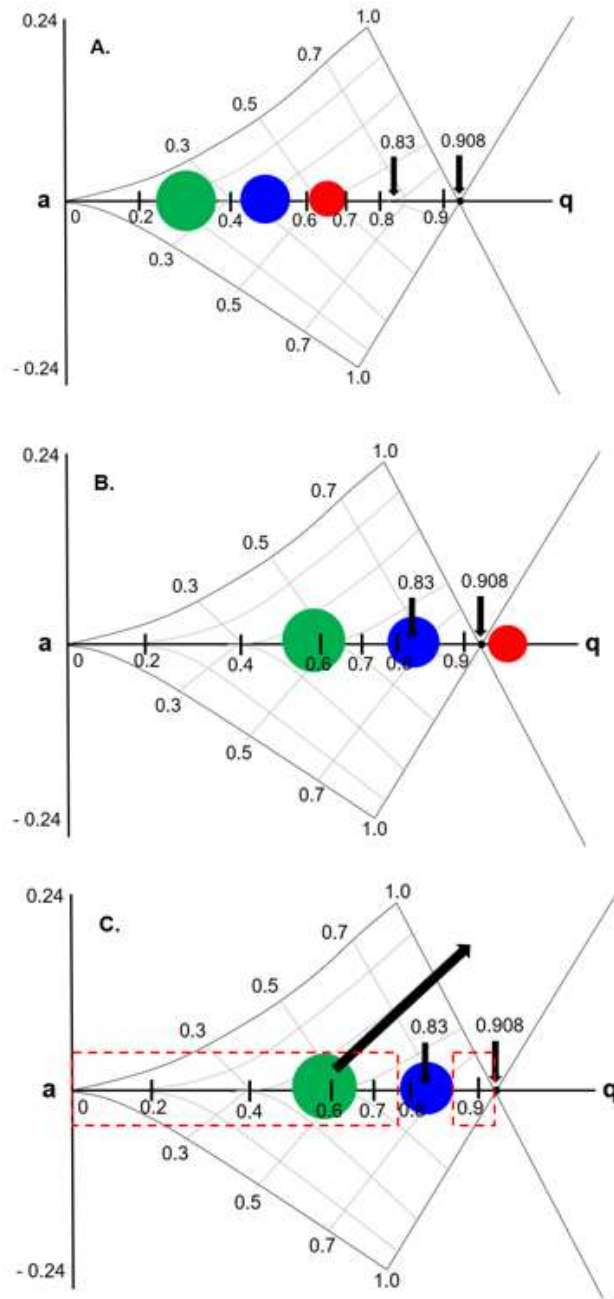


Figure 2.10 (A) Mathieu stability diagram showing ions of different  $m/z$  values with stable trajectories. (B) The RF amplitude is increased until the ion of interest (indicated using a blue circle) has a  $q$  value of 0.83 accompanied by ejection of the smallest ion (i.e., red circle) from the ion trap. (C) A tailored RF waveform is applied to the x-roads at all frequencies except for the secular frequency of the motion of the ion of interest (i.e., blue circle). The black arrow drawn from the green circle denotes an unstable trajectory when the tailored RF waveform is applied. This process results in isolation of the desired ion.<sup>15</sup>

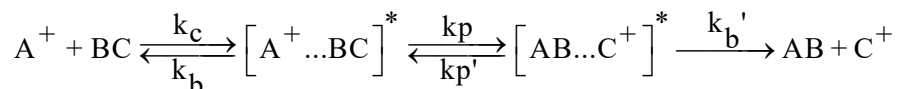
### 2.2.7 Collision-activated Dissociation (CAD)

In tandem mass spectrometric analysis, often the ions of interest are fragmented using CAD to gain insights into the structures of the ions. The ions of interest are at first isolated and excited. Then the ions undergo repeated low-energy collisions with the helium buffer gas inside the ion trap for a specific period of time (usually 30 ms). Each collision converts part of the ion kinetic energy into internal energy. Repeated collisions result in a gradual accumulation of internal energy in the ions until the internal energy is high enough to overcome the lowest dissociation energy threshold of the ion. At this point, the ions undergo fragmentation via low-energy pathways.<sup>27</sup>

### 2.2.8 Ion-molecule Reactions

In order to obtain structural information on analytes, often gas-phase ion-molecule reactions are used in addition to CAD experiments.<sup>28-31</sup> In this experiment, the ions of interest are first isolated and are allowed to react with a neutral reagent introduced into the ion trap through a home-built manifold. The product ions generated are detected which can provide helpful insights into the structure of the precursor ion.

For the introduction of the neutral reagents into the ion trap, an external manifold is used which was first developed by Gronert and co-workers.<sup>32,33</sup> The schematic of this manifold setup used is shown in **Figure 2.11**. In this setup, the reagent is leaked in through the helium line of the manifold using a syringe pump. Both the syringe port and the surrounding area of the manifold are heated to a temperature appropriate for the neutral reagent of choice in order to ensure complete evaporation of the reagent. A Granville-Phillips leak valve along a diverting line to waste is used to control the flow of the He/reagent mixture into the ion trap. Each day after completion of the experiments, the manifold is isolated from the instrument and baked out under vacuum to prevent contamination. During gas-phase ion-molecule reactions, a reactant complex is formed between the neutral reagent and the ions of interest due to long-range ion-dipole and/or ion-induced dipole forces, as illustrated in the scheme below:



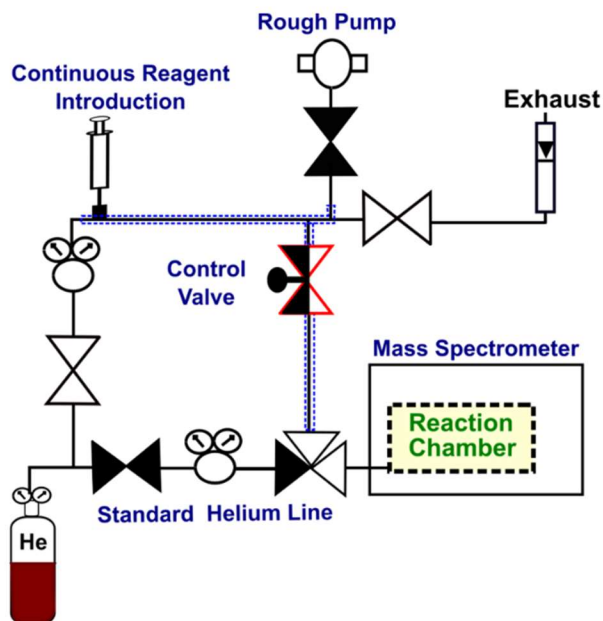


Figure 2.11 Inlet manifold for introduction of helium/reagent gas mixtures. The valves shown above are open to the manifold which allows the diluted reagent/helium mixture into the ion trap via a control valve.<sup>19</sup>

where  $k_c$  is the rate of collision,  $k_b$  is the rate of dissociation to form separated reactants,  $k_p$  and  $k_p'$  are the rates of forward and backward reactions respectively, and  $k_b'$  is the rate of dissociation to form separated products. In order to understand the plausible outcomes of ion-molecule reactions, Brauman proposed the double-well potential energy surface model (**Figure 2.12**).<sup>34,35</sup> According to this model, the long range dipole forces lower the potential energy of the complex by providing solvation energy. The collision complex utilizes this solvation energy to overcome the barrier for the reaction. The rate of the gas-phase ion-molecule reaction is dictated by the energy difference between the separated reactants and the transition states ( $\Delta E$ ; **Figure 2.12**). Unlike reactions in solution, the total energy in vacuum is conserved and gas-phase ion-molecule reactions proceed only when the overall reaction is exothermic. The height of the barrier dictates whether the reaction proceeds forward to generate the products or reverses back to form the reactants.

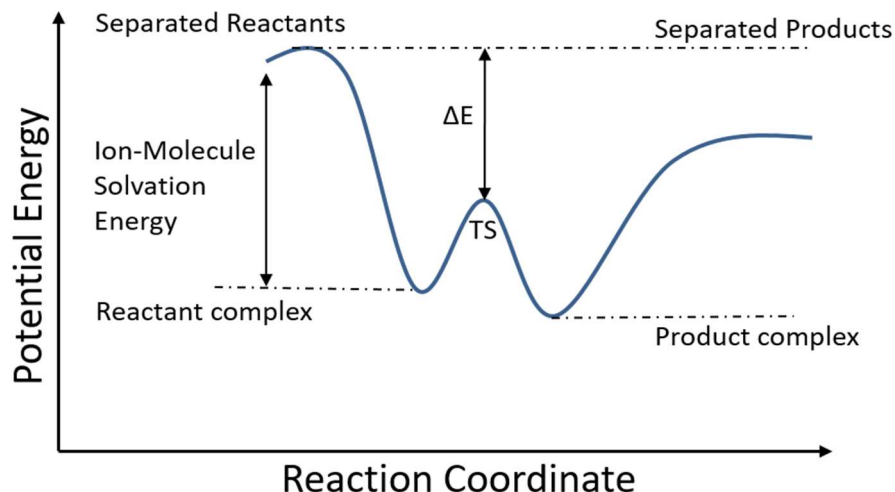


Figure 2.12 The Brauman double-well potential energy surface for a simple ion-molecule reaction in the gas phase.<sup>19</sup>

The transition state that leads to the formation of products is usually tighter than that leading to separated products. This implies that the transition state for the generation of the products is generally low in entropy and the dissociation of the reactant complex to generate separated reactants may occur faster than the product formation. This indicates that even when the net reaction is exothermic and the barrier is low in energy, many gas-phase ion-molecule reactions do not occur at collision rates ( $k_c$  as shown above) or may not proceed at all.<sup>35</sup>

### 2.2.9 Ion Ejection for Detection

The ions are detected by two detectors located perpendicular to the z-axis of the ion trap. Each detector consists of a conversion dynode and an electron multiplier (**Figure 2.13**). A potential of -15 kV or + 15 kV applied to the conversion dynodes attracts positive or negative ions, respectively, ejected from the ion trap. Positive ions hit the negatively charged dynode to eject electrons. An attractive electric field between the dynode and the electron multiplier attract the ions into the electron multiplier. The electrons hit the surface of the electron multiplier, which causes ejection of several electrons. The funnel shape of the electron multiplier enables this process to occur multiple times, creating more and more electrons. This cascade of electrons eventually creates a measurable current, which is proportional to the number of ions ejected from the ion trap.

## 2.2.10 Ion Detection

In order to detect the ions in the ion trap, they are ejected from the ion trap into the detection system using resonance ejection. A dipolar resonance excitation is applied on the x- electrode to enable ion ejection and this method increases the resolution and sensitivity.<sup>36,37</sup> Initially a supplementary RF voltage is applied to the x-electrodes and the main RF voltage is increased till the  $q$  value for the ions reached 0.88. At this point, the supplemental RF voltage applied to the x-electrodes is in frequency to the secular frequency of the ion, causing the ion to gain kinetic energy and oscillate (**Figure 2.14**). This oscillation causes the ions to get ejected from the ion trap through the slits on the x-rods of the ion trap. Then, the ejected ions hit the conversion dynode and were detected.

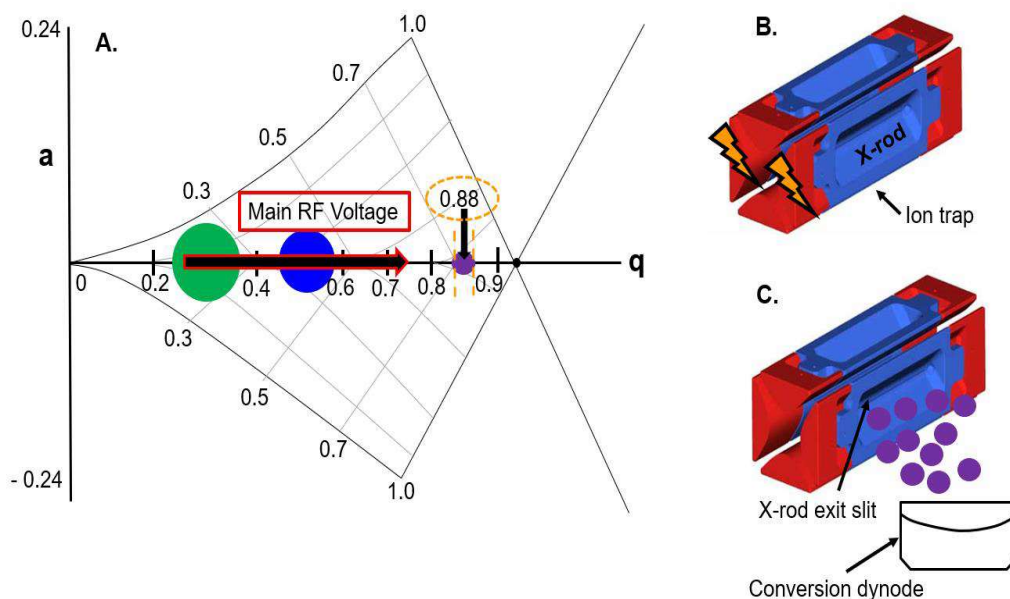


Figure 2.13 (A) The  $q$  values of the ions also increase with increasing main RF amplitude. (B) When the  $q$  value of the smallest ion (purple as shown above) reaches 0.88, a supplementary RF voltage is applied to the x-electrodes. The frequency of motion of the ions whose  $q$  value is 0.88 will be in resonance with the frequency of the supplementary RF voltage applied to the x-electrodes (C) These ions (purple circles) gain kinetic energy. The ions then move away from the center of the ion trap, exit via slits in the x-electrodes and strike the conversion dynode.<sup>15</sup>

## 2.3 Orbitrap

Orbitrap mass analyzers were first introduced in 2000 by Makarov.<sup>7</sup> The orbitrap utilizes a dynamic trapping method based on DC field to separate the ions. Dynamic trapping can be achieved by using one of three ways: linear trapping, ring trapping and orbital trapping.<sup>7</sup> Orbital trapping method, was initially developed by Kingdon in 1923 and was utilized to trap ions in the orbitrap mass spectrometers.<sup>38</sup> The concept ion trapping in Kingdon traps involves trapping of ions around a central wire stretched along the axis of a cylindrical electrode.<sup>38</sup> In orbitraps however, the ions are trapped in between two electrodes.<sup>39</sup> A schematic of a LQIT coupled with an orbitrap detector (Thermo Linear Quadrupole Ion Trap-Orbitrap XL) is shown in **Figure 2.15**. Analysis using the orbitrap mass analyzer is comprised of three key steps: transferring the ions into the orbitrap, moving the ions across and around the orbitrap and detecting the ions. The instrument (Thermo LTQ-Orbitrap XL) used in this research is equipped with an additional octupole collision cell (commercially known as HCD cell) additional fragmentation experiments, here referred to as medium-energy collision-activated dissociation (MCAD; also known as HCD) can be performed in the octupole collision cell. The details of these experiments are discussed below.

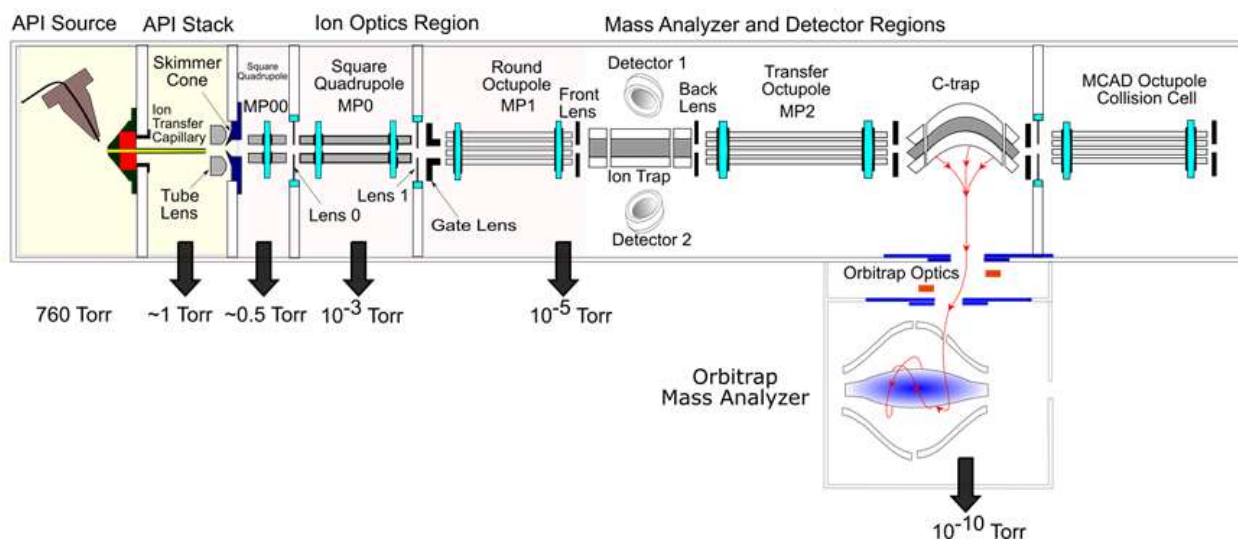


Figure 2.14 Schematic of an LQIT coupled to an orbitrap mass spectrometer (Thermo LTQ-Orbitrap XL). The pressures in different areas are also indicated. The red arrows represent the ion pathways from the C-trap into the orbitrap.<sup>15</sup>

The orbitrap consists of an outer barrel-like electrode and an inner coaxial spindle-like electrode, with the latter being supplied with external voltages.<sup>40</sup> The space between the electrodes is evacuated by a vacuum pump. This space makes up the ion trapping region. In this region, the ions are accelerated to a higher tangential velocity. Ions of same  $m/z$  values move as tight packets back and forth along the spindle electrode and also cycle around the spindle electrode.

### 2.3.1 Injection of Ions into the Orbitrap

Ions are transferred from the linear quadrupole ion trap into a C-shaped-RF only quadrupole called the C-trap (**Figure 2.17**). The C-trap is supplied with  $N_2$  as cooling gas and the pressure is maintained at approximately 1 mTorr.<sup>41</sup> The ions undergo collisional cooling by colliding with the  $N_2$  molecules before being axially compressed into the center of the C-trap by electrostatic fields. Then the ions pass through the ion optics as a tight ion packet and accelerated to high kinetic energies before being injected through a slit into one end of the orbitrap in less than one ms. An electrostatic deflector allows transfer of only the ions and prevents the carryover of  $N_2$  gas from the C-trap to the orbitrap.

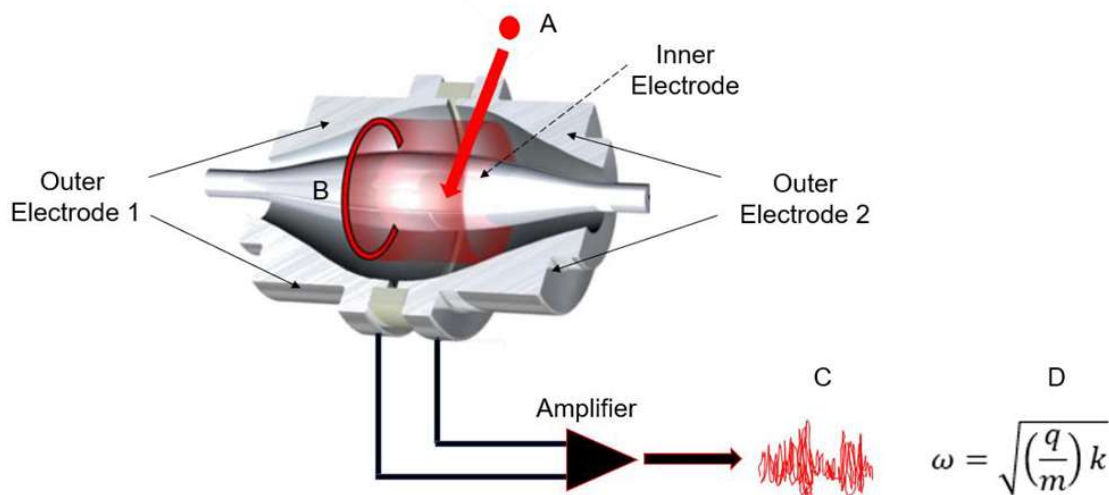


Figure 2.15 (A) Ions enter the orbitrap slightly off center (B) The electric field in the orbitrap causes ions to oscillate around and along the inner electrode. Ions with same  $m/z$  value move in tight packets (shown as thin rings). (C) The outer electrode measures the image current for the motion of the ion packets. (D) The frequency of the harmonic oscillations is proportional to the  $m/z$  value of the ions.

Ions were injected in tight packets at a position offset from the center of the orbitrap which leads to coherent axial oscillations of ion packets. Different ion packets are formed for ions with different  $m/z$  values and move differently. The rotational frequencies of ion packets depend upon their angles, initial position and their energies. The ion packets spread over the angular coordinates and form several thin rotating rings around the central electrode.

### 2.3.2 Trajectories of Ions in the Orbitrap

The outer and inner electrodes of the orbitrap were designed to create a three-dimensional electrostatic field ( $U$ ) when a DC voltage was applied to the inner electrodes. The quadropolar logarithmic field ( $U$ ) generated this way can be defined as

$$U(r,z) = \frac{k}{2} \left( z^2 - \frac{r^2}{2} \right) + \frac{k}{2} (R_m)^2 \ln \left[ \frac{r}{R_m} \right] + C \quad (2.16)$$

where  $r$  represents angular coordinate,  $z$  represents the axial coordinate ( $z=0$  due to equatorial plane of symmetry),  $k$  is a constant related to field curvature,  $R_m$  is radius of ion of mass  $m$ , and  $C$  is a constant.<sup>40,42</sup>

The ions in this quadropolar logarithmic field experience mainly two types of ion motion, rotational motion around the central electrode ( $r, \phi$ -motion where  $\phi$  is the angular coordinate) and axial oscillations along the central electrode. The frequencies of such motions can be represented as  $\omega_r, \omega_\phi$  and  $\omega_z$  respectively (**Figure 2.16**). The equations of ion motion in polar coordinates ( $\phi, r, z$ ) can be defined as

$$\frac{\partial^2 r}{\partial t^2} - r \left( \frac{\partial \phi}{\partial t} \right)^2 = -\frac{q}{m} \frac{k}{2} \left[ \frac{R_m^2}{r} - r \right] \quad (2.17)$$

$$\frac{d}{dt} \left[ r^2 \frac{\partial \phi}{\partial t} \right] = 0 \quad (2.18)$$

$$\frac{\partial^2 z}{\partial t^2} = -\frac{q}{m} kz \quad (2.19)$$

where  $m/q$  is the mass-to-charge ratio of the ion<sup>39</sup>

Among the above three frequencies, only the axial frequency  $\omega_\phi$  is independent of the position and energy of the ions. Hence, the axial frequency is used to determine the  $m/q$  value of the ions. The axial frequency of oscillation ( $\omega_z$ ) of an ion can be defined as

$$\omega_z = \sqrt{\left(\frac{q}{m}\right)k} \quad (2.20)$$

where  $k$  is a constant proportional to the voltage applied to the inner electrode.

### 2.3.3 Detection of Ions in the Orbitrap

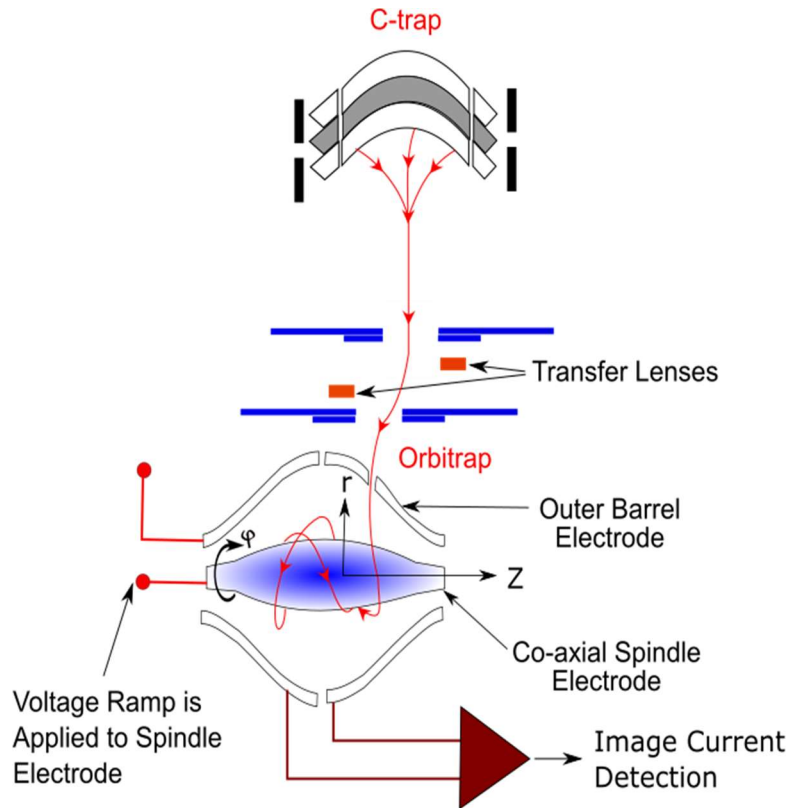


Figure 2.16 Red line indicates the injection of ion packets into the orbitrap off-center by the C-trap. The image current produced by the axial oscillation (z-axis) of the ions is measured by the outer electrode<sup>19</sup>

The image current of the oscillating ion packets is differentially amplified from each half of the outer electrode (**Figure 2.17**).<sup>39,41,43</sup> After amplification, the image current is converted into a frequency spectrum using fast Fourier transformation (FFT). Using a two-point calibration, the frequency spectrum is finally converted into a mass spectrum.<sup>41</sup>

## 2.4 Octupole Collision Cell

The LTQ Orbitrap XL mass spectrometer used in the research described in this thesis is equipped with an octupole collision cell (commercially known as HCD cell) filled with N<sub>2</sub> collision gas at a pressure of 3.8 mTorr. This collision cell is widely used to perform beam-type CAD experiments.<sup>44</sup> Although this method is commercially termed as ‘higher-energy collision activated dissociation’, IUPAC recommends that the term ‘high-energy’ should refer to ions with a translational energy greater than 1 keV.<sup>45</sup> Hence, our research group has introduced the term medium-energy collision-activated dissociation or MCAD for this fragmentation technique. Before MCAD experiments, ions are isolated in the linear quadrupole ion trap and transferred into the C-trap maintained at ground potential (**Figure 2.18**). Potential energy difference between the C-trap and the octupole collision cell accelerates the ions from the C-trap into the octupole collision cell and determines their kinetic energy. The accelerated ions collided with N<sub>2</sub> collision gas and undergo fragmentation. The DC offsets applied to the various sections of the instrument during MCAD are shown in **Figure 2.18**. MCAD often results in more extensive fragmentation compared to CAD in the ion trap because ions have greater kinetic energy during MCAD and collisions with N<sub>2</sub> are higher in energy than those with helium. After fragmentation, all ions are again transferred into the C-trap. From C-trap, ions are ejected into the orbitrap for analysis as described above for detection in the orbitrap.

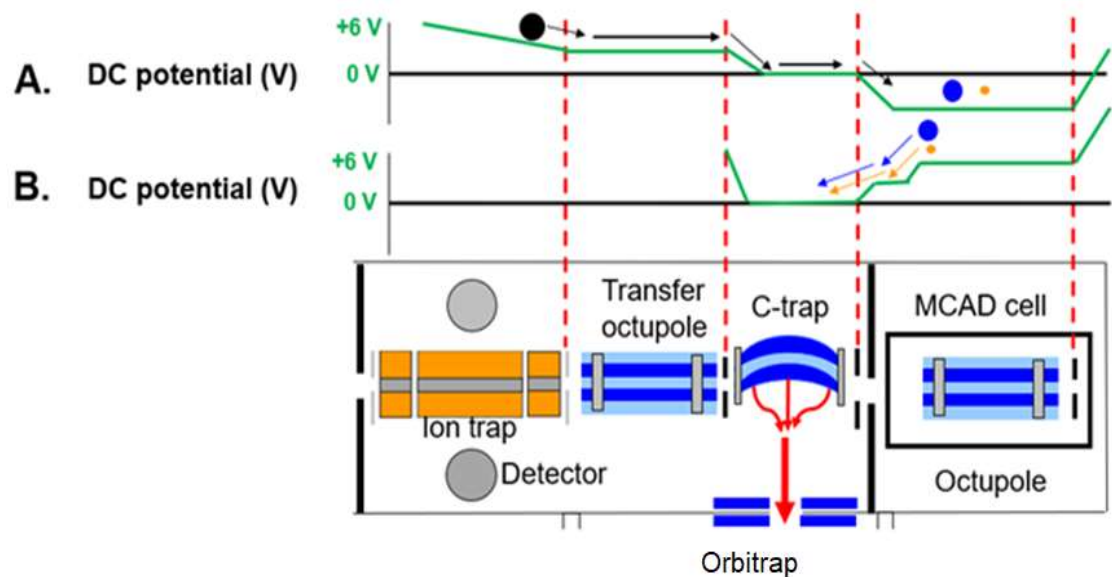


Figure 2.17 (A) A DC offset potential between the C-trap and the MCAD cell accelerates ions into the MCAD cell and induces their fragmentation. (B) Typical offset potentials applied to eject ions from the MCAD cell back into the C-trap. The ions are then transferred into the orbitrap for analysis. Only transfer of ions from the linear quadrupole ion trap via the C trap into the MCAD cell and then back into the C-trap is illustrated. The black circle represents a positively charged isolated ion while the blue and orange circles represent positively charged fragment ions generated by fragmentation of the isolated ion<sup>15</sup>

## 2.5 References

- (1) Han, X.; Aslanian, A.; Yates, J. R. Mass Spectrometry for Proteomics. *Curr. Opin. Chem. Biol.* 2008, 12 (5), 483–490. <https://doi.org/10.1016/j.cbpa.2008.07.024>.
- (2) Huang, Z.; Ogasawara, D.; Seneviratne, U. I.; Cognetta, A. B.; am Ende, C. W.; Nason, D. M.; Lapham, K.; Litchfield, J.; Johnson, D. S.; Cravatt, B. F. Global Portrait of Protein Targets of Metabolites of the Neurotoxic Compound BIA 10–2474. *ACS Chem. Biol.* 2019, 14 (2), 192–197. <https://doi.org/10.1021/acscchembio.8b01097>.
- (3) Maurer, H. Mass Spectrometry for Research and Application in Therapeutic Drug Monitoring or Clinical and Forensic Toxicology. *Ther. Drug Monit.* 2018, 40 (4), 389–393. <https://doi.org/10.1097/FTD.0000000000000525>.
- (4) Marshall, A. G.; Rodgers, R. P. Petroleomics: Chemistry of the Underworld. *Proc. Natl. Acad. Sci.* 2008, 105 (47), 18090–18095. <https://doi.org/10.1073/pnas.0805069105>.
- (5) Richardson, S. D. Mass Spectrometry in Environmental Sciences. *Chem. Rev.* 2001, 101 (2), 211–254. <https://doi.org/10.1021/cr990090u>.
- (6) Takáts, Z.; Wiseman, J. M.; Gologan, B.; Cooks, R. G. Mass Spectrometry Sampling Under Ambient Conditions with Desorption Electrospray Ionization. *Science* 2004, 306 (5695), 471–473. <https://doi.org/10.1126/science.1104404>.
- (7) Makarov, A. Electrostatic Axially Harmonic Orbital Trapping: A High-Performance Technique of Mass Analysis. *Anal. Chem.* 2000, 72 (6), 1156–1162. <https://doi.org/10.1021/ac991131p>.
- (8) Cody, R. B.; Laramée, J. A.; Durst, H. D. Versatile New Ion Source for the Analysis of Materials in Open Air under Ambient Conditions. *Anal. Chem.* 2005, 77 (8), 2297–2302. <https://doi.org/10.1021/ac050162j>.
- (9) Fenn, J. B.; Mann, M.; Meng, C. K.; Wong, S. F.; Whitehouse, C. M. Electrospray Ionization for Mass Spectrometry of Large Biomolecules. *Science* 1989, 246 (4926), 64–71. <https://doi.org/10.1126/science.2675315>.
- (10) Carroll, D. I.; Dzidic, I.; Stillwell, R. N.; Horning, M. G.; Horning, E. C. Subpicogram Detection System for Gas Phase Analysis Based upon Atmospheric Pressure Ionization (API) Mass Spectrometry. *Anal. Chem.* 1974, 46 (6), 706–710. <https://doi.org/10.1021/ac60342a009>.
- (11) Robb, D. B.; Covey, T. R.; Bruins, A. P. Atmospheric Pressure Photoionization: An Ionization Method for Liquid Chromatography–Mass Spectrometry. *Anal. Chem.* 2000, 72 (15), 3653–3659. <https://doi.org/10.1021/ac0001636>.
- (12) Lattimer, R. P.; Schulten, H. R. Field Ionization and Field Desorption Mass Spectrometry: Past, Present, and Future. *Anal. Chem.* 1989, 61 (21), 1201A–1215A. <https://doi.org/10.1021/ac00196a001>.

- (13) Rebane, R.; Kruve, A.; Liigand, P.; Liigand, J.; Herodes, K.; Leito, I. Establishing Atmospheric Pressure Chemical Ionization Efficiency Scale. *Anal. Chem.* 2016, 88 (7), 3435–3439. <https://doi.org/10.1021/acs.analchem.5b04852>.
- (14) Xia, Y.; McLuckey, S. A. Evolution of Instrumentation for the Study of Gas-Phase Ion/Ion Chemistry via Mass Spectrometry. *J. Am. Soc. Mass Spectrom.* 2008, 19 (2), 173–189. <https://doi.org/10.1016/j.jasms.2007.10.018>.
- (15) Gronert, S. Quadrupole Ion Trap Studies of Fundamental Organic Reactions. *Mass Spectrom. Rev.* 2005, 24 (1), 100–120. <https://doi.org/10.1002/mas.20008>.
- (16) Romanczyk, M. DEVELOPING MASS SPECTROMETRIC METHODS FOR DISTINGUISHING ISOMERS, CHARACTERIZING COMPLEX MIXTURES AND DETERMINING THE CAPABILITY OF ORGANIC COMPOUNDS TO SWELL AIRCRAFT O-RING SEALS, Purdue University, 2019.
- (17) Konermann, L.; Ahadi, E.; Rodriguez, A. D.; Vahidi, S. Unraveling the Mechanism of Electrospray Ionization. *Anal. Chem.* 2013, 85 (1), 2–9. <https://doi.org/10.1021/ac302789c>.
- (18) Gomez, A.; Tang, K. Charge and Fission of Droplets in Electrostatic Sprays. *Phys. Fluids* 1994, 6 (1), 404–414. <https://doi.org/10.1063/1.868037>.
- (19) Yerabolu, R. MASS SPECTROMETRIC METHODS DEVELOPMENT FOR THE CHARACTERIZATION OF COMPONENTS IN COMPLEX MIXTURES FOR ENHANCED OIL RECOVERY OPERATIONS AND FOR DRUG DEVELOPMENT. A Dissertation, Purdue University, 2018.
- (20) Gross, J. H. Ambient Mass Spectrometry. In *Mass Spectrometry: A Textbook*; Gross, J. H., Ed.; Springer: Berlin, Heidelberg, 2011; pp 621–649. [https://doi.org/10.1007/978-3-642-10711-5\\_13](https://doi.org/10.1007/978-3-642-10711-5_13).
- (21) Schwartz, J. C.; Senko, M. W.; Syka, J. E. P. A Two-Dimensional Quadrupole Ion Trap Mass Spectrometer. *J. Am. Soc. Mass Spectrom.* 2002, 13 (6), 659–669. [https://doi.org/10.1016/S1044-0305\(02\)00384-7](https://doi.org/10.1016/S1044-0305(02)00384-7).
- (22) March, R. E. An Introduction to Quadrupole Ion Trap Mass Spectrometry. *J. Mass Spectrom.* 1997, 32 (4), 351–369.
- (23) Douglas, D. J. Linear Quadrupoles in Mass Spectrometry. *Mass Spectrom. Rev.* 2009, 28 (6), 937–960. <https://doi.org/10.1002/mas.20249>.
- (24) Douglas, D. J.; Frank, A. J.; Mao, D. Linear Ion Traps in Mass Spectrometry. *Mass Spectrom. Rev.* 2005, 24 (1), 1–29. <https://doi.org/10.1002/mas.20004>.

- (25) Kaiser, R. E.; Graham Cooks, R.; Stafford, G. C.; Syka, J. E. P.; Hemberger, P. H. Operation of a Quadrupole Ion Trap Mass Spectrometer to Achieve High Mass/Charge Ratios. *Int. J. Mass Spectrom. Ion Process.* 1991, 106, 79–115. [https://doi.org/10.1016/0168-1176\(91\)85013-C](https://doi.org/10.1016/0168-1176(91)85013-C).
- (26) Xu, W.; Song, Q.; Smith, S. A.; Chappell, W. J.; Ouyang, Z. Ion Trap Mass Analysis at High Pressure: A Theoretical View. *J. Am. Soc. Mass Spectrom.* 2009, 20 (11), 2144–2153. <https://doi.org/10.1016/j.jasms.2009.06.019>.
- (27) McLuckey, S. A.; Goeringer, D. E. SPECIAL FEATURE: TUTORIAL Slow Heating Methods in Tandem Mass Spectrometry. *J. Mass Spectrom.* 1997, 32 (5), 461–474. [https://doi.org/10.1002/\(SICI\)1096-9888\(199705\)32:5<461::AID-JMS515>3.0.CO;2-H](https://doi.org/10.1002/(SICI)1096-9888(199705)32:5<461::AID-JMS515>3.0.CO;2-H).
- (28) Brodbelt, J. S. Analytical Applications of Ion-Molecule Reactions. *Mass Spectrom. Rev.* 1997, 16 (2), 91–110. [https://doi.org/10.1002/\(SICI\)1098-2787\(1997\)16:2<91::AID-MAS3>3.0.CO;2-4](https://doi.org/10.1002/(SICI)1098-2787(1997)16:2<91::AID-MAS3>3.0.CO;2-4).
- (29) Eberlin, M. N. Structurally Diagnostic Ion/Molecule Reactions: Class and Functional-Group Identification by Mass Spectrometry. *J. Mass Spectrom.* 2006, 41 (2), 141–156. <https://doi.org/10.1002/jms.998>.
- (30) Friedman, L. Ion-Molecule Reactions. *Annu. Rev. Phys. Chem.* 1968, 19 (1), 273–300. <https://doi.org/10.1146/annurev.pc.19.100168.001421>.
- (31) Osburn, S.; Ryzhov, V. Ion–Molecule Reactions: Analytical and Structural Tool. *Anal. Chem.* 2013, 85 (2), 769–778. <https://doi.org/10.1021/ac302920a>.
- (32) Gronert, S. Estimation of Effective Ion Temperatures in a Quadrupole Ion Trap. *J. Am. Soc. Mass Spectrom.* 1998, 9 (8), 845–848. [https://doi.org/10.1016/S1044-0305\(98\)00055-5](https://doi.org/10.1016/S1044-0305(98)00055-5).
- (33) Gronert, S. Mass Spectrometric Studies of Organic Ion/Molecule Reactions. *Chem. Rev.* 2001, 101 (2), 329–360. <https://doi.org/10.1021/cr9900836>.
- (34) Brauman, J. I. Some Historical Background on the Double-Well Potential Model. *J. Mass Spectrom.* 1995, 30 (12), 1649–1651. <https://doi.org/10.1002/jms.1190301203>.
- (35) Olmstead, W. N.; Brauman, J. I. Gas-Phase Nucleophilic Displacement Reactions. *J. Am. Chem. Soc.* 1977, 99 (13), 4219–4228. <https://doi.org/10.1021/ja00455a002>.
- (36) Hoffmann, E. de. Tandem Mass Spectrometry: A Primer. *J. Mass Spectrom.* 1996, 31 (2), 129–137. [https://doi.org/10.1002/\(SICI\)1096-9888\(199602\)31:2<129::AID-JMS305>3.0.CO;2-T](https://doi.org/10.1002/(SICI)1096-9888(199602)31:2<129::AID-JMS305>3.0.CO;2-T).
- (37) Schwartz, J. C.; Syka, J. E. P.; Jardine, I. High Resolution on a Quadrupole Ion Trap Mass Spectrometer. *J. Am. Soc. Mass Spectrom.* 1991, 2 (3), 198–204. [https://doi.org/10.1016/1044-0305\(91\)80044-8](https://doi.org/10.1016/1044-0305(91)80044-8).

- (38) Kingdon, K. H. A Method for the Neutralization of Electron Space Charge by Positive Ionization at Very Low Gas Pressures. *Phys. Rev.* 1923, 21 (4), 408–418. <https://doi.org/10.1103/PhysRev.21.408>.
- (39) Perry, R. H.; Cooks, R. G.; Noll, R. J. Orbitrap Mass Spectrometry: Instrumentation, Ion Motion and Applications. *Mass Spectrom. Rev.* 2008, 27 (6), 661–699. <https://doi.org/10.1002/mas.20186>.
- (40) Makarov, A.; Hardman, M. E.; Schwartz, J. C.; Jose, S.; Senko, M. W. (73) Assignee: Thermo Finnigan LLC, San Jose, CA. 20.
- (41) Makarov, A.; Denisov, E.; Kholomeev, A.; Balschun, W.; Lange, O.; Strupat, K.; Horning, S. Performance Evaluation of a Hybrid Linear Ion Trap/Orbitrap Mass Spectrometer. *Anal. Chem.* 2006, 78 (7), 2113–2120. <https://doi.org/10.1021/ac0518811>.
- (42) Gillig, K. J.; Bluhm, B. K.; Russell, D. H. Ion Motion in a Fourier Transform Ion Cyclotron Resonance Wire Ion Guide Cell. *Int. J. Mass Spectrom. Ion Process.* 1996, 157–158, 129–147. [https://doi.org/10.1016/S0168-1176\(96\)04465-5](https://doi.org/10.1016/S0168-1176(96)04465-5).
- (43) Paffen, F.-J. LTQ Orbitrap XL Getting Started 2.5.5. 190.
- (44) Olsen, J. V. Higher-Energy C-Trap Dissociation (HCD) for Precise Peptide Modification Analysis. *Nature Methods* volume, pages –712 (2007 709).
- (45) Murray, K. K.; Boyd, R. K.; Eberlin, M. N.; Langley, G. J.; Li, L.; Naito, Y. Definitions of Terms Relating to Mass Spectrometry (IUPAC Recommendations 2013). *Pure Appl. Chem.* 2013, 85 (7), 1515–1609. <https://doi.org/10.1351/PAC-REC-06-04-06>.

## CHAPTER 3. EFFECTS OF RESIDUAL WATER IN A LINEAR QUADRUPOLE ION TRAP ON THE PROTONATION SITES OF 4-AMINOBENZOIC ACID

### 3.1 Introduction

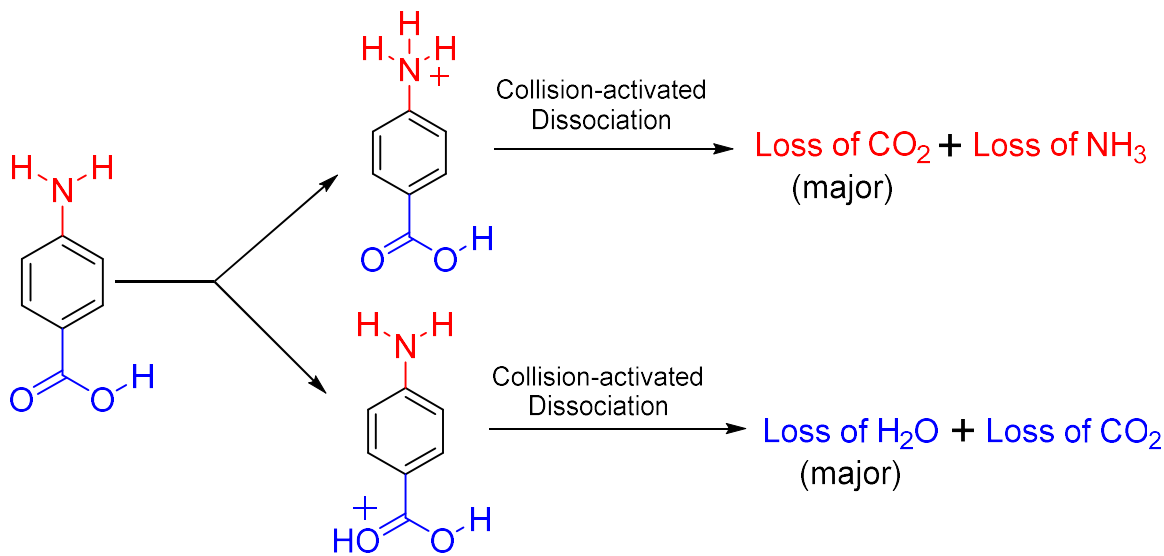
In recent years, protonation sites in polyfunctional analytes have received a lot of attention. In solution, the protonation site(s) of polyfunctional analytes are governed by the basicity of the different sites in the analyte as well as the interactions between the neutral and protonated functionalities of the analyte and the surrounding solvent. In the gas phase, usually the thermochemically favored protonation site dominates due to lack of solvation energy (present in solution).<sup>1</sup> This can become problematic in many ionization techniques where analytes are evaporated from their solution. After atmospheric pressure ionization, the distribution of protomers of polyfunctional analytes in the gas phase can be different from that in solution. The protomer distribution has been reported to depend on many experimental parameters, including the solvent(s) used, the method of ionization and the conditions in the ion source.<sup>2-7</sup> This causes difficulties in identifying polyfunctional analytes when the structures of their protonated forms are probed using collision-activated dissociation (CAD) as the fragmentation patterns obtained for different protomers can be very dissimilar. This also complicates the comparison of analyte CAD fragmentation patterns with CAD databases.<sup>8-10</sup> Different protomers may also exhibit different bimolecular reactivities, which can complicate the identification of functional groups in protonated analytes via functional-group selective gas-phase ion-molecule reactions.<sup>11</sup> Numerous studies have been carried out to better understand the influence of solvents and other variables on the protonation sites of various polyfunctional analytes. One of such widely studied analyte is 4-aminobenzoic acid whose protonation sites have been investigated extensively using electrospray ionization (ESI) in tandem mass spectrometry.<sup>1,2,5,7,12-14</sup>

In solution, 4-aminobenzoic acid is predominantly protonated on the amino nitrogen because the localized charge on the nitrogen atom is better solvated than the delocalized charge on the protonated carboxylic acid group.<sup>15</sup> Quantum chemical calculations indicated that in the gas phase, the carboxylic acid oxygen is the most basic site.<sup>3</sup> This is because the charge in protonated 4-aminobenzoic acid is delocalized over both oxygen atoms, the aromatic ring and the amino nitrogen.<sup>3</sup> Interestingly, numerous mass spectrometric studies have reported simultaneous

generation of the two protomers upon ESI and that the relative abundances of the protomers depend upon various experimental parameters, including the nature of the ionization solvent used.<sup>1,3,12-14</sup> Protonation occurred predominantly on the amino nitrogen when acetonitrile was used as the ionization solvent.<sup>1</sup> However, when water was used as the ionization solvent, both the N- and O-protomers were generated and detailed experimental studies using IRPD spectroscopy suggested that the preferred protonation site depended upon the size of the water clusters formed around the protonated 4-aminobenzoic acid molecule after ionization.<sup>16</sup> IR spectra obtained by both calculations and experiments showed that if the cluster contained six or more water molecules, the amino nitrogen was the preferred site of protonation whereas if the cluster contained less than six water molecules, the carboxylic acid oxygen was the preferred site of protonation.<sup>16</sup> Extensive calculations performed at the B3LYP-GD3/6-311++G(d,p) level of theory suggested that when using methanol as the ionization solvent, *N*-protomer is predominantly generated in the presence of more than eight methanol molecules.<sup>6,12</sup> However, for smaller clusters of methanol, the carboxylic acid oxygen is the predominant site of protonation.<sup>6,12</sup>

The protonation sites of 4-aminobenzoic acid have also been investigated in mixed solvent systems. The *O*-protomer has been reported to be preferentially generated when 3-1 (*v/v*) methanol-water was used as the ionization solvent.<sup>3,6</sup> This observation has been rationalized by formation of water/methanol clusters capable of forming a solvent bridge between the protonation sites which can move the proton from the amino nitrogen onto the carbonyl oxygen. On the contrary, the *N*-protomer has been reported to be preferentially generated when 1-1 (*v/v*) acetonitrile-water was used as the ionization solvent. This observation has been explained by the formation of adducts of acetonitrile and the *N*-protomer in the gas phase, which prevents the transfer of the proton from the amino nitrogen to the carboxylic acid oxygen (favored in the gas phase).<sup>1</sup>

Collision-activated dissociation (CAD) or infrared photodissociation spectroscopy have been used in the above studies to identify the structures of the protomers.<sup>1-3</sup> Most recently, conclusive studies have been performed using ion-mobility experiments.<sup>12,17</sup> The widely accepted consensus is that upon CAD, the *O*-protomer fragments predominantly via loss of H<sub>2</sub>O while the *N*-protomer fragments much slower than the *O*-protomer and loses CO<sub>2</sub> (**Scheme 3.1**).



Scheme 3.1 Losses observed upon CAD of the two protomers of protonated 4-aminobenzoic acid

Inspired by the above published results, the protonation sites of 4-aminobenzoic acid were investigated using the linear quadrupole ion traps (LQIT) in our group. However, when protonated 4-aminobenzoic acid was subjected to CAD inside a linear quadrupole ion trap (ion-trap CAD or ITCAD) in this thesis research, the solvent dependent selectivity of the protonation sites was lost. This finding contradicts the previously published literature reports.<sup>3,12</sup> Investigation of causes for such discrepancy led to the current research.

## 3.2 Experimental

### 3.2.1 Chemicals

4-Aminobenzoic acid (with  $\geq 99$  % purity) was purchased from Sigma-Aldrich. LC-MS grade methanol, water and acetonitrile were purchased from Thermo Fischer Scientific. All the chemicals were used as received without any further purification. Nitrogen used as a collision gas during medium-energy CAD experiments was obtained from the boil off of liquified nitrogen which was purchased from Linde.

### 3.2.2 Sample Preparation

Stock solutions of 4-aminobenzoic acid were prepared in 3-1 (v/v) methanol-water and 1-1 (v/v) acetonitrile-water at a concentration of 0.01 mM.

### 3.2.3 Instrumentation

A Thermo Scientific LTQ XL linear quadrupole ion trap (LQIT) mass spectrometer coupled with a high-resolution orbitrap mass analyzer was used for the experiments. An electrospray ionization source (ESI) operating in the positive ion mode was used. The ESI capillary was maintained at a temperature of 275 °C, the sheath gas (N<sub>2</sub>) flow rate was 30 (arbitrary units), the auxiliary gas (N<sub>2</sub>) flow rate was 10 (arbitrary units) and the spray voltage was kept at 3 kV. The analyte solutions were introduced into the ESI source at a flow rate of 20 μL min<sup>-1</sup> using a 500 μL Hamilton syringe.

#### 3.2.3.1 In-Source CAD (ISCAD)

During ISCAD, the ions generated in the ion source were accelerated from the skimmer region into the first multipole region of the ion source. The ion optics region is usually maintained at a pressure of 1 mTorr. The accelerated ions collided with the solvent and the air molecules present in the ion optics region and underwent fragmentation. It is important to note that during ISCAD, ions were subjected to CAD without isolation.

#### 3.2.3.2 Medium-energy CAD (MCAD) (commercially known as HCD)

In order to perform MCAD experiments, protonated 4-aminobenzoic acid was first isolated in the linear quadrupole ion trap (filled with helium buffer gas) using an isolation width of 2 *m/z* units and an isolation time of 30 ms. The isolated ions were then transferred from the linear quadrupole ion trap into the C-trap. The ions were then accelerated from the C-trap into an octupole collision cell by keeping the octupole at a 13 V lower potential than the C-trap.<sup>18</sup> The details of this process have been described in Chapter 2. The accelerated ions underwent collisions for a very short period of time (μs) with nitrogen gas molecules (purity 99.998 %) present in the octupole at a nominal pressure of 3-5 mTorr. The fragment ions generated were transferred into the orbitrap for detection and analysis.

#### 3.2.3.3 CAD in the Ion Trap (ITCAD)

During ITCAD experiments, the ions were isolated in the linear quadrupole ion trap and were subjected to CAD for 30 ms by accelerating them and allowing them to collide with helium

buffer gas (nominal pressure about 2 mTorr). For ITCAD, a  $q$  value of 0.25 and a collision energy of 30 (arbitrary units) were used. Detection and analysis of fragment ions were carried out by ejecting the ions in a mass selective manner from the ion trap into two electron multipliers, one on each side of the ion trap.

In a few experiments, additional water was injected into the linear quadrupole ion trap via an external home-built manifold. A syringe pump maintained at a flow rate of 6  $\mu\text{L}/\text{h}$  was used for the introduction of water. The injected water was diluted with helium at a flow rate of 0.6 L/h and a Granville-Phillips leak valve was used for the introduction. The manifold set up used has been described previously.<sup>19-21</sup> The manifold was kept at a temperature of 100 °C.

#### 3.2.3.4 Computational Studies

Geometry optimizations and single-point energy calculations were performed using Gaussian 16.<sup>22</sup> M06-2X/6-311++G(d,p) level of theory was used to optimize the molecular structures and for calculation of the potential energy surfaces for the fragmentation of the O- and N-protomers. All the optimized structures were ensured to have the correct number of negative frequencies (0 for minima and 1 for transition states). The negative frequency found for the transition states was verified to correspond to the bond(s) broken and/or formed during the reaction. All the calculations were performed at 298 K and all the values were corrected for zero-point energy. Intrinsic reaction coordinate (IRC) calculations were carried out for all transition states.

### 3.3 Results and Discussions

Two previously studied solvent systems, 3-1 (v/v) methanol-water and 1-1 (v/v) acetonitrile-water, were used for the dissolution of 4-aminobenzoic acid.<sup>3</sup> 4-Aminobenzoic acid was protonated using ESI. The ions were subjected to three different CAD experiments, CAD in the ion source area (in-source CAD or ISCAD), CAD in the octupole collision cell (medium-energy CAD or MCAD) and CAD in the linear quadrupole ion trap (ITCAD). The results of the experiments performed are discussed below in the same order.

During ISCAD experiments, all ions were transferred from the ion source into the skimmer region that was maintained at ground potential.<sup>23</sup> An attractive dc voltage applied to the ion transfer multipole (located after the skimmer region) was used to accelerate the ions. The accelerated ions

underwent activating collisions with the solvent and air molecules in the multipole region, causing fragmentation of the ions. All the ions were then transferred into the LQIT where they were separated according to their  $m/z$  values and were detected using the electron multipliers located on two sides of the ion trap. The mass spectra obtained after using two different solvent systems are shown in **Figure 3.1**. As shown in **Figure 3.1a**, when methanol-water was used as the solvent system, protonated 4-aminobenzoic acid predominantly lost  $\text{H}_2\text{O}$  whereas when acetonitrile-water was used as the solvent system, predominant loss of  $\text{CO}_2$  was observed (Figure 3.1 b). These results indicate that protonation had occurred preferably on the carbonyl oxygen when using methanol-water but on the amino nitrogen when using acetonitrile-water. These results are in agreement with the previously published reports.<sup>2,3</sup>

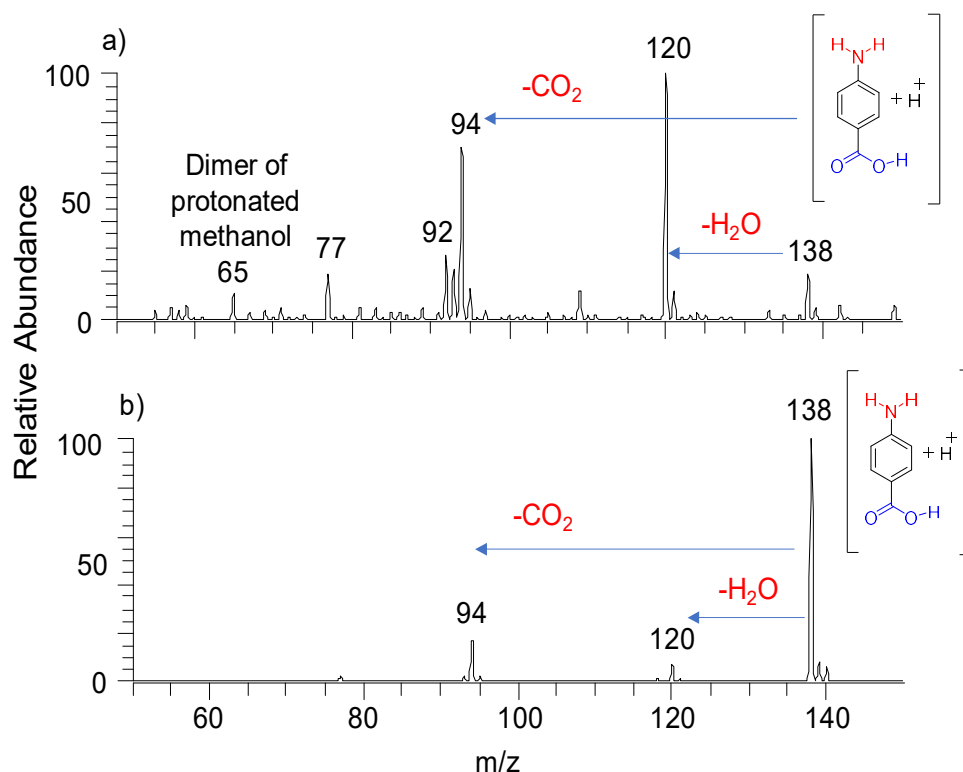


Figure 3.1 ISCAD mass spectra (collision energy 30 V) measured for all the ions ionized using ESI in a) 3-1 (v/v) methanol-water and b) 1-1 (v/v) acetonitrile-water. The ions were detected using electron multipliers located outside the linear quadrupole ion trap.

Previously published studies have indicated that the N-protomer requires about 30 kcal/mol more energy for fragmentation than the O-protomer.<sup>2</sup> Therefore, greater abundance of the

unfragmented protonated 4-aminobenzoic acid ( $m/z$  138) was observed when acetonitrile-water was used as the ionization solvent (**Figure 3.1 b**). This observation further verifies the dominant generation of N-protomer in acetonitrile-water and predominant generation of O-protomer in methanol-water.

Protonated 4-aminobenzoic acid was also subjected to MCAD experiments. In these experiments, ions isolated in the linear quadrupole ion trap were accelerated and transferred into the octupole collision cell. In the octupole collision cell, the accelerated ions were subjected to CAD with nitrogen gas. After MCAD, all the ions were transferred into the orbitrap for analysis and detection. Predominant loss of H<sub>2</sub>O was observed when 4-aminobenzoic acid was dissolved in methanol-water (Figure 3.2a) but predominant loss of CO<sub>2</sub> was observed when acetonitrile-water was used as the ionization solvent (**Figure 3.2b**). These results are in agreement with those observed for ISCAD as well as with previous literature.

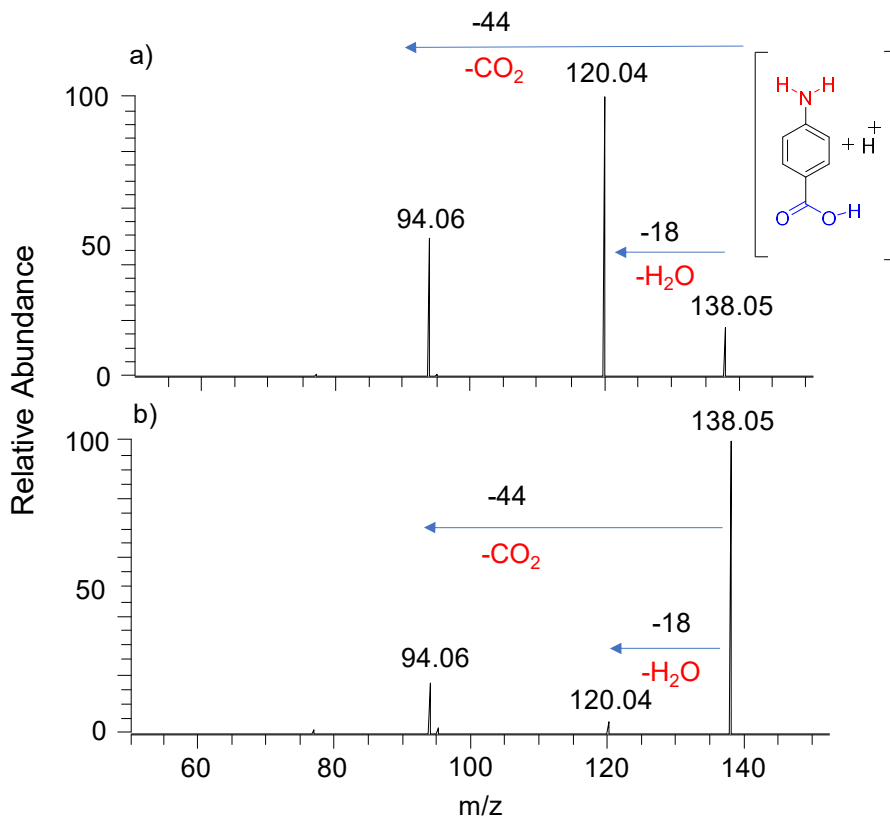


Figure 3.2 High resolution MCAD mass spectra (collision energy 13 eV) recorded for protonated 4-aminobenzoic acid, ionized using ESI in a) 3-1 (v/v) methanol-water and b) 1-1 (v/v) acetonitrile-water.

Lastly, protonated 4-aminobenzoic acid was subjected to ITCAD. In these experiments, the ions were isolated in the linear quadrupole ion trap. The isolated ions were then accelerated in the ion trap by applying a low amplitude rf-excitation voltage at the same secular frequency as the frequency of motion of the ions. Multiple low-energy collisions of the accelerated ions with helium buffer gas in the ion trap resulted in fragmentation of the ions. The fragment ions were detected using the electron multipliers located on each side of the LQIT and the mass spectra obtained are shown in **Figure 3.3**. As evident from **Figure 3.3b**, when acetonitrile-water was used as the ionization solvent, protonated 4-aminobenzoic acid predominantly fragmented via loss of CO<sub>2</sub>, in agreement with the literature.<sup>2,3,12</sup> On the contrary, when methanol-water was used as the ionization solvent, fragment ions corresponding to loss of CO<sub>2</sub> and H<sub>2</sub>O were observed in nearly equal abundance (**Figure 3.3a**). These unexpected results suggest that before or during ITCAD,

some of the O-protonomers formed in the ion source had converted back to the N-protonomers, which contradicts with the results obtained for MCAD and ISCAD.

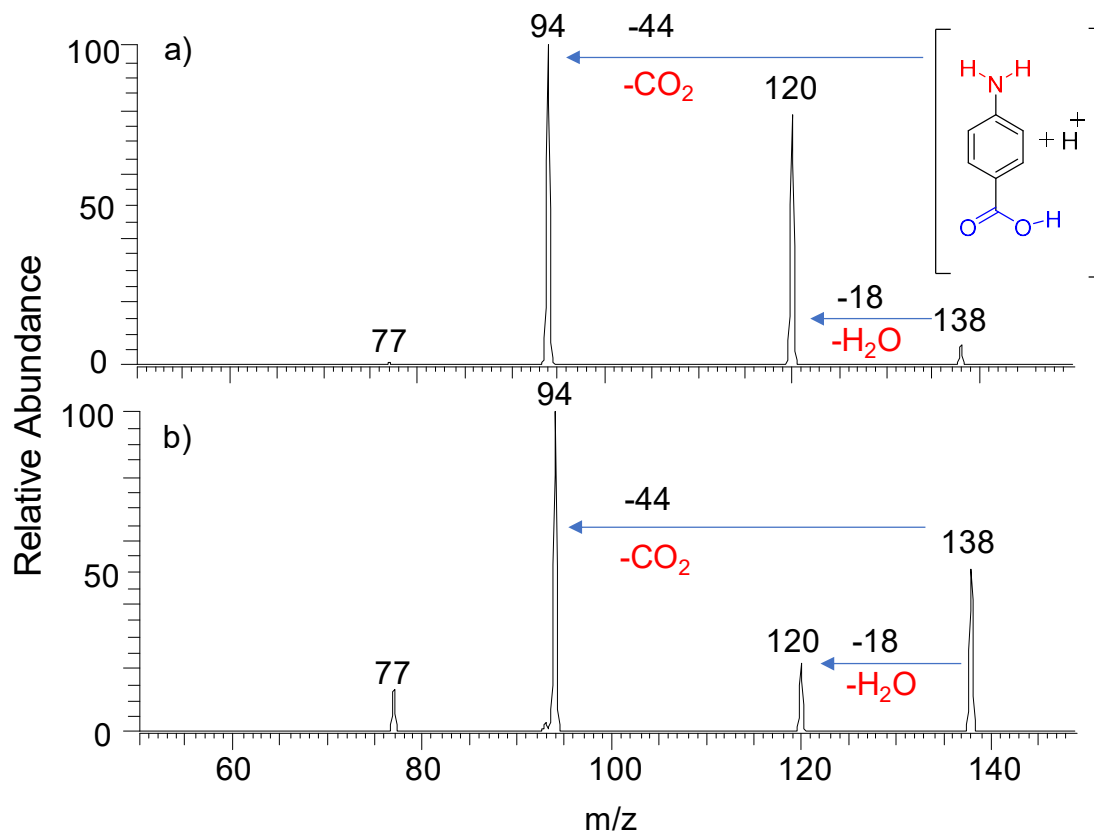


Figure 3.3 ITCAD mass spectra (collision energy 30 arbitrary units) recorded for protonated 4-aminobenzoic acid, ionized using ESI in a) 3-1 (v/v) methanol-water and b) 1-1 (v/v) acetonitrile-water. Ion of  $m/z$  77 corresponds to loss of  $\text{NH}_3$  from the ion of  $m/z$  94

In order to investigate whether the method used for detection of fragment ions plays a role in the manifested protonation sites, the fragment ions resulting from ITCAD were transferred through the C-trap into the high-resolution orbitrap for analysis and detection. As evident from **Figure 3.4**, ITCAD mass spectra obtained this way were similar to those obtained using the electron multipliers.

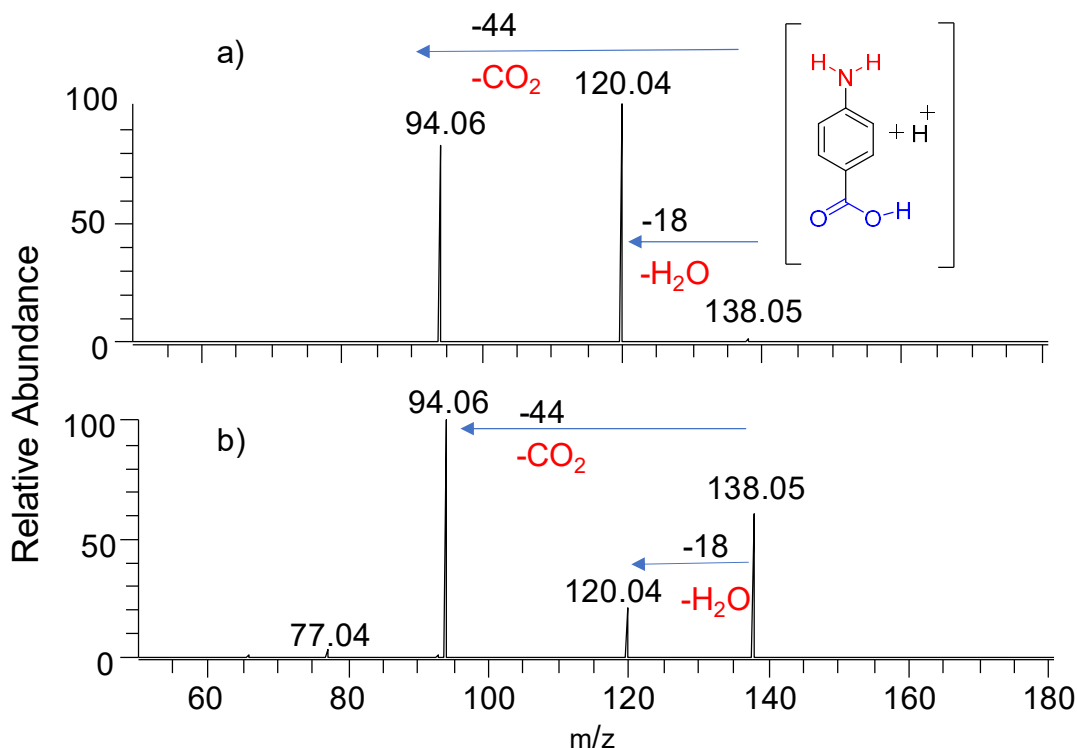


Figure 3.4 ITCAD products (collision energy: 35 arbitrary units) of protonated 4-aminobenzoic acid detected by high-resolution orbitrap when using a) 3-1 (v/v) methanol-water and b) 1-1 (v/v) acetonitrile-water solvent systems.

These observations led to the hypothesis that residual water in the LQIT may be responsible for the different protomer distribution. The ion transfer region between the capillary skimmer cone and the linear quadrupole ion trap (region where ISCAD occurs) contains significant amounts of air and solvent molecules and is maintained at a pressure of  $\sim 1$  mTorr.<sup>24,25</sup> Some less volatile solvent molecules may survive into the low-pressure regions of the mass spectrometer, including the linear quadrupole ion trap. In order to test this hypothesis, the background compounds in the linear quadrupole ion trap were investigated. This experiment was performed by generating molecular ions of  $\text{CO}_2$  via APCI using  $\text{CO}_2$  as the auxiliary and sheath gas. The molecular ions of  $\text{CO}_2$  were transferred into the linear quadrupole ion trap, isolated and allowed to react with residual compounds present in the ion trap for 30 ms. The resulting mass spectrum is shown in Figure 3.5. As shown in Figure 3.5, significant amount of water and oxygen were observed in the linear quadrupole ion trap. If enough water molecules were present to form clusters containing six or more water molecules around the O-protomer, they would behave like bulk solution favoring the

formation of N-protomers (Scheme 3.2a). O-protomers in these clusters could have rearranged back to N-protomers which can explain the greater than expected abundance of the N-protomers in when using methanol-water as the ionization solvent.

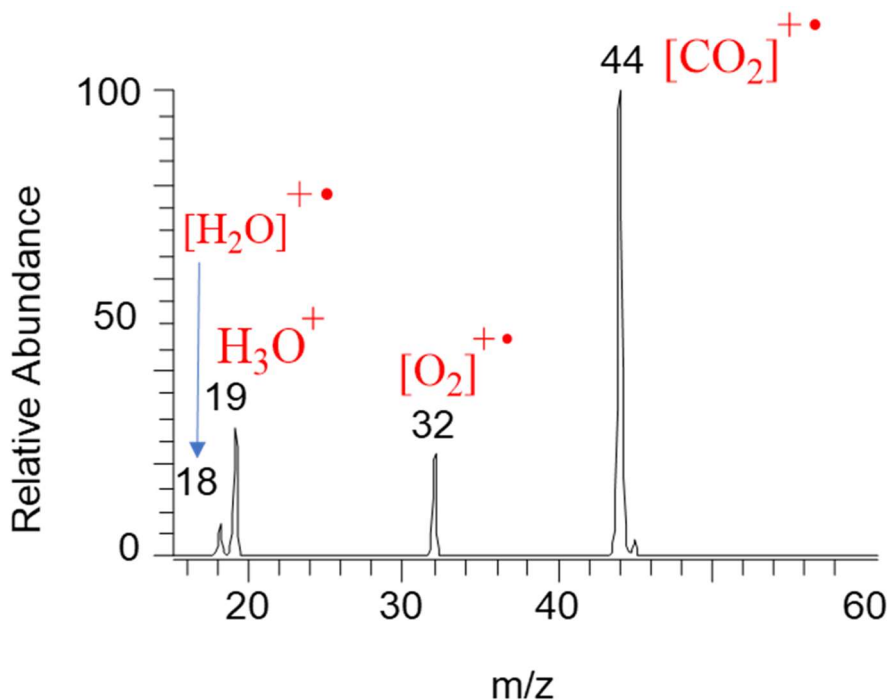


Figure 3.5 Water and oxygen were detected in the linear quadrupole ion trap when the molecular ions of carbon dioxide (ionized using APCI) were isolated and allowed to react with residual molecules in the ion trap for 30 ms. As  $\text{N}_2$  has a greater ionization energy (15.6 eV) than  $\text{CO}_2$  (13.8 eV),  $\text{N}_2$  in the ion trap were not detected using this method

In order to investigate the above assumptions, two more experiments were performed. In these experiments, additional water was introduced into the linear quadrupole ion trap by using an external reagent manifold. 4-Aminobenzoic acid dissolved in the two different solvent systems was introduced into the ESI source and ionized, and the ions were transferred into the ion trap, isolated and subjected to ITCAD in the presence of added water. The mass spectra collected when using 3-1 methanol-water solvent system did not change significantly upon addition of water into the trap (Figure 3.6a). On the contrary, product distribution measured when using acetonitrile-water changed drastically and resembled that measured using methanol-water although some excess of the N-protomer was still detectable (Figure 3.6b). This can be rationalized by the

presence of water clusters of various sizes in the linear quadrupole ion trap, some favoring the O-protomer while others favoring the N-protomer. After prolonged exposure to the background water in the ion trap, an equilibrium mixture of the protomers may have been achieved. As both the solvent systems generated almost the same abundances of the two protomers, this distribution of protomers must be close to the equilibrium distribution. Since N-protomer required extra water to reach a similar protomer distribution as the O-protomer, conversion of N-protomer requires larger water clusters than conversion of the O-protomer ( $\geq 6$ ). A summary of such isomerization reactions taking place is shown in **Scheme 3.2**

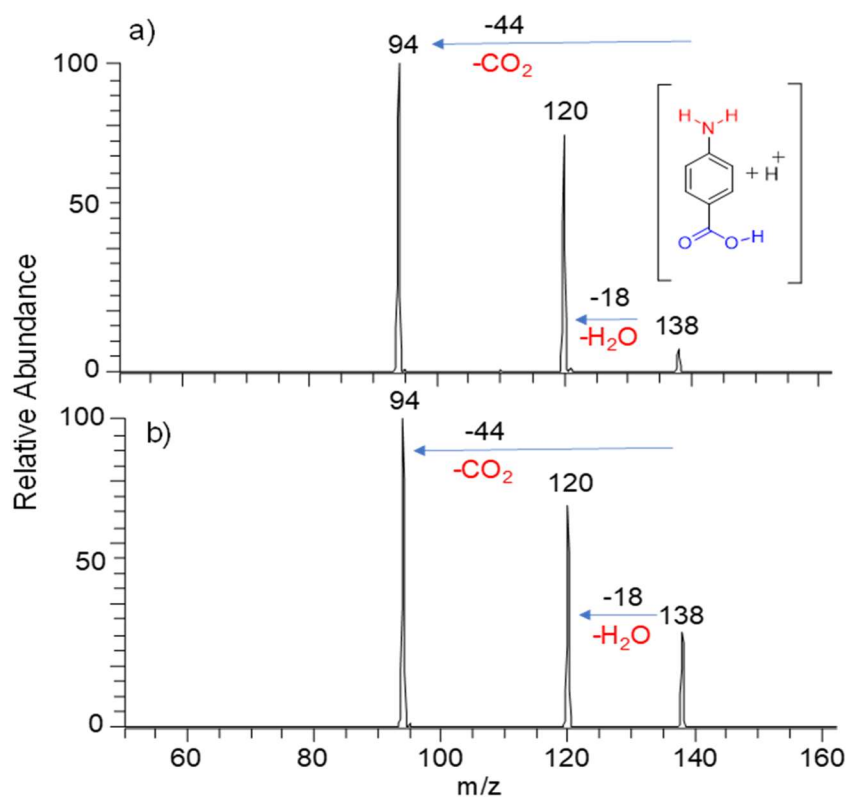
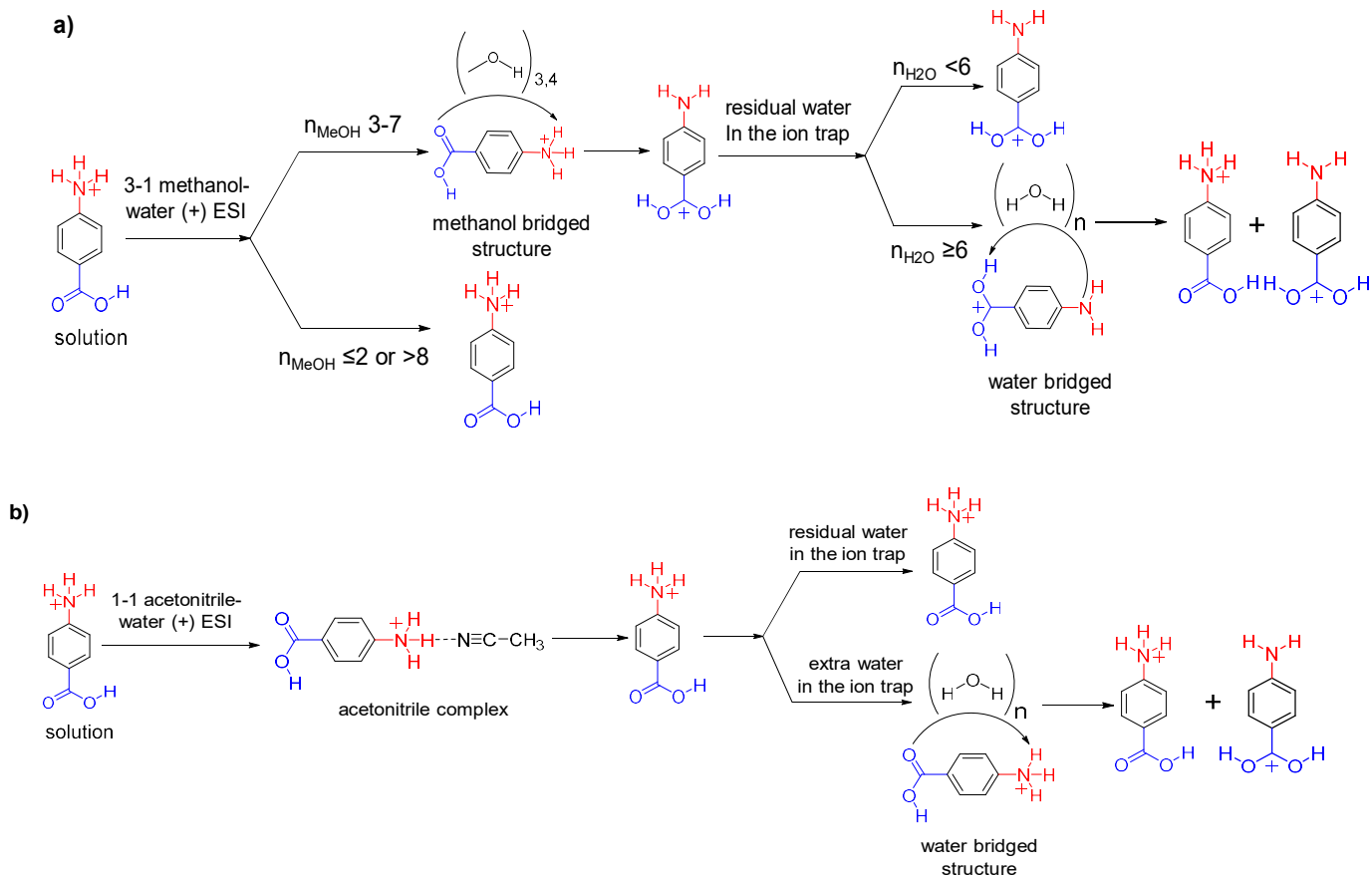


Figure 3.6 ITCAD mass spectra (collision energy 30 arbitrary units; detection method: external electron multipliers) recorded in the presence of extra water for protonated 4-aminobenzoic acid (ionized by ESI by using a) 3-1 (v/v) methanol-water and b) 1-1 (v/v) acetonitrile-water solvent systems)



Scheme 3.2 Scheme showing tautomerization of the protomers of 4-aminobenzoic acid when ionized using a) 3-1 methanol-water and b) 1-1 acetonitrile-water. <sup>a</sup>  $n$  is the number of solvent molecules in solvent clusters around the protonated analyte

It is crucial to address the reasons for the lack of isomerization of the O-protomer to N-protomer during ISCAD and MCAD. In both ISCAD and MCAD experiments, the kinetic energies of the ions were greater and the time frame was shorter ( $\mu\text{s}$  vs  $\text{ms}$  time frame) than for ITCAD. For ISCAD, the pressure was lower than for ITCAD, which might hinder formation of large long-lived solvent clusters. The octupole collision cell used for MCAD experiments was located far away from the atmospheric pressure ionization source and it was filled with high-purity nitrogen gas. This may have prevented the formation of large solvent clusters around the analyte ions during MCAD.

Previously published calculations suggested that the activation enthalpy for the loss of  $\text{H}_2\text{O}$  from the O-protomer is almost the same as that for the loss of  $\text{CO}_2$  (44.1 and 43.2 kcal/mol, respectively).<sup>2</sup> This result is not in a complete agreement with the present experimental results

where the loss of H<sub>2</sub>O from the O-protomer was more facile than the loss of CO<sub>2</sub>. In order to better understand the mechanisms and energetics of the fragmentation patterns of the two protomers, quantum chemical calculations were performed at the M06-2X/6-311++G (d,p) level of theory.

The activation enthalpy for the loss of H<sub>2</sub>O from the O-protomer was calculated to be only 38.6 kcal/mol while the activation enthalpy for the loss of CO<sub>2</sub> from the O-protomer was calculated to be 45.5 kcal/mol (**Figure 3.7**). Hence the activation energy required for the loss of H<sub>2</sub>O is than that for the loss of CO<sub>2</sub> from the O-protomer. The N-protomer requires substantially more energy to eliminate CO<sub>2</sub> than the O-protomer as the activation enthalpy was calculated to be 74.3 kcal/mol. According to literature, even more energy is required for the elimination of NH<sub>3</sub> from the N-protomer (reaction endothermicity 81.9 kcal/mol). These results explain the lower rate of fragmentation of the N-protomer than the O-protomer, in agreement with the literature.<sup>2,3,6,12</sup>

### 3.4 Conclusions

The most basic site of 4-aminobenzoic acid in solution is the amino nitrogen whereas calculations indicate that the carbonyl oxygen is the most basic site in the gas phase.<sup>2,3,12,17</sup> Based on CAD, both the N- and O-protomers were generated upon electrospray ionization with their relative abundances depending upon the experimental conditions.<sup>3,12,17</sup> When acetonitrile-water was used as the ionization solvent, solution-favored N-protomer was predominantly generated. This is because acetonitrile can form a stable adduct with the N-protomer, trapping the proton on the amino nitrogen.<sup>13</sup> When methanol-water was used as the ionization solvent, O-protomer was predominantly generated. This observation can be rationalized by the evaporation of solvent molecules from the large solvent clusters initially formed in the ion source area, resulting in the formation of smaller water and/or methanol clusters where the O-protomer is more stable than the N-protomer.<sup>6,12</sup> A solvent bridge between the two protonation sites allows the transfer of a proton from the amino nitrogen onto the carbonyl oxygen. This phenomenon is not possible in presence of acetonitrile. These previously published observations, however, are in sharp contrast with the results obtained in ITCAD experiments in the presence of extra water in the linear quadrupole ion trap. These experiments revealed the formation of a nearly equal amount of both protomers when using both solvent systems, which can be rationalized by the formation of water clusters of various sizes inside the ion trap. These water clusters vary widely in sizes, some of which favor the formation of the N-protomer while the others favor the formation of the O-protomer by forming a

solvent bridge between the two protonation sites. Similar protomer distributions in both solvent systems suggest that an equilibrium was nearly reached in presence of water. In contrast, ISCAD and MCAD results were in agreement with literature. This can be rationalized by the lack of long-lived water clusters during MCAD experiments and the shorter ion residence times during ISCAD experiments. Finally, the addition of water into the linear quadrupole ion trap eliminated the solvent-caused differences exhibited in ITCAD experiments in the protomer distribution of 4-aminobenzoic acid.

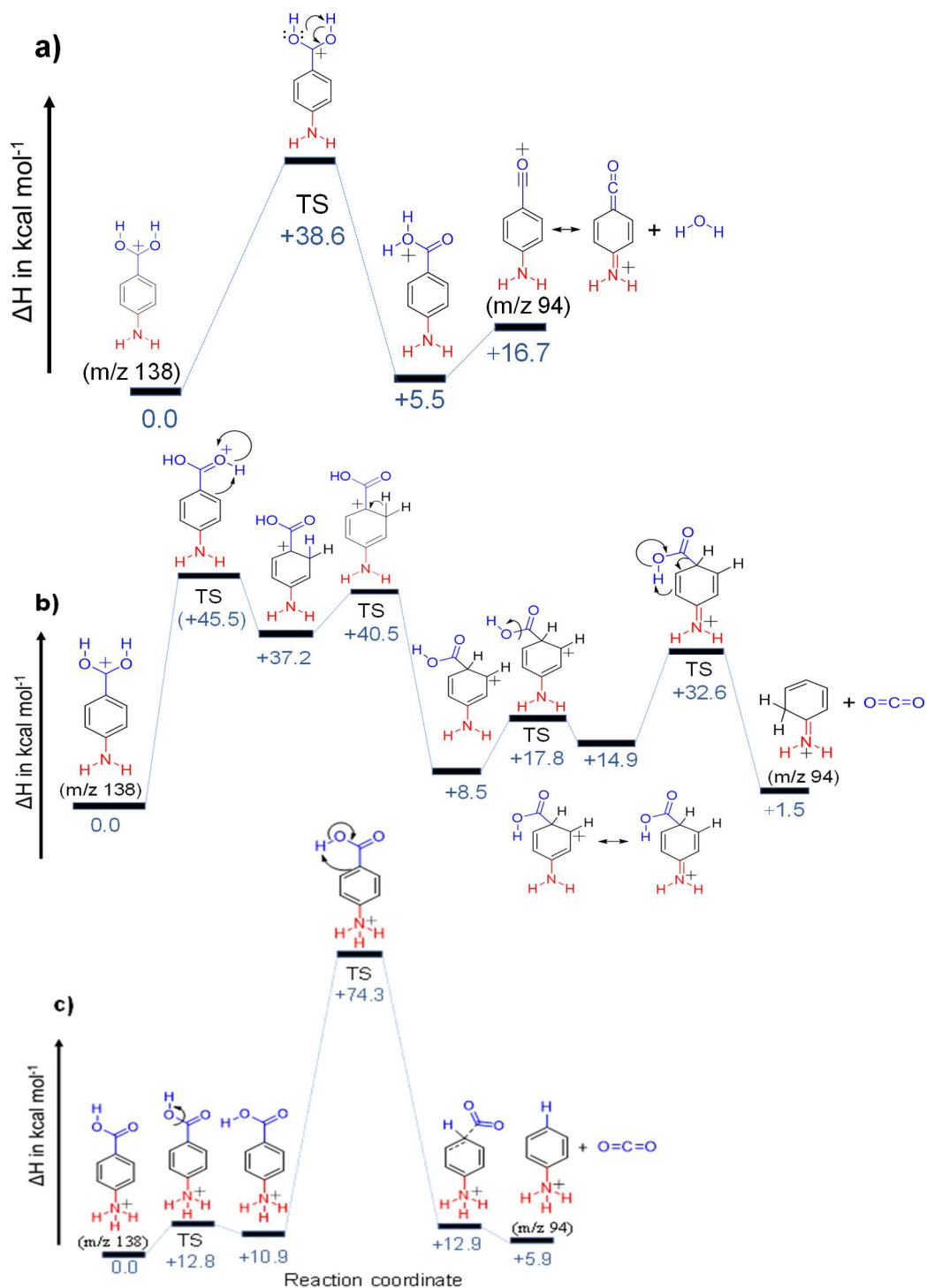


Figure 3.7 Potential energy surfaces and transition state structures calculated at the M06-2X/6-311++G(d, p) level of theory for (A) loss of H<sub>2</sub>O from the O-protomer, (B) loss of CO<sub>2</sub> from the O-protomer and (C) loss of CO<sub>2</sub> from the N-protomer

### 3.5 References

- (1) Seo, J.; Warnke, S.; Gewinner, S.; Schöllkopf, W.; T. Bowers, M.; Pagel, K.; Helden, G. von. The Impact of Environment and Resonance Effects on the Site of Protonation of Aminobenzoic Acid Derivatives. *Phys. Chem. Chem. Phys.* **2016**, *18* (36), 25474–25482. <https://doi.org/10.1039/C6CP04941A>.
- (2) Schmidt, J.; Meyer, M. M.; Spector, I.; Kass, S. R. Infrared Multiphoton Dissociation Spectroscopy Study of Protonated *p*-Aminobenzoic Acid: Does Electrospray Ionization Afford the Amino- or Carboxy-Protonated Ion? *J. Phys. Chem. A* **2011**, *115* (26), 7625–7632. <https://doi.org/10.1021/jp203829z>.
- (3) Tian, Z.; Kass, S. R. Gas-Phase versus Liquid-Phase Structures by Electrospray Ionization Mass Spectrometry. *Angew. Chem. Int. Ed.* **2009**, *48* (7), 1321–1323. <https://doi.org/10.1002/anie.200805392>.
- (4) Attygalle, A. B.; Xia, H.; Pavlov, J. Influence of Ionization Source Conditions on the Gas-Phase Protomer Distribution of Anilinium and Related Cations. *J. Am. Soc. Mass Spectrom.* **2017**, *28* (8), 1575–1586. <https://doi.org/10.1007/s13361-017-1640-0>.
- (5) Xia, H.; Attygalle, A. B. Effect of Electrospray Ionization Source Conditions on the Tautomer Distribution of Deprotonated *p*-Hydroxybenzoic Acid in the Gas Phase. *Anal. Chem.* **2016**, *88* (11), 6035–6043. <https://doi.org/10.1021/acs.analchem.6b01230>.
- (6) Campbell, J. L.; Yang, A. M.-C.; Melo, L. R.; Hopkins, W. S. Studying Gas-Phase Interconversion of Tautomers Using Differential Mobility Spectrometry. *J. Am. Soc. Mass Spectrom.* **2016**, *27* (7), 1277–1284. <https://doi.org/10.1007/s13361-016-1392-2>.
- (7) Chai, Y.; Weng, G.; Shen, S.; Sun, C.; Pan, Y. The Protonation Site of Para-Dimethylaminobenzoic Acid Using Atmospheric Pressure Ionization Methods. *J. Am. Soc. Mass Spectrom.* **2015**, *26* (4), 668–676. <https://doi.org/10.1007/s13361-014-1069-7>.
- (8) Stein, S. Mass Spectral Reference Libraries: An Ever-Expanding Resource for Chemical Identification. *Anal. Chem.* **2012**, *84* (17), 7274–7282. <https://doi.org/10.1021/ac301205z>.
- (9) Klagkou, K.; Pullen, F.; Harrison, M.; Organ, A.; Firth, A.; Langley, G. J. Approaches towards the Automated Interpretation and Prediction of Electrospray Tandem Mass Spectra of Non-Peptidic Combinatorial Compounds. *Rapid Commun. Mass Spectrom.* **2003**, *17* (11), 1163–1168. <https://doi.org/10.1002/rcm.987>.
- (10) Heinonen, M.; Rantanen, A.; Mielikäinen, T.; Kokkonen, J.; Kiuru, J.; Ketola, R. A.; Rousu, J. FiD: A Software for Ab Initio Structural Identification of Product Ions from Tandem Mass Spectrometric Data. *Rapid Commun. Mass Spectrom.* **2008**, *22* (19), 3043–3052. <https://doi.org/10.1002/rcm.3701>.

- (11) Sheng, H.; Tang, W.; Yerabolu, R.; Max, J.; Kotha, R. R.; Riedeman, J. S.; Nash, J. J.; Zhang, M.; Kenttämä, Hilka. I. Identification of *N*-Oxide and Sulfoxide Functionalities in Protonated Drug Metabolites by Using Ion–Molecule Reactions Followed by Collisionally Activated Dissociation in a Linear Quadrupole Ion Trap Mass Spectrometer. *J. Org. Chem.* **2016**, *81* (2), 575–586. <https://doi.org/10.1021/acs.joc.5b02409>.
- (12) Campbell, J. L.; Le Blanc, J. C. Y.; Schneider, B. B. Probing Electrospray Ionization Dynamics Using Differential Mobility Spectrometry: The Curious Case of 4-Aminobenzoic Acid. *Anal. Chem.* **2012**, *84* (18), 7857–7864. <https://doi.org/10.1021/ac301529w>.
- (13) Cismesia, A. P.; Nicholls, G. R.; Polfer, N. C. Amine vs. Carboxylic Acid Protonation in Ortho-, Meta-, and Para-Aminobenzoic Acid: An IRMPD Spectroscopy Study. *J. Mol. Spectrosc.* **2017**, *332*, 79–85. <https://doi.org/10.1016/j.jms.2016.10.020>.
- (14) Patrick, A. L.; Cismesia, A. P.; Tesler, L. F.; Polfer, N. C. Effects of ESI Conditions on Kinetic Trapping of the Solution-Phase Protonation Isomer of *p*-Aminobenzoic Acid in the Gas Phase. *Int. J. Mass Spectrom.* **2017**, *418*, 148–155. <https://doi.org/10.1016/j.ijms.2016.09.022>.
- (15) Zhang, X. X.; Oscarson, J. L.; Izatt, R. M.; Schuck, P. C.; Li, D. Thermodynamics of Macroscopic and Microscopic Proton Ionization from Protonated 4-Aminobenzoic Acid in Aqueous Solution from 298.15 to 393.15 K. *J. Phys. Chem. B* **2000**, *104* (35), 8598–8605. <https://doi.org/10.1021/jp994379r>.
- (16) Chang, T. M.; Prell, J. S.; Warrick, E. R.; Williams, E. R. Where’s the Charge? Protonation Sites in Gaseous Ions Change with Hydration. *J. Am. Chem. Soc.* **2012**, *134* (38), 15805–15813. <https://doi.org/10.1021/ja304929h>.
- (17) Xia, H.; Attygalle, A. B. Transformation of the Gas-Phase Favored *O*-Protomer of *p*-Aminobenzoic Acid to Its Unfavored *N*-Protomer by Ion Activation in the Presence of Water Vapor: An Ion-Mobility Mass Spectrometry Study. *J. Mass Spectrom.* **2018**, *53* (4), 353–360. <https://doi.org/10.1002/jms.4066>.
- (18) Olsen, J. V.; Macek, B.; Lange, O.; Makarov, A.; Horning, S.; Mann, M. Higher-Energy C-Trap Dissociation for Peptide Modification Analysis. *Nat. Methods* **2007**, *4* (9), 709–712. <https://doi.org/10.1038/nmeth1060>.
- (19) Gronert, S. Quadrupole Ion Trap Studies of Fundamental Organic Reactions. *Mass Spectrom. Rev.* **2005**, *24* (1), 100–120. <https://doi.org/10.1002/mas.20008>.
- (20) Gronert, S. Estimation of Effective Ion Temperatures in a Quadrupole Ion Trap. *J. Am. Soc. Mass Spectrom.* **1998**, *9* (8), 845–848. [https://doi.org/10.1016/S1044-0305\(98\)00055-5](https://doi.org/10.1016/S1044-0305(98)00055-5).
- (21) Habicht, S. C.; Vinueza, N. R.; Amundson, L. M.; Kenttämä, H. I. Comparison of Functional Group Selective Ion–Molecule Reactions of Trimethyl Borate in Different Ion Trap Mass Spectrometers. *J. Am. Soc. Mass Spectrom.* **2011**, *22* (3), 520–530. <https://doi.org/10.1007/s13361-010-0050-3>.

- (22) M. J. Frisch, G. W. Trucks, H. B. Schlegel, G. E. Scuseria, M. A. Robb, J. R. Cheeseman, G. Scalmani, V. Barone, B. Mennucci, G. A. Petersson, H. Nakatsuji, M. Caricato, X. Li, H. P. Hratchian, A. F. Izmaylov, J. Bloino, G. Zheng, J. L. Sonnenberg, M. Hada, M. Ehara, K. Toyota, R. Fukuda, J. Hasegawa, M. Ishida, T. Nakajima, Y. Honda, O. Kitao, H. Nakai, T. Vreven, J. A. Montgomery, Jr., J. E. Peralta, F. Ogliaro, M. Bearpark, J. J. Heyd, E. Brothers, K. N. Kudin, V. N. Staroverov, T. Keith, R. Kobayashi, J. Normand, K. Raghavachari, A. Rendell, J. C. Burant, S. S. Iyengar, J. Tomasi, M. Cossi, N. Rega, J. M. Millam, M. Klene, J. E. Knox, J. B. Cross, V. Bakken, C. Adamo, J. Jaramillo, R. Gomperts, R. E. Stratmann, O. Yazyev, A. J. Austin, R. Cammi, C. Pomelli, J. W. Ochterski, R. L. Martin, K. Morokuma, V. G. Zakrzewski, G. A. Voth, P. Salvador, J. J. Dannenberg, S. Dapprich, A. D. Daniels, O. Farkas, J. B. Foresman, J. V. Ortiz, J. Cioslowski, D. J. Fox, Gaussian, Inc., Wallingford CT, 2013. Gaussian 09, Revision D.01.
- (23) Parcher, J. F.; Wang, M.; Chittiboyina, A. G.; Khan, I. A. In-Source Collision-Induced Dissociation (IS-CID): Applications, Issues and Structure Elucidation with Single-Stage Mass Analyzers. *Drug Test. Anal.* **2018**, *10* (1), 28–36. <https://doi.org/10.1002/dta.2249>.
- (24) McAlister, G. C.; Phanstiel, D. H.; Brumbaugh, J.; Westphall, M. S.; Coon, J. J. Higher-Energy Collision-Activated Dissociation Without a Dedicated Collision Cell. *Mol. Cell. Proteomics* **2011**, *10* (5), O111.009456. <https://doi.org/10.1074/mcp.O111.009456>.
- (25) Searcy, J. Q.; Fenn, J. B. Clustering of Water on Hydrated Protons in a Supersonic Free Jet Expansion. *J. Chem. Phys.* **1974**, *61* (12), 5282–5288. <https://doi.org/10.1063/1.1681876>.

## CHAPTER 4. THE EFFECTS OF ANALYTE CONCENTRATION ON THE PROTONATION SITES OF 4-AMINOBENZOIC ACID UPON APCI AS REVEALED BY GAS-PHASE ION-MOLECULE REACTIONS

### 4.1 Introduction

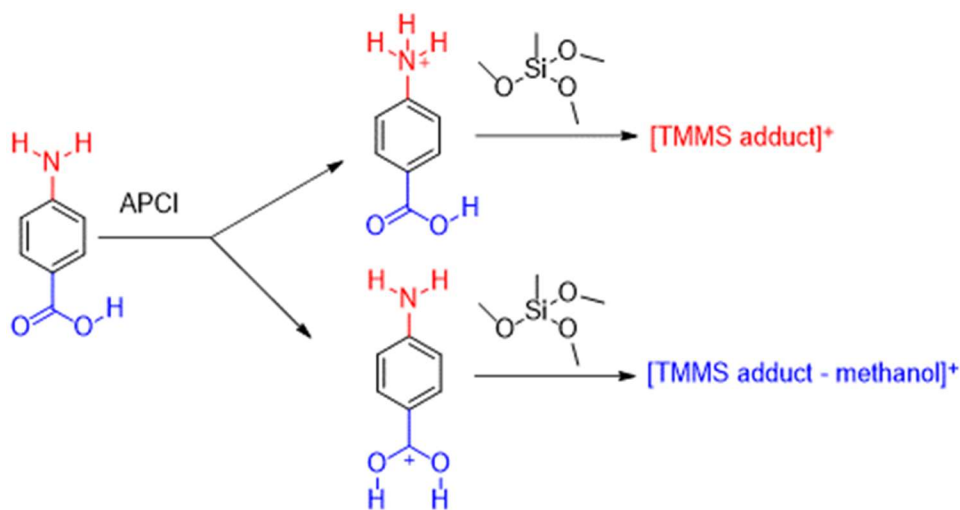
Identification of drug metabolites is extremely important for understanding the metabolic activities of drugs, which is required for FDA approval.<sup>1-3</sup> Commonly used techniques for the structural elucidation and identification of drug metabolites include NMR spectroscopy, X-ray crystallography, liquid chromatography coupled with mass spectrometry (LC-MS) and tandem mass spectrometry (MS<sup>n</sup>).<sup>2</sup> However, NMR spectroscopy and X-ray crystallography require relatively large amounts of pure samples, which may not be available. In contrary, tandem mass spectrometric methods do not require pure samples or large amounts of sample. Tandem mass spectrometric analysis based on collision-activated dissociation (CAD) often generates similar fragmentation patterns for isomeric ionized compounds.<sup>4</sup> Hence, numerous functional group-selective gas-phase ion-molecule reactions have been developed to distinguish between isomeric compounds with/without similar functional groups.<sup>5-7</sup>

In polyfunctional analytes containing multiple plausible protonation sites, two or more sites may have similar gas-phase proton affinities. If these sites with similar proton affinities are also the most basic sites, these analytes may get protonated at several sites.<sup>5</sup> Ionization solvents and ion source conditions may influence the preferred protonation sites.<sup>8-10</sup> For gas-phase ion-molecule reactions that are not initiated by proton transfer from a protonated analyte to the neutral reagent, the site of reaction in the analyte is often controlled by the site of protonation.<sup>11</sup> Hence it is crucial to understand the factors controlling the manifested protonation sites.

4-Aminobenzoic acid, a bifunctional analyte containing functional groups with similar proton affinities, is one of the most widely studied compounds in investigations of factors controlling protonation sites.<sup>8,12-17</sup> In solution, the most basic site of 4-aminobenzoic acid is the amino nitrogen while calculations suggest that the carbonyl oxygen is the most basic site in the gas phase.<sup>8</sup> Fragmentation patterns obtained using collision-activated dissociation (CAD) have revealed that electrospray ionization (ESI) of 4-aminobenzoic acid dissolved in 3-1 (v/v) methanol-water predominantly prefers protonation on the carbonyl oxygen whereas the same dissolved in 1-1 (v/v) acetonitrile-water prefers protonation on the amino nitrogen.<sup>8,16</sup> Another

study reported that the size and nature of solvent clusters present during the desolvation process of electrospray ionization affected the manifested protonation sites.<sup>13</sup> In clusters containing 3-7 methanol molecules, a solvent bridge was proposed to be formed between the two protonation sites, leading to shuffling of a proton from the amino nitrogen (favored in solution) onto the carbonyl oxygen (favored in the gas phase).<sup>13</sup> On the contrary, in the presence of  $\leq 2$  or  $\geq 8$  methanol molecules, the proton was suggested to remain on the amino nitrogen (favored in solution).<sup>13</sup>

ESI is one of the most commonly used techniques for ionization of polar analytes whereas atmospheric pressure chemical ionization (APCI) can be used to ionize analytes with low polarity.<sup>18,19</sup> Most of the investigations regarding protonation sites of 4-aminobenzoic acid have been carried out using ESI.<sup>8,16</sup> So far, only one study using APCI has been published. This study reported fragmentation patterns that suggested that a higher infusion rate (50  $\mu\text{L}/\text{min}$ ) of 4-aminobenzoic acid dissolved in 2-1 (v/v) acetonitrile-water led to predominant generation of the N-protomer whereas at low infusion rates (5  $\mu\text{L}/\text{min}$ ), both N- and O-protomers were generated in almost equal amounts.<sup>20</sup> However, the effects of other parameters, such as the ionization solvent or analyte concentration on the manifested protonation sites of 4-aminobenzoic acid ionized via APCI have not been studied so far.



Scheme 4.1 Gas-phase ion-molecule reactions of the two protomers of 4-aminobenzoic acid with trimethoxymethylsilane (TMMS)

CAD is commonly used for structural elucidation of protomers in tandem mass spectrometry experiments.<sup>8,15,16</sup> However, this method is inadequate for the identification of protomers of 4-aminobenzoic acid in linear quadrupole ion traps (LQIT) because LQITs contain significant amount of residual moisture that can change the protonation site during CAD.<sup>21</sup> In this study, previously known<sup>22</sup> gas-phase ion-molecule reactions of trimethoxymethylsilane (TMMS) with amines and aromatic carboxylic acids have been employed to identify the protonation sites of 4-aminobenzoic acid (**Scheme 4.1**). The results suggest that both analyte concentration and ionization solvent system determine the manifested protonation sites.

## 4.2 Experimental

### 4.2.1 Chemicals

4-Aminobenzoic acid, benzoic acid, aniline, 4-chloroaniline, methyl 4-aminobenzoate and trimethoxymethylsilane (TMMS) were purchased from Sigma Aldrich. Aniline and benzoic acid had a purity of  $\geq 99.5$  % while 4-chloroaniline, trimethoxymethylsilane and methyl-4-aminobenzoate had a purity of 98 %. 4-Aminobenzoic acid had purity of  $\geq 99\%$  whereas trimethoxymethylsilane had a purity of 98%. LC-MS grade methanol, water and acetonitrile were purchased from Thermo Fisher Scientific. All the chemicals were used without further purification.

### 4.2.2 Sample Preparation

Two different solvent systems, methanol and 1-1 (v/v) acetonitrile-water, were used to prepare solutions of 4-aminobenzoic acid at the following analyte concentrations (in M):  $10^{-9}$ ,  $10^{-8}$ ,  $10^{-7}$ ,  $10^{-6}$ ,  $10^{-5}$ ,  $10^{-4}$ ,  $10^{-3}$ . Solutions containing aniline, benzoic acid, 4-chloroaniline and methyl 4-aminobenzoate at analyte concentrations of  $10^{-5}$  M were prepared using methanol as the solvent.

### 4.2.3 Instrumentation

A linear quadrupole ion trap (LQIT) mass spectrometer equipped with an APCI source was used for all the experiments. The APCI source was operated in positive ion mode with nitrogen as the sheath and auxiliary gas. The analyte solutions were introduced into the APCI source by using a 500  $\mu$ L Hamilton syringe at a flow rate of 50  $\mu$ L/min. Following are the parameters of the APCI source used to ensure maximum signal for the analyte ions: vaporizer temperature: 300 °C,

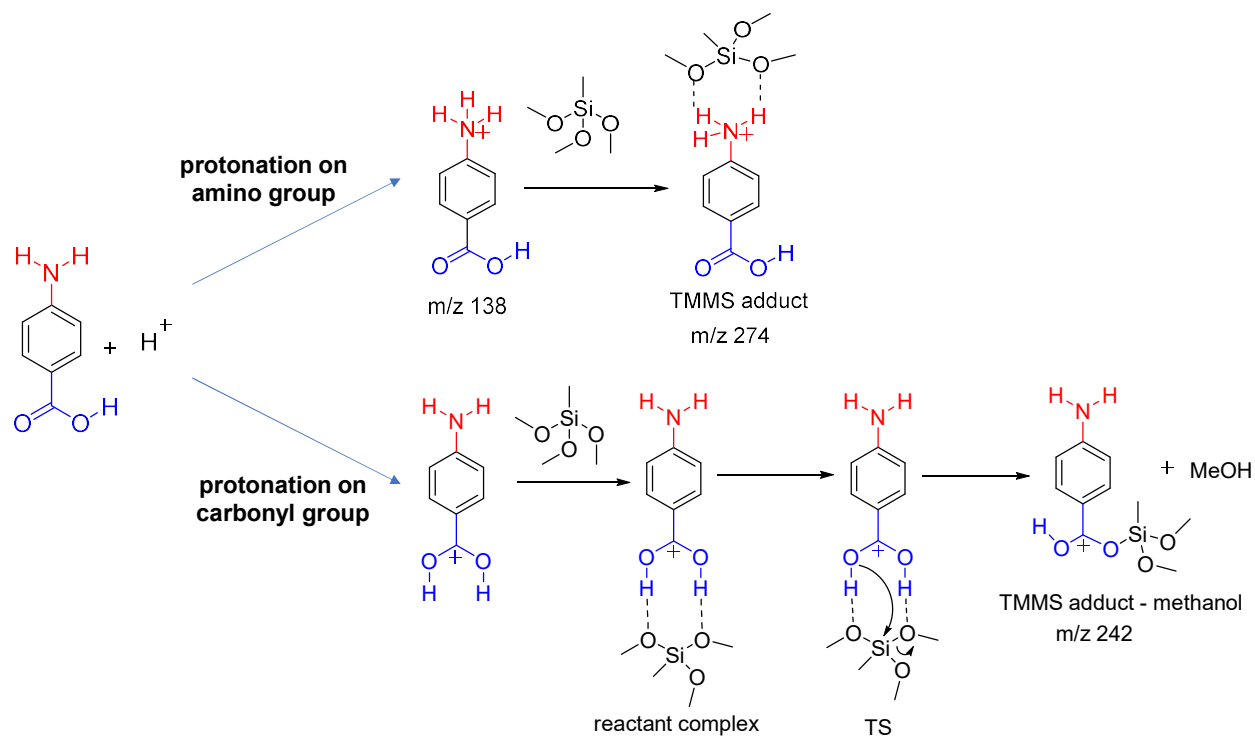
capillary temperature: 250 °C, sheath gas (N<sub>2</sub>) flow rate: 30 (arbitrary units), auxiliary gas (N<sub>2</sub>) flow rate: 10 (arbitrary units), capillary voltage: 5 kV. An ion isolation width of 2 m/z units and a q of 0.25 was used for the isolation of ions. After isolation of ions, the ions were allowed to react with TMMS for 300 ms followed by detection of all ions by using the electron multipliers located on the two sides of the ion trap.

An external home-built manifold was used to inject TMMS into the ion trap.<sup>23–25</sup> The manifold was maintained at a temperature of 125 °C to ensure complete evaporation of TMMS. A syringe pump maintained at a flow rate of 6 μL/h was used to inject TMMS into the trap. The reagent was diluted with helium at a flow rate of 0.6 L/h and was introduced into the ion trap by using a Granville-Phillips leak valve.

### 4.3 Results and Discussions

Prior to the investigation of 4-aminobenzoic acid, gas-phase ion-molecule reactions of protonated aniline with TMMS was examined in the ion trap as previous studies.<sup>22</sup> Aniline was dissolved in pure methanol, ionized using APCI and was introduced into the mass spectrometer. Protonated aniline was isolated in the ion trap and allowed to react with TMMS. A stable adduct was slowly generated (Figure 1), that indicated that gas-phase ion-molecule reactions with TMMS can be used to differentiate between the protomers of protonated 4-aminobenzoic acid.

TMMS reacts with protonated amines to form an adduct (TMMS adduct) but with protonated carboxylic acids to generate product whose m/z corresponds to an adduct that has lost a methanol molecule (TMMS adduct - MeOH).<sup>22</sup> Hence, in the case of gas-phase ion-molecule reactions with protonated 4-aminobenzoic acid, generation of TMMS adduct (m/z 274) should indicate formation of N-protomer whereas generation of [TMMS adduct-methanol] (m/z 242) should indicate formation of the O-protomer. The mechanism based on a previously published report<sup>22</sup> is shown in **Scheme 4.2**. 4-Aminobenzoic acid was dissolved in pure methanol or 1-1 (v/v) acetonitrile-water at various concentrations, ionized using APCI, transferred into the ion trap, isolated, and allowed to react with TMMS for 300 ms. The results obtained when 4-aminobenzoic acid was dissolved in methanol are discussed first followed by those obtained when 1-1 (v/v) acetonitrile-water was used as the ionization solvent.



Scheme 4.2 Proposed mechanisms of the gas-phase ion-molecule reactions between trimethoxymethylsilane (TMMS) and the protonated forms of 4-aminobenzoic acid. TS indicates transition state<sup>22</sup>

The mass spectra (MS/MS) recorded for such experiments are shown in **Figure 4.1**. As evident from **Figures 4.1a** to **4.1d**, [TMMS adduct-methanol]<sup>+</sup> was the predominant product at low analyte concentrations. The abundances of TMMS adduct and [TMMS adduct-methanol]<sup>+</sup> were similar in **Figure 4.1e** whereas at higher analyte concentrations (10<sup>-4</sup> M), TMMS adduct was the major product. These results indicated that the abundance of N-protomer increased with increasing analyte concentration. For accurate analysis of the data, the relative rates of the reactions of the two protomers with TMMS were investigated via model compound studies.

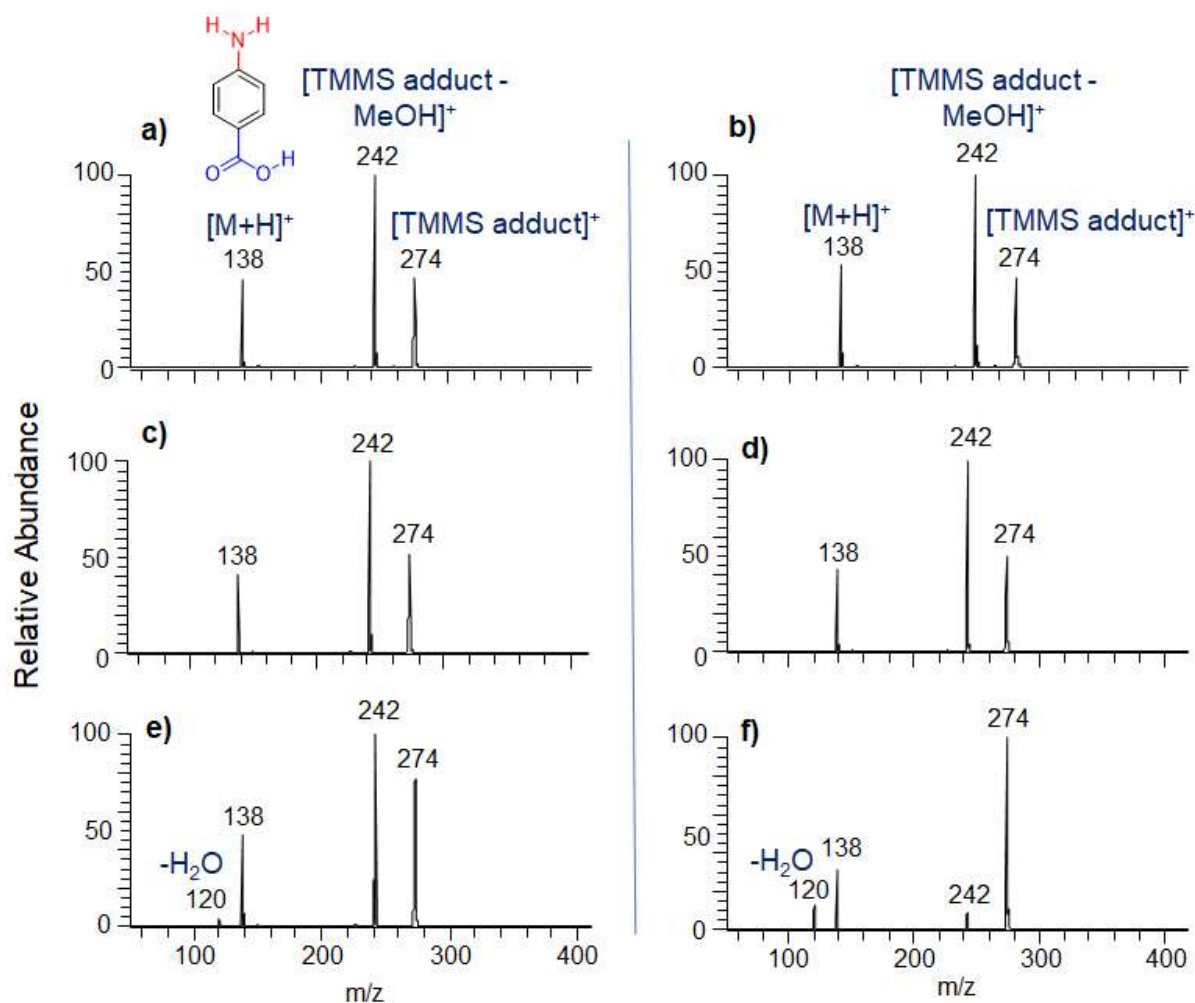


Figure 4.1 MS<sup>2</sup> spectra measured after 300 ms gas-phase ion-molecule reactions between TMMS and protonated 4-aminobenzoic acid (dissolved in methanol) ionized using positive ion mode APCI. The MS/MS spectra were collected at analyte concentrations of a) 10<sup>-9</sup> M, b) 10<sup>-8</sup> M, c) 10<sup>-7</sup> M, d) 10<sup>-6</sup> M, e) 10<sup>-5</sup> M and f) 10<sup>-4</sup> M

Protonated benzoic acid (proton affinity (PA) 196.3 kcal/mol<sup>26</sup>) and protonated aniline (PA 210.9 kcal/mol<sup>26</sup>) were allowed to react with TMMS (PA ~202 kcal/mol as calculated previously at the B3LYP/6-31++G(d,p) level of theory). Protonated benzoic acid predominantly generated an adduct (m/z 227) that had lost a methanol molecule whereas protonated aniline predominantly generated a stable adduct (m/z 230) (**Figure 4.2**). Protonated benzoic acid was also observed to react with TMMS about ten times faster than protonated aniline. This may be due to the low PA of benzoic acid which enables an exothermic proton transfer (exothermic by 6 kcal/mol) to TMMS causing fast dissociation of the complex via loss of methanol (**Scheme 4.2**). Proton transfer from protonated aniline however is less likely (endothermic by ~9 kcal/mol) leading to slow formation of stable adduct. However, PAs of the protomers of 4-aminobenzoic acid are much closer to each other and therefore different reactivity is expected. Both the PA of carbonyl oxygen (~207 kcal/mol) and the amino nitrogen (~201 kcal/mol) are close to PA of TMMS (~202 kcal/mol). Therefore, the reactivity difference between the two protomers can be expected to be much smaller than that for aniline and benzoic acid.

For an appropriate comparison and to obtain an estimate for the reactivities for the two protomers, additional model compounds were investigated. Two model compounds (4-chloroaniline and methyl 4-aminobenzoate) having similar PAs as the protomers of 4-aminobenzoic acid were chosen. PA of 4-chloroaniline is 208.8<sup>26</sup> kcal/mol which is close to PA of the carbonyl oxygen (~207 kcal/mol) in 4-aminobenzoic acid whereas the PA of methyl 4-aminobenzoate is 201.3 kcal/mol, similar to the amino nitrogen (~ 201 kcal/mol) of 4-aminobenzoic acid. As expected from the PA values protonated 4-chloroaniline was observed to react faster than protonated aniline whereas methyl 4-aminobenzoate was observed to react substantially slower than protonated benzoic acid (**Figure 4.2**). It is noteworthy that protonated methyl 4-aminobenzoate reacts with TMMS via adduct formation about 90 times slower than protonate benzoic acid and four times slower than 4-chloroaniline. Comparing the PAs of the model compounds and the protonation sites of 4-aminobenzoic acid, O-protomers are expected to have reactivities similar to protonated 4-chloroaniline whereas the N-protomers are expected to have reactivities similar to protonated methyl 4-aminobenzoate and the O-protomers are expected to react with TMMS about four times faster than the N-protomer.

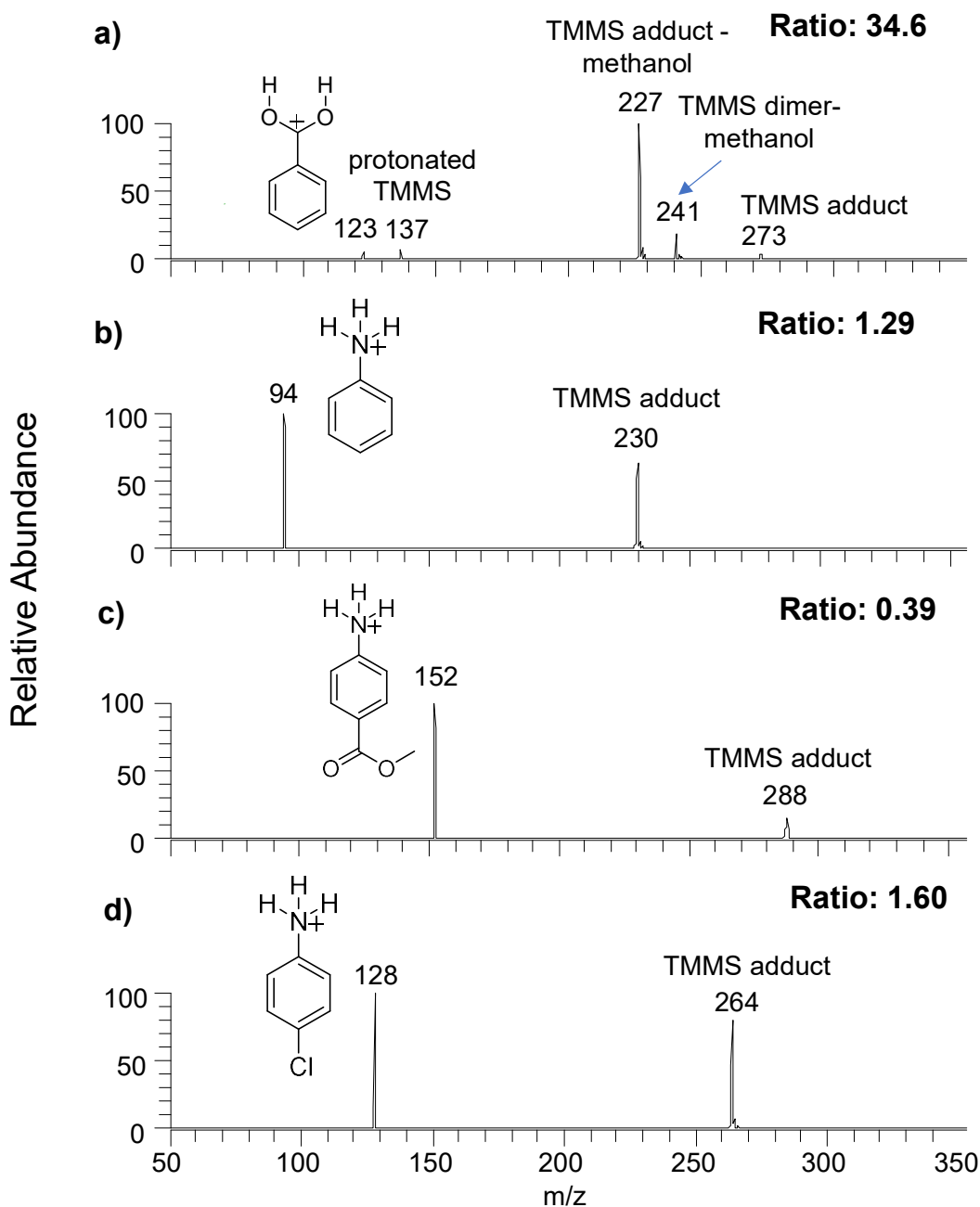


Figure 4.2 Mass spectra recorded after 300 ms gas-phase ion-molecule reactions between TMMS and a) protonated benzoic acid b) protonated aniline c) protonated methyl-4-aminobenzoate and d) protonated 4-chloroaniline. The indicated ratio corresponds to the sum of the abundances of all the product ions divided by the abundance of the reactant ions after reaction time of 300 ms.

Based on the above discussions results shown in **Figure 4.1**, at low analyte concentrations, in methanol solvent the abundance of the N-protomer was about twice the abundance of the O-protomer. At higher analyte concentrations, the amino nitrogen was the predominant site of protonation. These results are interesting because a) the results suggest that analyte concentrations play significant role on the manifested protonation sites upon APCI although previous reports suggested that analyte concentrations do not affect the protonation sites upon ESI.<sup>10</sup> and b) results suggest that N-protomer dominates at all analyte concentrations although a previous report<sup>20,27</sup> for a similar model compound, dimethylaminochalcone showed that only O-protomer was generated upon APCI in presence of methanol as the ionization solvent. The plausible reasons for these observations are explained below.

A previously published report based on density functional theory found that solvent clusters containing 3-8 methanol molecules can form a solvent bridge between the protonation sites and transfer the proton from the amino nitrogen (favored in solution) onto the carbonyl oxygen (favored in the gas phase).<sup>13</sup> On the contrary, if the number of methanol is  $\leq 2$ , a solvent bridge cannot be formed, leading to trapping of the proton on the amino nitrogen. If the number of methanol molecules in the cluster is  $\geq 8$ , protonated analytes are suggested to behave as if they were in solution; i.e., generation of the N-protomer dominates (favored in solution).<sup>13</sup> Predominant formation of N-protomers in the current study can be explained as the following: initially formed the O-protomers upon APCI in presence of  $> 8$  methanol molecules in solvent clusters can convert to N-protomers. This hypothesis can be supported by recent studies showing residual moisture in ion trap can form solvent clusters around analyte ions and affecting the manifested protonation sites.<sup>28</sup> APCI source is also expected to contain significant amount of methanol molecules during ionization which may allow formation of bigger solvent clusters around analyte ions, resulting in conversion of initially formed O-protomer to N-protomer.

Increased abundance of N-protomers with respect to O-protomers at high analyte concentrations are discussed next. A previous study showed that long-lived proton bound dimers of 4-aminobenzoic acid can be formed during ESI which survived the ion desolvation process and affected the manifested protonation sites.<sup>17</sup> In order to understand whether proton-bound dimers are responsible for the generation of the N-protomers at high analyte concentration, further experiments were performed. All the ions entering the mass spectrometer, prior to isolation were investigated. **Figure 4.3** shows the mass spectra recorded at analyte concentrations of  $10^{-5}$  M and

$10^{-4}$  M. As shown in **Figure 4.3a**, only protonated 4-aminobenzoic acid was detected at low analyte concentrations. This may be because methanol adducts have been reported to be unstable.<sup>17</sup> At higher analyte concentrations ( $\geq 10^{-4}$  M), proton bound dimers ( $m/z$  275) of 4-aminobenzoic acid were observed along with methanol adducts ( $m/z$  170) of 4-aminobenzoic acid (Figure 3b). Proton bound dimers of 4-aminobenzoic acid have been previously reported to be more stable than methanol adducts.<sup>17</sup> This suggests that proton-bound dimer may be responsible for the predominant generation of N-protomer at high analyte concentration. However, the proton-bound dimers can fragment to generate either the N- or the O-protomer. Hence further experiments were performed to determine the structure of the dimer formed

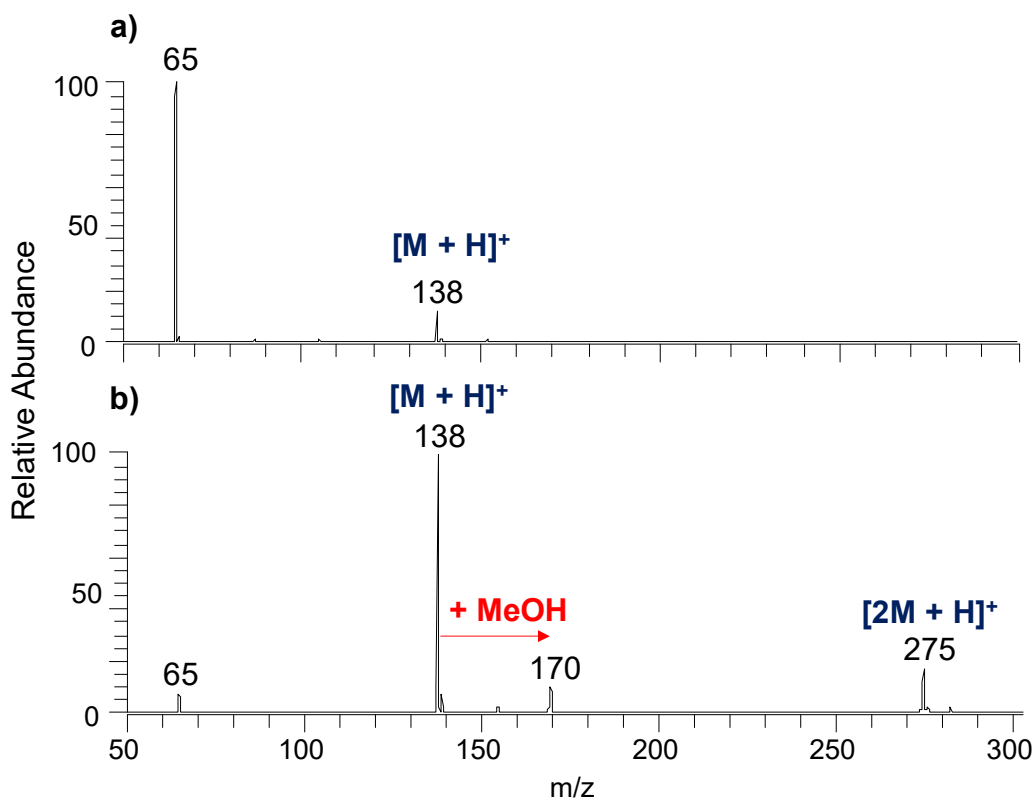


Figure 4.3 Mass spectra measured for methanol solutions of 4-aminobenzoic acid (MW 137 Da) ionized using positive ion mode APCI at concentrations of a)  $10^{-5}$  M and b)  $10^{-4}$  M. Ion of  $m/z$  275 corresponds to a protonated dimer of 4-aminobenzoic acid. Ion of  $m/z$  170 corresponds to a methanol adduct of protonated 4-aminobenzoic acid.

Five plausible structures exist for the proton bound dimer of protonated 4-aminobenzoic acid and neutral 4-aminobenzoic acid (**Figure 4.4**). Calculations in a previously published study<sup>17</sup> showed that dimers O1, O2 and O3 are more stable than dimers N1, N2 and N3 in the gas phase whereas dimers N1, N2 and N3 are more stable than O1, O2 and O3 in water. Calculations in the same study revealed that dimer N1 is the most stable dimer generated in water. In the same study, experiments using IR spectroscopy studies showed that a mixture of N1 and N2 is formed, suggesting that the dimers are formed during ionization process. According to the study,<sup>17</sup> dimers N1 and N2 can survive the desolvation process before dissociating in vacuum in the mass spectrometer. In the current studies using APCI, dimers O1, O2 and O3 are expected to be formed.

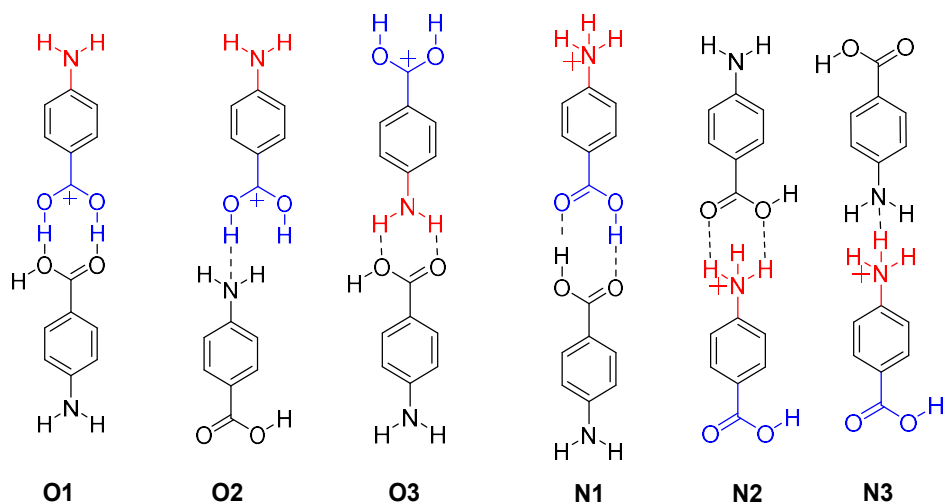
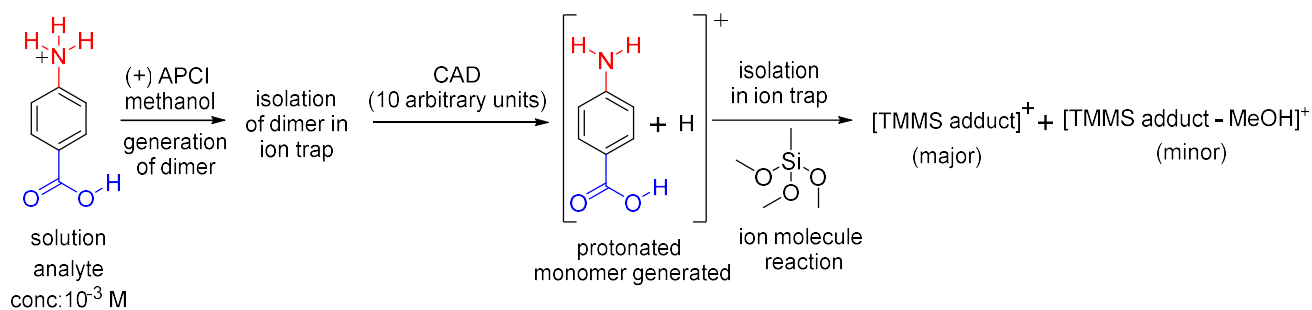


Figure 4.4 Possible structures of the proton-bound dimer of 4-aminobenzoic acid. O1, O2 and O3 correspond to structures where the carbonyl oxygen is protonated (calculated<sup>15</sup> to be more stable in the gas phase) while N1, N2 and N3 correspond to structures where the amino nitrogen is protonated (calculated<sup>15</sup> to be more stable in water).

According to Cooks' kinetic method developed for the accurate measurement of proton affinities of gaseous Bronsted bases, proton bound adducts of two bases fragment upon CAD in such a manner that the base with the greater proton affinity is predominantly protonated.<sup>29,30</sup> In the case of 4-aminobenzoic acid, the most basic site in the gas phase is the carbonyl oxygen whereas in solution, the most basic site is the amino nitrogen. Hence dimers O1, O2 and O3 generated during APCI are expected to dissociate and predominantly generate the O-protomers. On the contrary dimer N1 can fragment to form only the N-protomer. Further experiments were performed

to investigate the structure of the dimer formed. A methanol solution containing 4-aminobenzoic acid at a concentration of  $10^{-3}$  M was introduced into the ion trap. Protonated dimer ( $m/z$  275) was isolated and subjected to CAD to generate 4-aminobenzoic acid (**Scheme 4.3**) which was isolated and allowed to react with TMMS. TMMS adduct was predominantly formed (**Figure 4.5**) which suggests predominant formation of the N-protomer after dissociation of the proton-bound dimer. This result also suggests that most likely dimer N1 was formed upon APCI which fragmented to generate the N-protomers. These results are interesting for two reasons: 1) The proton bound dimer of 4-aminobenzoic acid may be responsible for the predominant formation of the N-protomers at high analyte concentrations (**Scheme 4.4**) and 2) dimer N1 observed to be formed during APCI was reported by previously published manuscripts to be more stable in water, indicating that the mechanisms for APCI and ESI are similar. This is in agreement with recent studies that showed that compounds having ionization efficiency in ESI also have high ionization efficiencies in APCI.<sup>19</sup>



Scheme 4.3 Isolation of the gaseous proton bound dimer (generated during APCI) of 4-aminobenzoic acid followed by CAD to generate protonated 4-aminobenzoic acid that was isolated in the ion trap and allowed to react with TMMS

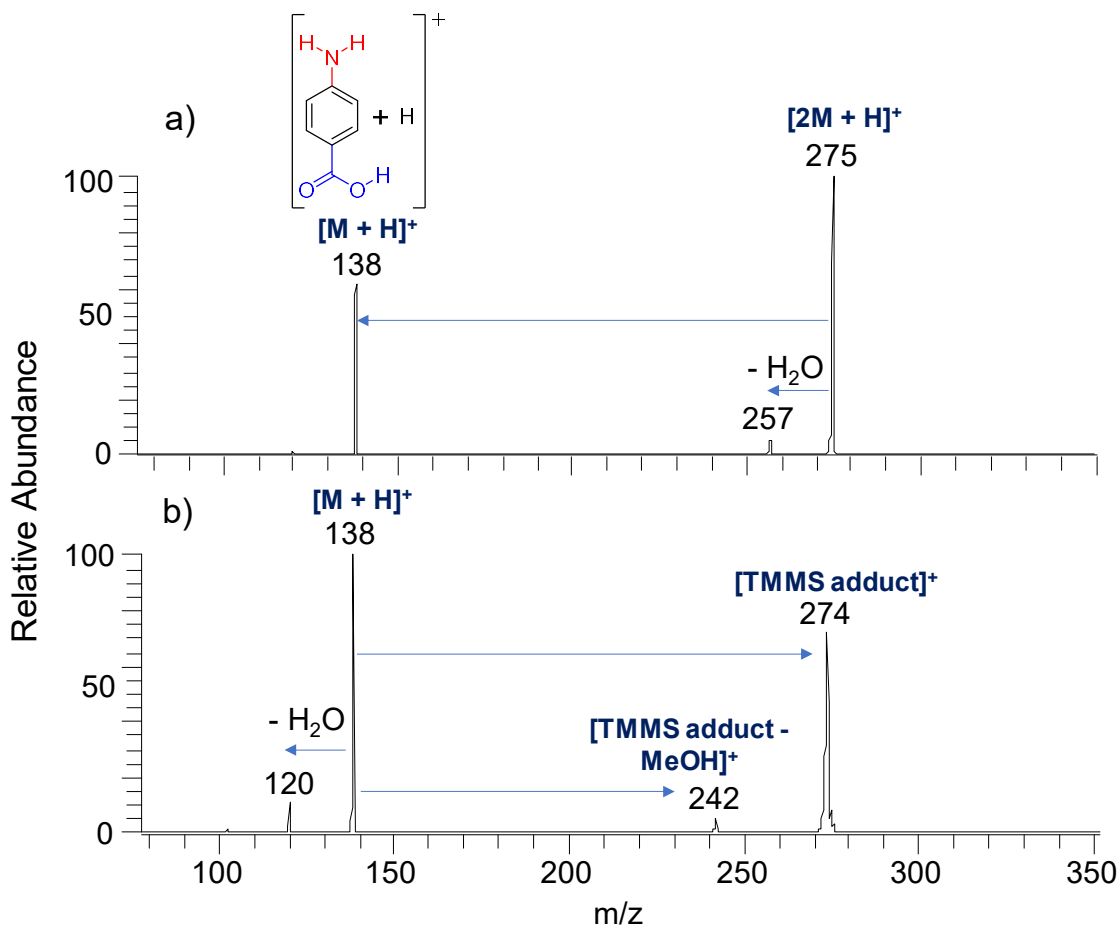
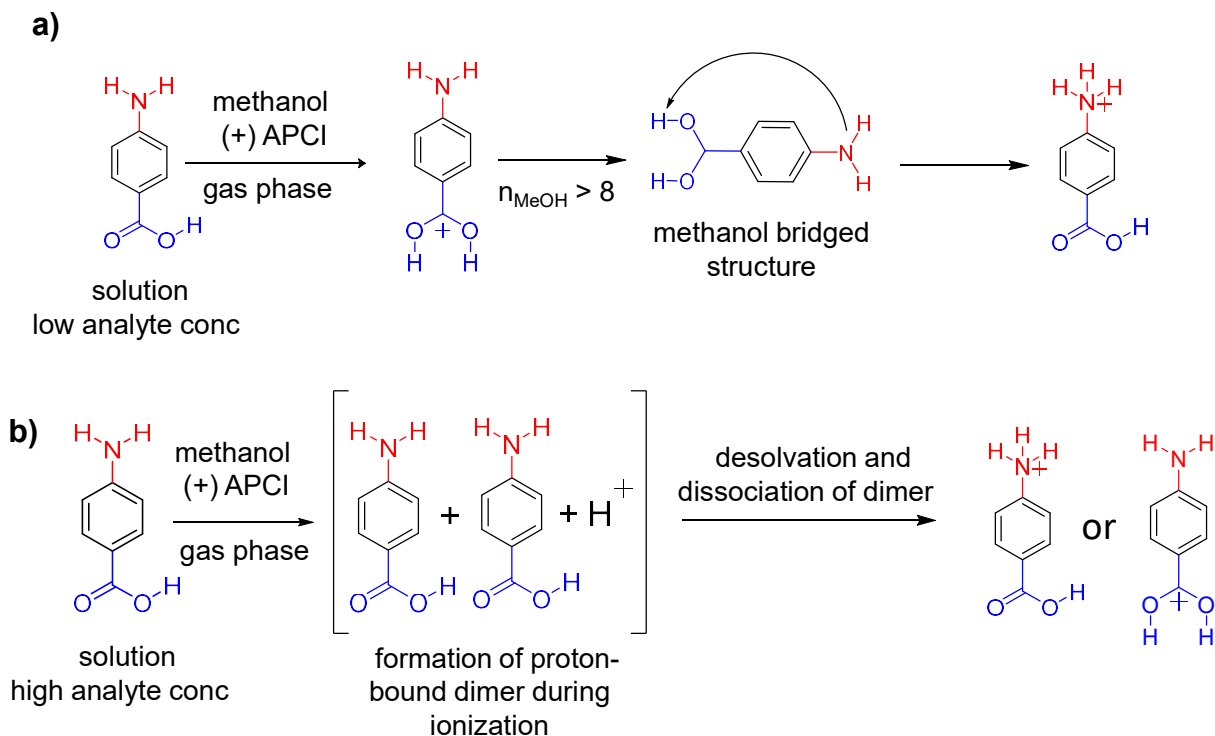


Figure 4.5 a) MS<sup>3</sup> spectrum measured after isolation of the gaseous proton bound dimer ([2M+H]<sup>+</sup>; m/z 275) of protonated 4-aminobenzoic acid formed in the ion trap followed by CAD (collision energy: 10 arbitrary units) generates protonated 4-aminobenzoic acid ([M+H]<sup>+</sup>; m/z 138). b) Isolation of protonated 4-aminobenzoic acid (m/z 138) followed by 300 ms reactions with trimethoxymethylsilane (MS<sup>4</sup>).



Scheme 4.4 Mechanisms proposed for tautomerization of the protomers of 4-aminobenzoic acid in 1-1 (v/v) acetonitrile-water during ion transfer, when concentrations of a)  $\leq 10^{-5}$  M and b)  $\geq 10^{-4}$  M were used.

Intrigued by above results, the effects of concentration on the protonation sites of 4-aminobenzoic acid dissolved in 1-1 (v/v) acetonitrile-water were next investigated. **Figure 4.6** shows MS/MS spectra measured after gas-phase ion-molecule reactions for 300 ms between TMMS and the protomers of 4-aminobenzoic acid at concentrations varying from  $10^{-9}$  M to  $10^{-4}$  M. TMMS adduct was the predominant product observed for all concentrations. This result suggests that in the presence of 1-1 (v/v) acetonitrile-water, proton remains trapped on the amino nitrogen, leading to predominant generation of the N-protomer. This observation is in agreement with previously published studies for ESI that found that the amino group is predominantly protonated in acetonitrile-water.<sup>8,14,16,17</sup> This has been rationalized based on the formation of a stable adduct between acetonitrile and protonated 4-aminobenzoic acid that leads to the trapping of the proton onto the amino nitrogen.<sup>17</sup>

Intrigued by above results, the effects of concentration on the protonation sites of 4-aminobenzoic acid dissolved in 1-1 (v/v) acetonitrile-water were next investigated. **Figure 4.4** shows MS/MS spectra measured after gas-phase ion-molecule reactions for 300 ms between

TMMS and the protomers of 4-aminobenzoic acid at concentrations varying from  $10^{-9}$  M to  $10^{-4}$  M. TMMS adduct was the predominant product observed for all concentrations. This result suggests that in the presence of 1-1 (v/v) acetonitrile-water N-protomer was predominantly generated irrespective of analyte concentrations. This can be explained by the formation of bulky water clusters which are formed during APCI, leading to the formation of protomers favored in solution, the N-protomers.

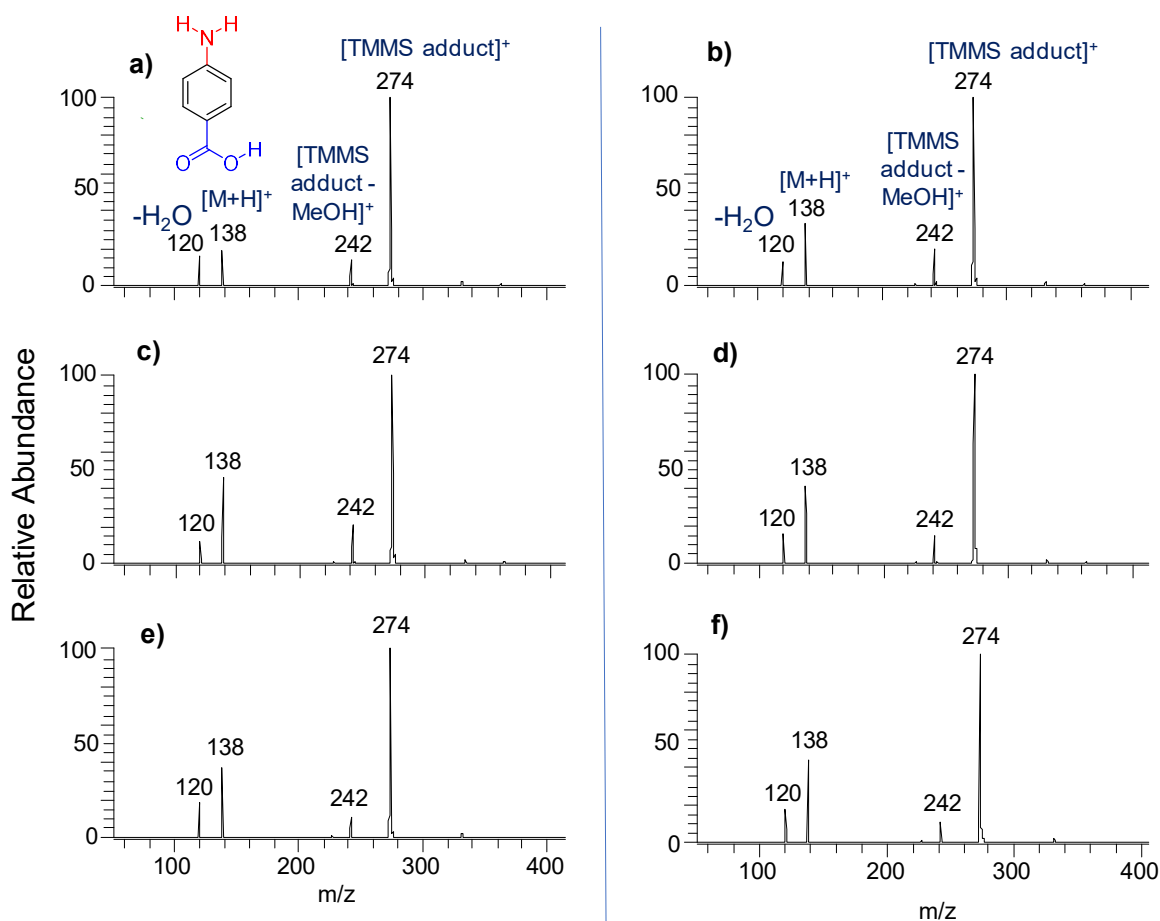


Figure 4.6 MS<sup>2</sup> spectra measured after the gas-phase ion-molecule reactions for 300 ms between TMMS and protonated 4-aminobenzoic acid (dissolved in 1-1 (v/v) acetonitrile-water) ionized using positive ion mode APCI. The MS/MS spectra were collected at concentrations of a)  $10^{-9}$  M, b)  $10^{-8}$  M, c)  $10^{-7}$  M, d)  $10^{-6}$  M, e)  $10^{-5}$  M and f)  $10^{-4}$  M

Next all the ions/adduct formed when 4-aminobenzoic acid was sprayed with 1-1 (v/v) acetonitrile-water were investigated and the mass spectra recorded are shown in **Figure 4.7**. **Figure 4.7** shows that acetonitrile adducts both at high and low analyte concentrations. In addition,

at high analyte concentrations ( $\geq 10^{-4}$  M), formation of proton bound dimers of 4-aminobenzoic acid ( $[2M+H]^+$ ) was also observed (Figure 7). This indicated that proton bound dimers both may be responsible for the generation of N-protomer at high analyte concentrations.

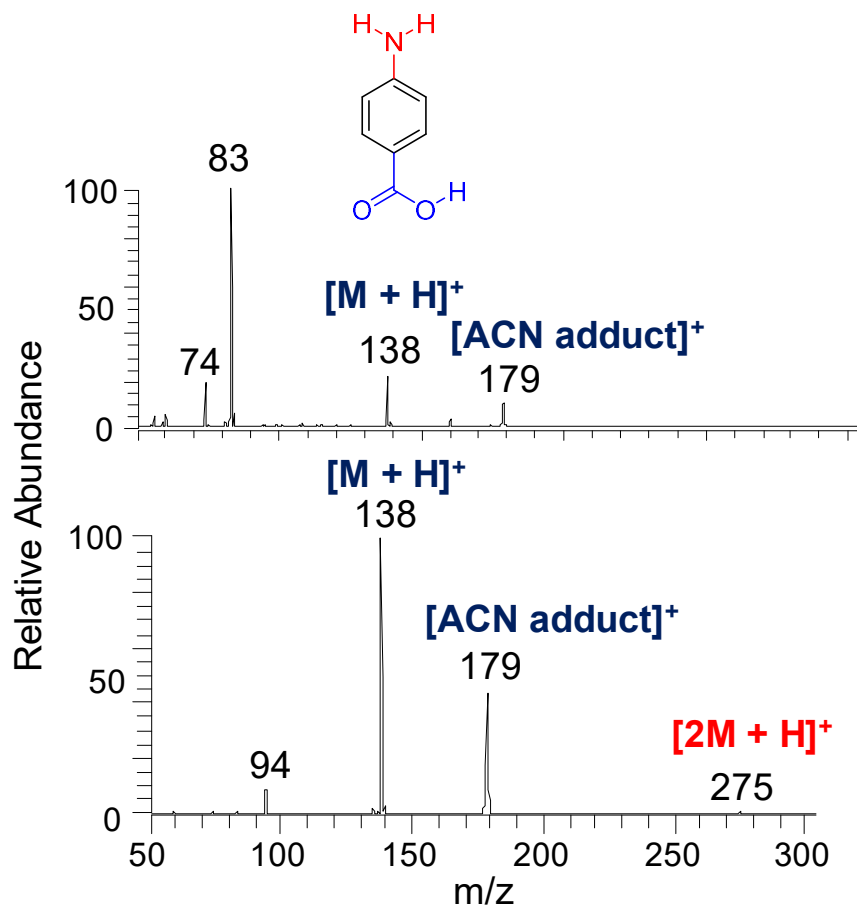


Figure 4.7 Mass spectra measured for solutions of 4-aminobenzoic acid in 1-1 (v/v) acetonitrile-water ionized using APCI for analyte concentrations a)  $10^{-5}$  M and b)  $10^{-4}$  M. ACN indicates acetonitrile. Ion of m/z 83 corresponds to a protonated dimer of acetonitrile

#### 4.4 Conclusions

In this study, preferred protonation sites in 4-aminobenzoic acid have been identified using functional group-selective gas-phase ion-molecule reactions. Trimethoxymethylsilane (TMMS) reacts with protonated amines to generate TMMS adduct and with protonated carboxylic acids to generate TMMS adduct-methanol. Protonated carboxylic acids react with TMMS about four times

faster than protonated amino groups. This functional group-selective reactivity of TMMS has been exploited in this study to identify N- and O-protomers of 4-aminobenzoic acid.

In this study, analyte concentration was observed to play a significant role in the manifested protonation sites of 4-aminobenzoic acid when ionized using positive mode APCI and methanol as the ionization solvent. At low analyte concentrations, the abundance of N-protomer generated was about twice the abundance of O-protomers. This result is in contrast to the popular notion that APCI predominantly involves gas-phase ions and is expected to generate the O-protomer. This observation can be rationalized based on previous studies<sup>13</sup> that showed that in the presence of solvent clusters containing large clusters of solvent molecules (> 8 methanol molecules) during ionization can initially formed O-protomers can get converted to N-protomers.

At high analyte concentrations, N-protomers were formed exclusively. This may be due to the formation of proton-bound dimers of 4-aminobenzoic acid. These dimers may survive the desolvation step and travel through ion optics region before fragmenting to generate the N-protomer. Interestingly, experimental results suggest that the structure of the dimer observed corresponds to those preferred in solution, not in gas phase.

When 1-1 (v/v) acetonitrile-water was used as the ionization solvent, amino nitrogen was the predominant site of protonation irrespective of analyte concentration. This can be rationalized based on the formation of bigger water clusters during APCI. In presence of bigger solvent clusters 4-aminobenzoic acid behaves as if it is bulk solution, leading to the manifestation of the N-protomer. Above results indicate that ESI-like solution chemistry is important during APCI in contrast to the popular belief that APCI produce gaseous ions.

## 4.5 References

- (1) Ma, S.; Chowdhury, S. K. Analytical Strategies for Assessment of Human Metabolites in Preclinical Safety Testing. *Anal. Chem.* **2011**, *83* (13), 5028–5036. <https://doi.org/10.1021/ac200349g>.
- (2) Wen, B.; Zhu, M. Applications of Mass Spectrometry in Drug Metabolism: 50 Years of Progress. *Drug Metab. Rev.* **2015**, *47* (1), 71–87. <https://doi.org/10.3109/03602532.2014.1001029>.
- (3) Gao, H.; Jacobs, A.; White, R. E.; Booth, B. P.; Obach, R. S. Meeting Report: Metabolites in Safety Testing (MIST) Symposium—Safety Assessment of Human Metabolites: What’s REALLY Necessary to Ascertain Exposure Coverage in Safety Tests? *AAPS J.* **2013**, *15* (4), 970–973. <https://doi.org/10.1208/s12248-013-9502-6>.

- (4) Zhang, M.; Eismin, R.; Kenttämäa, H.; Xiong, H.; Wu, Y.; Burdette, D.; Urbanek, R. Identification of 2-Aminothiazolobenzazepine Metabolites in Human, Rat, Dog, and Monkey Microsomes by Ion-Molecule Reactions in Linear Quadrupole Ion Trap Mass Spectrometry. *Drug Metab. Dispos.* **2015**, *43* (3), 358–366. <https://doi.org/10.1124/dmd.114.061978>.
- (5) Sheng, H.; Williams, P. E.; Tang, W.; Riedeman, J. S.; Zhang, M.; Kenttämäa, H. I. Identification of the Sulfone Functionality in Protonated Analytes via Ion/Molecule Reactions in a Linear Quadrupole Ion Trap Mass Spectrometer. *J. Org. Chem.* **2014**, *79* (7), 2883–2889. <https://doi.org/10.1021/jo402645a>.
- (6) Tang, W.; Sheng, H.; Kong, J. Y.; Yerabolu, R.; Zhu, H.; Max, J.; Zhang, M.; Kenttämäa, H. I. Gas-phase Ion–Molecule Reactions for the Identification of the Sulfone Functionality in Protonated Analytes in a Linear Quadrupole Ion Trap Mass Spectrometer. *Rapid Commun. Mass Spectrom.* **2016**, *30* (12), 1435–1441. <https://doi.org/10.1002/rcm.7569>.
- (7) Zhu, H.; Max, J. P.; Marcum, C. L.; Luo, H.; Abu-Omar, M. M.; Kenttämäa, H. I. Identification of the Phenol Functionality in Deprotonated Monomeric and Dimeric Lignin Degradation Products via Tandem Mass Spectrometry Based on Ion–Molecule Reactions with Diethylmethoxyborane. *J. Am. Soc. Mass Spectrom.* **2016**, *27* (11), 1813–1823. <https://doi.org/10.1007/s13361-016-1442-9>.
- (8) Tian, Z.; Kass, S. R. Gas-Phase versus Liquid-Phase Structures by Electrospray Ionization Mass Spectrometry. *Angew. Chem. Int. Ed.* **2009**, *48* (7), 1321–1323. <https://doi.org/10.1002/anie.200805392>.
- (9) Warnke, S.; Seo, J.; Boschmans, J.; Sobott, F.; Scrivens, J. H.; Bleiholder, C.; Bowers, M. T.; Gewinner, S.; Schöllkopf, W.; Pagel, K.; von Helden, G. Protomers of Benzocaine: Solvent and Permittivity Dependence. *J. Am. Chem. Soc.* **2015**, *137* (12), 4236–4242. <https://doi.org/10.1021/jacs.5b01338>.
- (10) Patrick, A. L.; Cismesia, A. P.; Tesler, L. F.; Polfer, N. C. Effects of ESI Conditions on Kinetic Trapping of the Solution-Phase Protonation Isomer of p -Aminobenzoic Acid in the Gas Phase. *Int. J. Mass Spectrom.* **2017**, *418*, 148–155. <https://doi.org/10.1016/j.ijms.2016.09.022>.
- (11) Sheng, H.; Tang, W.; Yerabolu, R.; Max, J.; Kotha, R. R.; Riedeman, J. S.; Nash, J. J.; Zhang, M.; Kenttämäa, H. I. Identification of N -Oxide and Sulfoxide Functionalities in Protonated Drug Metabolites by Using Ion–Molecule Reactions Followed by Collisionally Activated Dissociation in a Linear Quadrupole Ion Trap Mass Spectrometer. *J. Org. Chem.* **2016**, *81* (2), 575–586. <https://doi.org/10.1021/acs.joc.5b02409>.
- (12) Cismesia, A. P.; Nicholls, G. R.; Polfer, N. C. Amine vs. Carboxylic Acid Protonation in Ortho-, Meta-, and Para-Aminobenzoic Acid: An IRMPD Spectroscopy Study. *J. Mol. Spectrosc.* **2017**, *332*, 79–85. <https://doi.org/10.1016/j.jms.2016.10.020>.

- (13) Campbell, J. L.; Yang, A. M.-C.; Melo, L. R.; Hopkins, W. S. Studying Gas-Phase Interconversion of Tautomers Using Differential Mobility Spectrometry. *J. Am. Soc. Mass Spectrom.* **2016**, *27* (7), 1277–1284. <https://doi.org/10.1007/s13361-016-1392-2>.
- (14) Schmidt, J.; Meyer, M. M.; Spector, I.; Kass, S. R. Infrared Multiphoton Dissociation Spectroscopy Study of Protonated *p*-Aminobenzoic Acid: Does Electrospray Ionization Afford the Amino- or Carboxy-Protonated Ion? *J. Phys. Chem. A* **2011**, *115* (26), 7625–7632. <https://doi.org/10.1021/jp203829z>.
- (15) Xia, H.; Attygalle, A. B. Transformation of the Gas-Phase Favored *O*-Protomer of *p*-Aminobenzoic Acid to Its Unfavored *N*-Protomer by Ion Activation in the Presence of Water Vapor: An Ion-Mobility Mass Spectrometry Study. *J. Mass Spectrom.* **2018**, *53* (4), 353–360. <https://doi.org/10.1002/jms.4066>.
- (16) Campbell, J. L.; Le Blanc, J. C. Y.; Schneider, B. B. Probing Electrospray Ionization Dynamics Using Differential Mobility Spectrometry: The Curious Case of 4-Aminobenzoic Acid. *Anal. Chem.* **2012**, *84* (18), 7857–7864. <https://doi.org/10.1021/ac301529w>.
- (17) Seo, J.; Warnke, S.; Gewinner, S.; Schöllkopf, W.; T. Bowers, M.; Pagel, K.; Helden, G. von. The Impact of Environment and Resonance Effects on the Site of Protonation of Aminobenzoic Acid Derivatives. *Phys. Chem. Chem. Phys.* **2016**, *18* (36), 25474–25482. <https://doi.org/10.1039/C6CP04941A>.
- (18) Gross, J. H. Chemical Ionization. In *Mass Spectrometry: A Textbook*; Gross, J. H., Ed.; Springer: Berlin, Heidelberg, 2011; pp 351–380. [https://doi.org/10.1007/978-3-642-10711-5\\_7](https://doi.org/10.1007/978-3-642-10711-5_7).
- (19) Rebane, R.; Kruve, A.; Liigand, P.; Liigand, J.; Herodes, K.; Leito, I. Establishing Atmospheric Pressure Chemical Ionization Efficiency Scale. *Anal. Chem.* **2016**, *88* (7), 3435–3439. <https://doi.org/10.1021/acs.analchem.5b04852>.
- (20) Chai, Y.; Hu, N.; Pan, Y. Kinetic and Thermodynamic Control of Protonation in Atmospheric Pressure Chemical Ionization. *J. Am. Soc. Mass Spectrom.* **2013**, *24* (7), 1097–1101. <https://doi.org/10.1007/s13361-013-0626-9>.
- (21) Kumar, R.; Yerabolu, R.; Kenttämä, H. I. Effects of Residual Water in a Linear Quadrupole Ion Trap on the Protonation Sites of 4-Aminobenzoic Acid. *J Am Soc Mass Spectrom* **2020**, *8*.
- (22) Yerabolu, R.; Kong, J.; Easton, M.; Kotha, R. R.; Max, J.; Sheng, H.; Zhang, M.; Gu, C.; Kenttämä, H. I. Identification of Protonated Sulfone and Aromatic Carboxylic Acid Functionalities in Organic Molecules by Using Ion–Molecule Reactions Followed by Collisionally Activated Dissociation in a Linear Quadrupole Ion Trap Mass Spectrometer. *Anal. Chem.* **2017**, *89* (14), 7398–7405. <https://doi.org/10.1021/acs.analchem.7b00817>.
- (23) Gronert, S. Quadrupole Ion Trap Studies of Fundamental Organic Reactions. *Mass Spectrom. Rev.* **2005**, *24* (1), 100–120. <https://doi.org/10.1002/mas.20008>.

- (24) Gronert, S. Estimation of Effective Ion Temperatures in a Quadrupole Ion Trap. *J. Am. Soc. Mass Spectrom.* **1998**, *9* (8), 845–848. [https://doi.org/10.1016/S1044-0305\(98\)00055-5](https://doi.org/10.1016/S1044-0305(98)00055-5).
- (25) Habicht, S. C.; Vinueza, N. R.; Amundson, L. M.; Kenttämää, H. I. Comparison of Functional Group Selective Ion–Molecule Reactions of Trimethyl Borate in Different Ion Trap Mass Spectrometers. *J. Am. Soc. Mass Spectrom.* **2011**, *22* (3), 520–530. <https://doi.org/10.1007/s13361-010-0050-3>.
- (26) Cooks, R. G.; Kruger, T. L. Intrinsic Basicity Determination Using Metastable Ions. *J. Am. Chem. Soc.* *99* (4), 1279–1281.
- (27) Nourse, B. D.; Graham Cooks, R. Proton Affinity Determinations Using the Kinetic Method in an Ion Trap Mass Spectrometer. *Int. J. Mass Spectrom. Ion Process.* **1991**, *106*, 249–272. [https://doi.org/10.1016/0168-1176\(91\)85022-E](https://doi.org/10.1016/0168-1176(91)85022-E).

## CHAPTER 5. MEASUREMENT OF THE PROTON AFFINITIES OF A SERIES OF MONO- AND BIRADICALS OF PYRIDINE

### 5.1 Introduction

In the recent years aromatic carbon-centered  $\sigma$ -type mono- and biradicals (such as benzyne) have received increased attention because they serve as reaction intermediates in many areas, including the function of some DNA-cleavers such as calicheamicin and dynemicin.<sup>1-3</sup> These drug molecules contain enediyne functional groups that can undergo Bergman cyclization to generate highly reactive biradicals (*para*-benzyne) in biological systems. These biradicals once formed can abstract hydrogen atom from each strand of double-stranded DNA, ultimately leading to apoptosis of cells.<sup>1</sup> Hence a better understanding of the properties of these types of reaction intermediates (biradicals) is necessary that could facilitate the design of better synthetic prodrugs that generate desirable, biologically-active biradical intermediates.

Protonated mono-and biradicals are substantially more reactive than the corresponding neutral molecules both in solution and in the gas phase.<sup>4</sup> Hence knowledge on the proton affinities (PA) of basic mono-and biradicals is crucial for understanding their reactivities. The proton affinity (PA) of a neutral molecule is defined as the negative of the enthalpy change for the gas-phase reaction between a proton and the neutral molecule to produce the (charged) conjugate acid of the molecule.<sup>5</sup> Gas-phase PA values are interesting because complications due to solvation effects are absent in the gas phase.<sup>4</sup> However, only very few experimental gas-phase PA values have been recorded for monoradicals,<sup>6-9</sup> and none for monoradicals of the type considered here. Gas-phase PA of one related biradical, 2, 6-didehydropyridine has been previously determined.<sup>10</sup>

Various mass spectrometric techniques are commonly used for experimental determination of gas-phase PA values. Many mass spectrometric methods have been developed for this purpose such as the equilibrium method<sup>11</sup> and the Cooks' kinetic methods.<sup>12</sup> In case of equilibrium method, an equilibrium between the protonated analyte and a reference base needs to be established, which is impossible in the case of highly reactive radical species. On the other hand, the Cooks' kinetic method requires formation of a proton-bound dimer between the protonated analyte and a reference base. Unfortunately, this method cannot be used for radical species as they are highly reactive and may react in undesirable ways with the references bases. PA values can be also determined by another method known as the bracketing method.<sup>11,13,14</sup> The bracketing technique utilizes proton

transfer reactions of the protonated analytes with different reference bases with known PAs. The occurrence of, or absence of, (exothermic) proton transfer is monitored as a function of the PA of the reference base to determine the upper and lower limits for the PA of the analyte. This bracketing method is suitable for determination of PA values of (bi)radicals and hence this method was employed here to measure the PA values for a series of pyridine-based mono- and biradicals. The experimentally determined PA values have also been compared to those obtained by quantum chemical calculations.

## **5.2 Experimental**

### **5.2.1 Chemicals**

The radical precursors, 2-iodopyridine, 3-iodopyridine, 4-iodopyridine, 2, 3-diiodopyridine, 2,4-diiodopyridine, 3, 5-diiodopyridine and 3, 4-pyridinedicarboxylic anhydride, were purchased from Sigma-Aldrich (purities  $\geq 97\%$ ) while 2, 6-Diiodopyridine was purchased from Accel Pharmtech (purity  $\geq 97\%$ ). LC-MS grade methanol and water were purchased from Thermo Fisher Scientific and all the chemicals were used without further purification. Nitrogen gas used for atmospheric pressure chemical ionization (APCI) was derived from boil off of liquified nitrogen (purity: 99.998 %) purchased from Linde.

### **5.2.2 Sample Preparation**

Solutions containing the radical precursors were prepared at a concentration of 0.5 mM in 1-1 (v/v) methanol-water.

### **5.2.3 Instrumentation**

#### **5.2.3.1 Ion-Molecule Reactions in Linear Quadrupole Ion Trap**

Some of the experiments have been performed using a linear quadrupole ion trap equipped with an atmospheric pressure chemical ionization (APCI) source. Solutions containing monoradical and biradical precursors were injected into the APCI source by using 500  $\mu\text{L}$  Hamilton syringe maintained at a flowrate of 10  $\mu\text{L}/\text{min}$ . The APCI source was operated at the following conditions: vaporizer temperature of 300  $^{\circ}\text{C}$ . capillary temperature of 250 $^{\circ}\text{C}$ , sheath gas

(N<sub>2</sub>) flow rate of 30 (arbitrary units), auxiliary gas (N<sub>2</sub>) flow rate of 10 (arbitrary units), and capillary voltage of 5 kV. Protonated (bi)radical precursors were guided by the ion transfer optics into the linear quadrupole ion trap. The ion optics were optimized in order to ensure maximum signal intensity of the ions. The protonated radical precursors were then isolated using an isolation width of 2 m/z units and a q value of 0.25. The precursors were then subjected to collision activated dissociation (CAD) using a collision energy of 30-50 (arbitrary units) and helium as the collision gas. The biradical precursors needed two CAD events (MS<sup>3</sup>) while the monoradical precursors needed only one CAD event (MS<sup>2</sup>). The Bi- and monoradicals generated after CAD were isolated and allowed to react with reagent bases introduced into the ion trap.

An external home-built manifold (described elsewhere)<sup>15-17</sup> was used to introduce the reference bases into the ion trap. The manifold was maintained at a temperature of 160 °C to ensure evaporation of the reference bases. The bases were diluted with helium, introduced in the inlet manifold at a flow rate of 0.6 L/h using a Granville-Phillips leak valve. In order to examine the exo-/endothermicity of any observed proton transfer reactions, protonated mono- and biradicals were allowed to react with the reference bases for varying periods of time. When the relative abundances of the reactant ions were < 3 % compared to the most abundant ion in the mass spectrum, abundances of all the ions were measured. At this reaction time, the ratio of the abundance of the protonated base (and the dimer of the protonated base if observed) to the sum of the abundances of all the product ions was determined. This ratio was used to classify the reaction as exothermic or endothermic.

### **5.2.3.2 Ion-Molecule Reactions in Fourier Transform Ion Cyclotron Resonance (FT-ICR) Mass Spectrometer**

Some experiments on the biradicals were also performed using a Finnigan model FTMS 2001 FT-ICR by previous group members. The instrument was equipped a differentially pumped dual cell placed within the magnetic field produced by a 3.0 T superconducting magnet. The two cells were separated by a common plate with a 2-mm hole in the center. Usually this plate and other two trapping plates were kept at +2 V unless otherwise stated. Two Edwards (Sanborn, NY, USA) diffusion pumps (800 L/s) maintained the nominal base pressure in each cell at  $< 1 \times 10^{-9}$  Torr. The diffusion pumps were backed with an Alcatel mechanical pump.

In FT-ICR, protonation of the precursors were carried out via methanol chemical ionization described elsewhere.<sup>18</sup> The conductance limit plate was then grounded for transferring the precursor ions into the other cell. Usually the transfer time varied between 100- 160  $\mu$ s depending upon the  $m/z$  of the ions. In the second cell, the precursor ions were subjected to sustained off-resonance irradiation collision-activated dissociation (SORI-CAD)<sup>19</sup> to generate protonated mono- and biradicals. Prior to isolation of the protonated biradical, either one or five second cooling times was used to reduce the extra energy of the biradicals via IR emission and collisions with Ar gas, pulsed into the cell using a set of two pulsed valves. Isolation of the biradicals were carried out using stored-waveform inversed Fourier transform (SWIT) by ejecting all unwanted ions from the cell. The isolated ions were then allowed to react with reference bases introduced into the trap using a Granville-Phillips leak valve.

### 5.3 Computational Methods

All the calculations for this project were performed by Dr. Nash. Optimization of molecular geometries for all the neutral and protonated species were optimized at the density functional (DFT) level of theory by using the correlation-consistent polarized valence-triple- $\zeta$  (cc-pVTZ) basis set.<sup>20</sup> An isodesmic reaction involving proton transfer from the charged aromatic (bi)radical to pyridine to produce pyridinium cation and the neutral (bi)radical was used to calculate the proton affinities (PA) for the mono- and biradicals. In order to derive PAs for the (bi)radicals the calculated enthalpy change for the isodesmic reaction was then added to the experimentally determined PA for pyridine (222 kcal mol<sup>-1</sup>).<sup>5</sup> The performance of the following levels of theory were compared by calculating the PAs for the mono- and the biradicals: (1) (U)B3LYP/cc-pVTZ//(U)B3LYP//cc-pVTZ, (2) RHF-(U)CCSD(T)/(U)B3LYP/cc-pVTZ, (3) RHF-(U)CCSD(T)/cc-pVTZ//RHF-(U)CCSD(T)/cc-pVTZ, and (4) CASPT2/CASSCF( $m,n$ )/cc-pVTZ//RHF-(U)CCSD(T)/cc-pVTZ. All the calculated PAs were corrected for zero-point vibrational energy differences at 298 K by using the (U)B3LYP frequencies.

### 5.4 Results and Discussion

In traditional PA bracketing experiments, exothermic or endothermic proton transfers are usually distinguished based on whether they occur or not.<sup>21</sup> If only exothermic proton transfer

reactions are assumed to occur, observation of proton transfer from a protonate analyte to a reference base indicates that the PA of the reference base is greater than that of the analyte. However, reactions that are slightly endothermic may still occur, although slowly.<sup>13,22</sup> For determination of the most endothermic proton transfer reactions that can be observed in a linear quadrupole ion trap (LQIT) and a Fourier -transform ion cyclotron resonance mass spectrometer (FT-ICR), a series of protonated reference bases were allowed to react with neutral reference bases, both with known PA values. Next procedures were developed for the differentiating between exo- and endothermic proton transfer reactions in these instruments, based on the previous results. Using the same procedure, PA values for the mono- and biradicals were experimentally determined.

#### 5.4.1 Proton Affinity Measurements for Reference Bases.

In both the LQIT and FT-ICR, protonated reference bases (**1**) were allowed to react with neutral reference bases (**2**), both with known PAs.<sup>5,23</sup> The experimental results from LQIT are discussed first. As expected, exothermic proton transfer reactions were observed to occur much faster than the endothermic proton transfer reactions (**Figures 5.1** and **5.2** respectively). Experimental data for several endothermic reactions are shown in **Table 5.1** and all the data for proton transfer reactions between reference bases are shown in **Table 5.2**. As shown in **Table 5.1**, a proton transfer reaction that is endothermic by 2.5 kcal mol<sup>-1</sup> was observed to take place from protonated N-ethylacetamide to N, N-dimethylformamide whereas no proton transfer reaction was observed from protonated mesitylene to cyclopentanone (a reaction that is endothermic by 3.0 kcal mol<sup>-1</sup>). These results suggest that in the LQIT any proton transfer reaction that can be observed must have an enthalpy change less than 3.9 kcal mol<sup>-1</sup>.

Mass spectra for gas-phase ion-molecule reactions were recorded at various reaction times. When the relative abundance of the reactant ions was < 3% compared to the most abundant ion in the mass spectrum, a ratio of the abundance of the protonated reference base **2** ( and the abundance of the protonated dimer of the reference base **2**, if present) to the sum of the abundances of all ions present was calculated (**Tables 5.1** and **5.2**). For endothermic proton transfer reactions, the ratio was observed to be much smaller (< 0.4) while for exothermic proton transfer reactions, the ratios were calculated to be > 0.6. The proton transfer reactions whose ratios lie in between 0.4 and 0.6

were nearly thermoneutral. These results were subsequently used to determine whether the proton transfer reactions observed for mono- and biradicals in LQIT were exo- or endothermic.

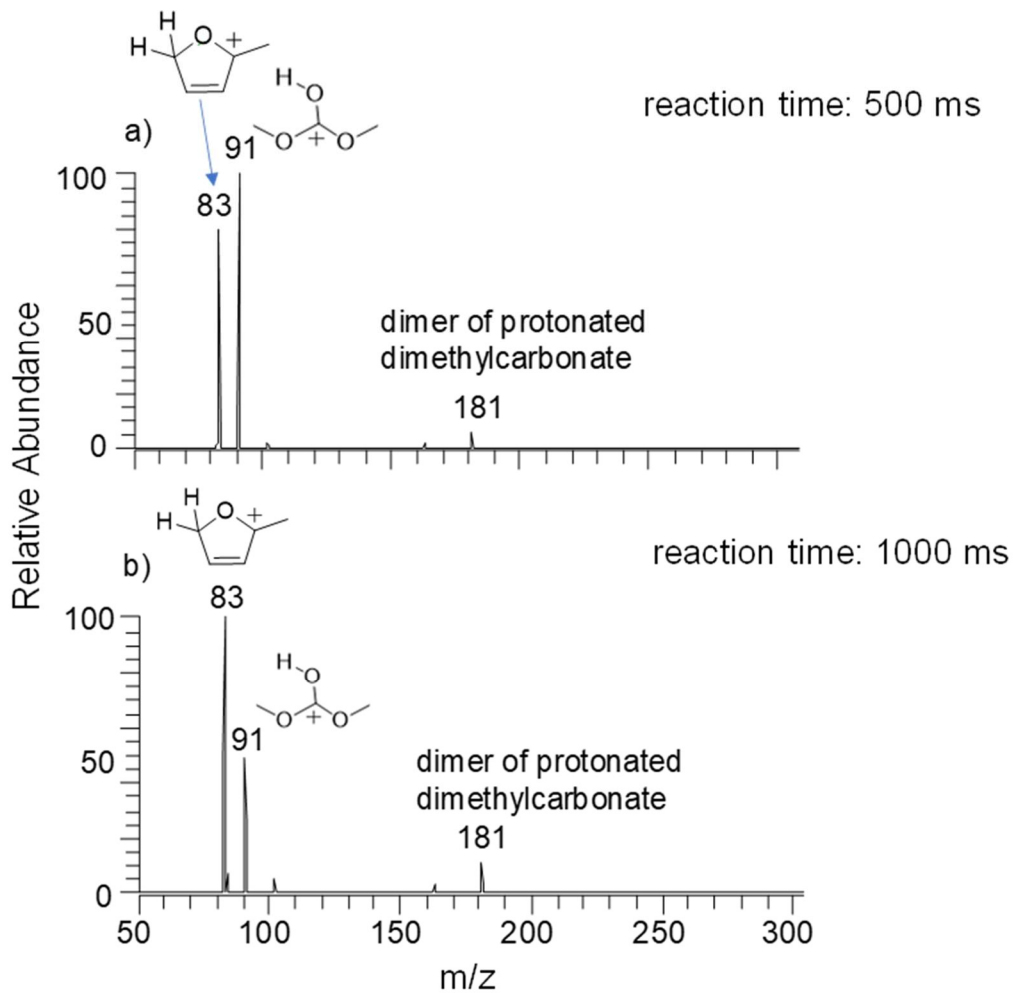


Figure 5.1 Mass spectra ( $MS^2$ ) recorded in the LQIT after (a) 500 ms and (b) 1000 ms exothermic proton transfer from protonated dimethylcarbonate to 2-methylfuran (introduced into the ion trap using manifold)

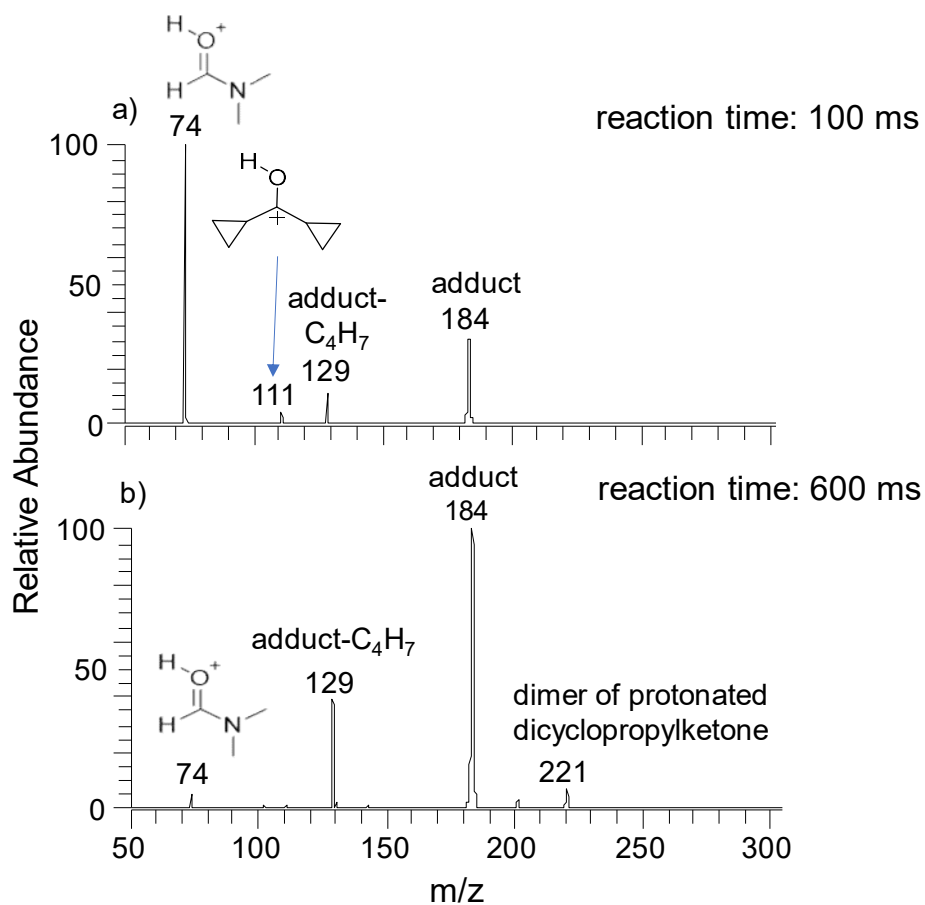


Figure 5.2 Mass spectra ( $MS^2$ ) recorded in the LQIT after (a) 100 ms and (b) 600 ms endothermic proton transfer from protonated N, N-dimethylformamide to dicyclopropylketone (introduced into the ion trap through the reagent mixing manifold)

Table 5.1 Structures of Reference Bases 1 and 2, Proton Affinities (PA) of the bases, a  $\Delta$ PA, and Proton Transfer Observations and Abundance Ratios Determined in a Linear Quadrupole Ion Trap Mass Spectrometer (LQIT)

protonated base 1 (PA)	base 2 (PA)	$\Delta$ PA <sup>b</sup> kcal mol <sup>-1</sup>	proton transfer observed?	abundance ratio <sup>c</sup>
 (212.1 kcal mol <sup>-1</sup> )	 (210.4 kcal mol <sup>-1</sup> )	1.7	yes	0.06
 (214.6 kcal mol <sup>-1</sup> )	 (212.1 kcal mol <sup>-1</sup> )	2.5	yes	0.28
 (214.8 kcal mol <sup>-1</sup> )	 (212.1 kcal mol <sup>-1</sup> )	2.7	yes	0.01
 (199.9 kcal mol <sup>-1</sup> )	 (196.9 kcal mol <sup>-1</sup> )	3.0	no	n/a <sup>d</sup>
 (215.3 kcal mol <sup>-1</sup> )	 (212.1 kcal mol <sup>-1</sup> )	3.2	no	n/a <sup>d12</sup>

<sup>1a</sup>Reference 5. <sup>b</sup>Difference in PA between reference bases 1 and 2.  $\Delta$ PA is the endothermicity of the proton transfer reaction. <sup>c</sup>Ratio of the abundance of protonated base 2 to the sum of the abundances of all ions after all protonated base 1 had reacted away (the relative abundance of protonated base 1 was < 3% compared to the most abundant ion in the spectrum; see text). <sup>d</sup>n/a = not applicable because no proton transfer reaction was observed.

Table 5.2 . Observation of Proton Transfer Reactions between Protonated Reference Bases 1 and Neutral Reference Bases 2 (introduced into the ion trap), Both with Known PA, in the LQIT. The Ratio of the Abundance of the Protonated Reference bases 2 to the Sum of the Abundances of All Ions After All the Protonated Base 1 Had Reacted Away.

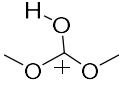
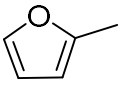
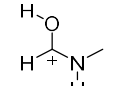
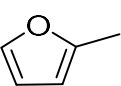
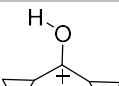
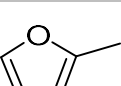
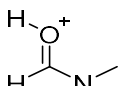
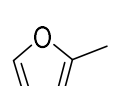
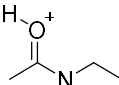
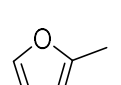
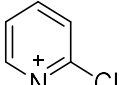
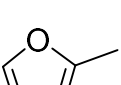
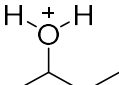
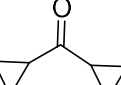
protonated base 1 (PA)	base 2 (PA)	$\Delta PA^b$ kcal mol <sup>-1</sup>	proton transfer observed?	abundance ratio <sup>c</sup>
		- 8.6	yes	0.70
198.4	207.0			
		- 3.5	yes	0.83
203.5	207.0			
		+ 3.4	yes	0.06
210.4	207.0			
		+ 5.1	no	<sup>b</sup> not applicable
212.1	207.0			
		+ 7.6	no	not applicable
214.6	207.0			
		+ 8.3	no	not applicable
215.3	207.0			
		-15.6	yes	0.82
194.8	210.4			

Table 3.2 continued

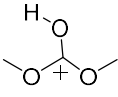
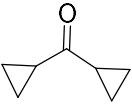
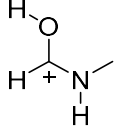
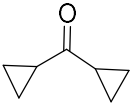
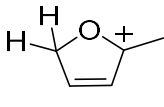
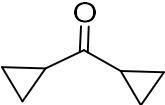
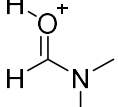
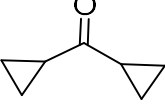
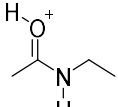
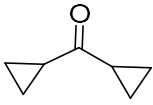
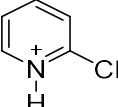
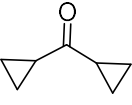
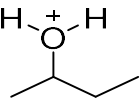
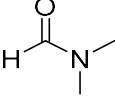
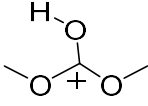
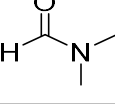
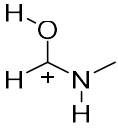
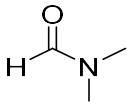
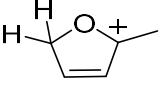
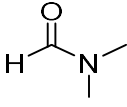
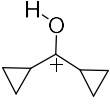
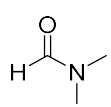
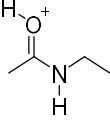
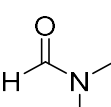
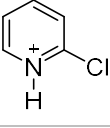
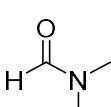
		<b>-12.0</b>	<b>yes</b>	<b>0.92</b>
198.4	210.4			
		-6.9	yes	0.82
203.5	210.4			
		-3.4	yes	-0.79
207.0	210.4			
		+ 1.7	yes	0.06
212.1	210.4			
		+ 4.2	no	not applicable
214.6	210.4			
		+ 4.9	no	not applicable
215.3	210.4			
		-17.9	yes	0.80
194.8	212.1			
		-13.7	yes	0.99
198.4	212.1			

Table 3.2 continued

		<b>-8.6</b>	<b>yes</b>	<b>0.98</b>
203.5	212.1			
		-5.1	yes	0.96
207.0	212.1			
		-1.7	yes (slow)	0.07
210.4	212.1			
		+2.5	yes	0.28
214.6	212.1			
		+3.2	no	not applicable
215.3	212.1			

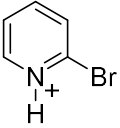
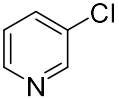
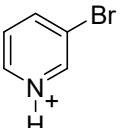
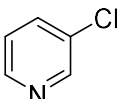
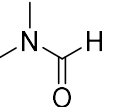
<sup>a</sup> PAs of reference bases are from reference 19 and have the uncertainty of  $\pm 1.9$  kcal mol<sup>-1</sup>. <sup>b</sup> No proton transfer reactions were observed.

In FT-ICR the precursor ions may acquire excess internal energy during SORI-CAD and ion isolation. For example, an endothermic ( $\Delta PA = 1.8$  kcal mol<sup>-1</sup>) proton transfer reaction was observed from 2-methoxypropene to N, N-dimethylformamide after a cooling time of 1 s. In attempt to distinguish between exo- and endothermic proton transfer reactions in the FT-ICR, the protonated bases **1** were subjected to two cooling times, 1s (normal) and 5 s, prior to isolation and ion-molecule reactions. A cooling time of 5 s is expected to cool down the ions considerably and hence the cooler ions should not undergo endothermic reactions. **Table 5.3** shows whether endothermic proton transfer reactions were observed or not after 5 s cooling time. Endothermic proton transfer reactions were observed when  $\Delta PA$  of the reference bases was 0.4 kcal mol<sup>-1</sup> and 1.6 kcal mol<sup>-1</sup> but no proton transfer reaction was observed when  $\Delta PA$  was 1.8 kcal mol<sup>-1</sup>. These

results suggest that when  $\Delta PA$  of the reference bases is  $1.8 \text{ kcal mol}^{-1}$  or greater, endothermic proton transfer reactions cannot be observed in FT-ICR.

The method described above for LQIT was used to determine the PAs of the mono- and biradicals whereas the method developed above for the FT-ICR was used to determine the PAs of some of the biradicals.

Table 5.3 Structures of Reference Bases 1 and 2, Proton Affinities (PA) of the reference bases,  $\Delta PAs$ , and Proton Transfer Observations Determined b in an FT-ICR Mass Spectrometer

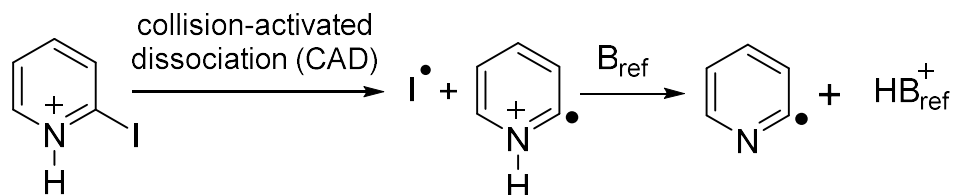
protonated base 1 (PA)	base 2 (PA)	$\Delta PA^c$ $\text{kcal mol}^{-1}$	proton transfer observed?
 (216.3 $\text{kcal mol}^{-1}$ )	 (215.9 $\text{kcal mol}^{-1}$ )	0.4	yes
 (217.5 $\text{kcal mol}^{-1}$ )	 (215.9 $\text{kcal mol}^{-1}$ )	1.6	yes (slow)
 (213.9 $\text{kcal mol}^{-1}$ )	 (212.1 $\text{kcal mol}^{-1}$ )	1.8	no

<sup>a</sup>Reference 5. <sup>b</sup>After a cooling time of 5 s. <sup>c</sup>Difference in PA between reference bases 1 and 2. Note that  $\Delta PA$  is the endothermicity of the proton transfer reaction.

#### 5.4.2 Proton Affinity Measurements for Monoradicals

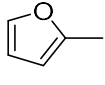
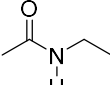
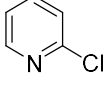
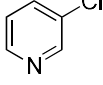
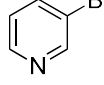
The precursors of the monoradicals (isomeric mono-iodopyridines) were introduced into LQIT where they were protonated, transferred into the ion trap, isolated and subjected to CAD to cleave off iodine atom to generate the monoradicals (e.g., **Scheme 5.1**). The monoradicals were isolated and allowed to react with neutral reference bases until the relative abundance of the radical was  $< 3\%$  compared to the most abundant ion in the mass spectra. At this time, the ratio of the abundance of the protonated base and protonated base dimer (if present) to the sum of the abundances of all of the product ions was determined. If the ratio was  $< 0.4$ , the reaction was

assigned to be endothermic whereas if the ratio was  $> 0.6$ , the reaction was designated to be exothermic. If the ratio was calculated to be between 0.4 and 0.6, it was designated to be a thermoneutral reaction. The final PA values were determined by taking an average of the PA of the reference base (if any) for which a thermoneutral reaction was observed and the value obtained by taking the average of the PA values of the reference bases undergoing the least endothermic reaction and the least exothermic reaction. The final values are shown in red in **Table 5.4**. The similarity of the final values to that of the reference bases supports the accuracy of the determined PA values. The error of the PA measurements can be calculated based on the uncertainties of the reported PAs of the reference bases. PAs of the reference bases used here has an uncertainty of  $\pm 1.9 \text{ kcal mol}^{-1}$  (NIST database).<sup>5</sup> To account for the accuracy of PA values determined here, the error for the experimental PA values is estimated to be  $\pm 2.5 \text{ kcal mol}^{-1}$ , which is close to the commonly accepted error range<sup>21,24,25</sup> for bracketing method.



Scheme 5.1 CAD of protonated 2-iodopyridine in an LQIT in order to generate protonated 2-dehydropyridine via homolytic cleavage of the C-I bond, followed by isolation of the protonated monoradical and proton transfer from the monoradical to a reference base ( $B_{\text{ref}}$ ).

Table 5.4. Reference Bases, Their Proton Affinities (PA) and Abundance Ratios <sup>b</sup> Determined in a LQIT. The Average of the PA Values of the Reference Bases Whose Ratios Are Given in Bold Was Averaged with the PA Value of the Reference Base Observed to Undergo a Nearly Thermoneutral Reaction ( $0.4 < \text{Ratio} < 0.6$ ; Underlined in Below Table) to Determine the Final PA (Given in Red) for Each Monoradical

reference base							
PA (kcal mol <sup>-1</sup> )	207.0	210.4	212.1	214.6	215.3	215.9	217.5
	0.04	0.07	<b>0.26</b>	<u>0.58</u> <b>214.3</b>		<b>0.69</b>	0.88
	no proton transfer		0.09	<b>0.25</b>		0.63 <b>215.3</b>	<b>0.64</b>
	no proton transfer	0.02	0.01	0.23	<b>0.25</b>	<u>0.55</u> <b>216.2</b>	<b>0.72</b>

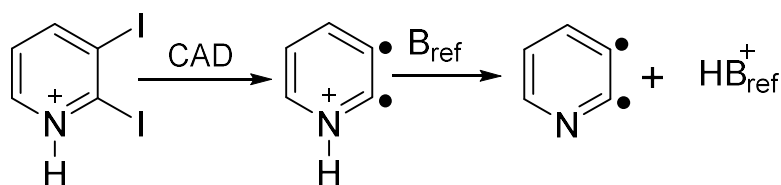
<sup>a</sup>Reference 5. <sup>b</sup>Ratio of the abundance of the protonated reference base (and protonated base dimer if present) to the sum of the abundances of all ions after all protonated radicals had reacted away. Values used to derive a PA for each monoradical are shown in bold.

The ratio determined for the proton transfer reaction protonated 2-dehydropyridine to 3-chloropyridine (PA = 215.9 kcal mol<sup>-1</sup>) was 0.61 while the ratio for proton transfer reaction from protonated 2-dehydropyridine to *N,N*-dimethylformamide (PA = 212.1 kcal mol<sup>-1</sup>) was determined to be 0.26. These results indicate that proton transfer reaction from protonated 2-dehydropyridine to 3-chloropyridine (PA = 215.9 kcal mol<sup>-1</sup>) is exothermic whereas the proton transfer reaction from 2-dehydropyridine to *N,N*-dimethylformamide (PA = 212.1 kcal mol<sup>-1</sup>) is endothermic and the PA of 2-dehydropyridine lies in between those of *N*-ethylacetamide and *N,N*-dimethylformamide (the average of these two values being 214.0 ± 2.5 kcal mol<sup>-1</sup>). Proton transfer reaction from protonated 2-dehydropyridine to *N*-ethylacetamide (PA = 214.6 kcal mol<sup>-1</sup>) was observed to be thermoneutral with ratio = 0.58. Hence the final value was determined to be 214.3 kcal mol<sup>-1</sup> by taking an average of value calculated above (214.0 ± 2.5 kcal mol<sup>-1</sup>) and the PA of the reference base *N*-ethylacetamide (PA = 214.6 kcal mol<sup>-1</sup>). Similarly protonated 3-dehydropyridine was observed to undergo exothermic proton transfer (ratio = 0.63) to 3-chloropyridine (PA = 215.9 kcal mol<sup>-1</sup>) and endothermic proton transfer to *N*-ethylacetamide (ratio = 0.25). Hence the PA for 3-dehydropyridine was determined to be 215.3 kcal mol<sup>-1</sup>. Similar

experimental results yielded a PA of  $216.2 \pm 2.5$  kcal mol<sup>-1</sup> for 4-dehydropyridine. It is noteworthy that the experimental PAs of all the monoradicals are lesser than that of pyridine (PA = 222 kcal mol<sup>-1</sup>). This reflects the presence of an electron-withdrawing site in monoradicals. Further, the PAs of the monoradicals also reflect the distance of the radical site from the basic nitrogen atom which agrees with calculated atomic charges. Calculations indicate that the nitrogen atom has the greatest negative charge for pyridine (0.628) followed by 4- (-0.570), 3- (-0.543) and 2-dehydropyridines (-0.417).

### 5.4.3 Proton Affinity Measurements for Biradicals

The PAs of isomeric biradicals were measured using both LQIT and FT-ICR. Experimental data obtained from LQIT are discussed first followed by data obtained from FT-ICR. In LQIT, protonated diiodoprecursors were initially isolated and subjected to two CAD steps in the ion trap to cleave two iodine atoms that generated protonated biradicals. The protonated biradicals were again isolated and allowed to react with reference bases with known PAs (**Scheme 5.2**) for variable reaction times until the relative abundance of the biradicals were < 3% compared to the most abundant ion in the mass spectrum. At this reaction time, the ratio of the abundances of the protonated reference bases (and protonated base dimers if present) to the sum of the abundances of all the product ions were determined in order to distinguish between exo- and endothermic proton transfer reactions. As explained in case of monoradicals, a reaction was assigned to be endothermic if the ratio was <0.4, exothermic if it was >0.6, and thermoneutral in between. The final PA values were determined by taking the average of the PAs of the reference bases undergoing the least endothermic reaction and the least exothermic reaction (**Table 5.5**).



Scheme 5.2 CAD of protonated 2,3-diiodopyridine in an LQIT in order to generate protonated 2,3-didehydropyridine via homolytic cleavages of the two C-I bonds, followed by isolation of the protonated biradical and proton transfer from the biradical to a reference base ( $B_{ref}$ )

**Figure 5.3** shows tandem mass spectra ( $MS^3$ ) recorded after reactions between protonated 2,6-didehydropyridine and *N*-ethylacetamide in the LQIT for 30 ms and 150 ms. As shown in **Figure 5.3**, the relative abundance of protonated *N*-ethylacetamide ( $m/z$  88) is high at short reaction times whereas the relative abundance of the protonated base dimer ( $m/z$  175) increases significantly at higher reaction times. Ion corresponding to  $m/z$  70 is a fragment of protonated *N*-ethylacetamide. Hence during determination of ratio of the protonated base, protonated base dimer and fragment ion of  $m/z$  70 are also considered. The ratio was calculated to be 0.88, indicating an exothermic proton transfer (**Table 5.5**). Reactions of protonated 2,6-didehydropyridine with other reference bases suggested that the PA of 2,6-didehydropyridine lies in between PAs of 2-butanol (PA= 194.8 kcal mol<sup>-1</sup>) and dimethylcarbonate (PA = 198.4 kcal mol<sup>-1</sup>) and a final PA of 196.6 ± 2.5 kcal mol<sup>-1</sup> was assigned to 2,6-didehydropyridine.

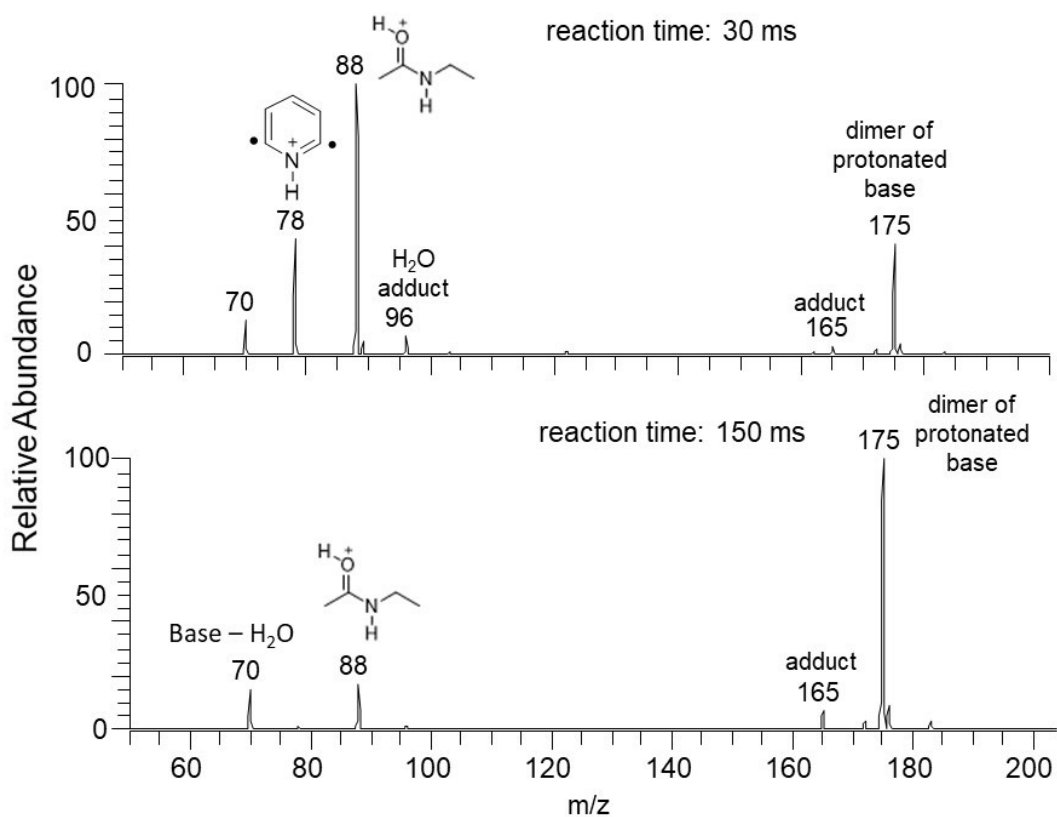


Figure 5.3 Mass spectra ( $MS^3$ ) recorded using the LQIT after (a) 30 ms and (b) 150 ms reaction of protonated 2,6-didehydropyridine with *N*-ethylacetamide. Proton transfer is exothermic.

Mass spectra measured after reactions of protonated 2,3-didehydropyridine with *N*-methylformamide for 5 ms and 10 ms are shown in **Figure 5.4**. As shown in **Figure 5.4** the abundance of protonated *N*-methylformaldehyde ( $m/z$  60) does not increase significantly with reaction time and the major reaction is formation of an adduct that has lost the formyl radical ( $m/z$  108). The ratio of the abundance of protonated *N*-methylformamide at the end of the reaction was 0.05, indicating that the proton transfer reaction is endothermic (**Table 5.5**). Similarly, reactions of protonated 2, 3-didehydropyridine with other reference bases indicated that the PA of 2, 3-didehydropyridine lies in between the PAs of *N*-methylformamide and 2-methylfuran (PA = 207.0 kcal mol<sup>-1</sup>) and a final PA of 205.3 kcal mol<sup>-1</sup> was assigned to 2, 3-didehydropyridine. The PAs of all other biradicals were determined similarly with two exceptions (**Table 5.5**).

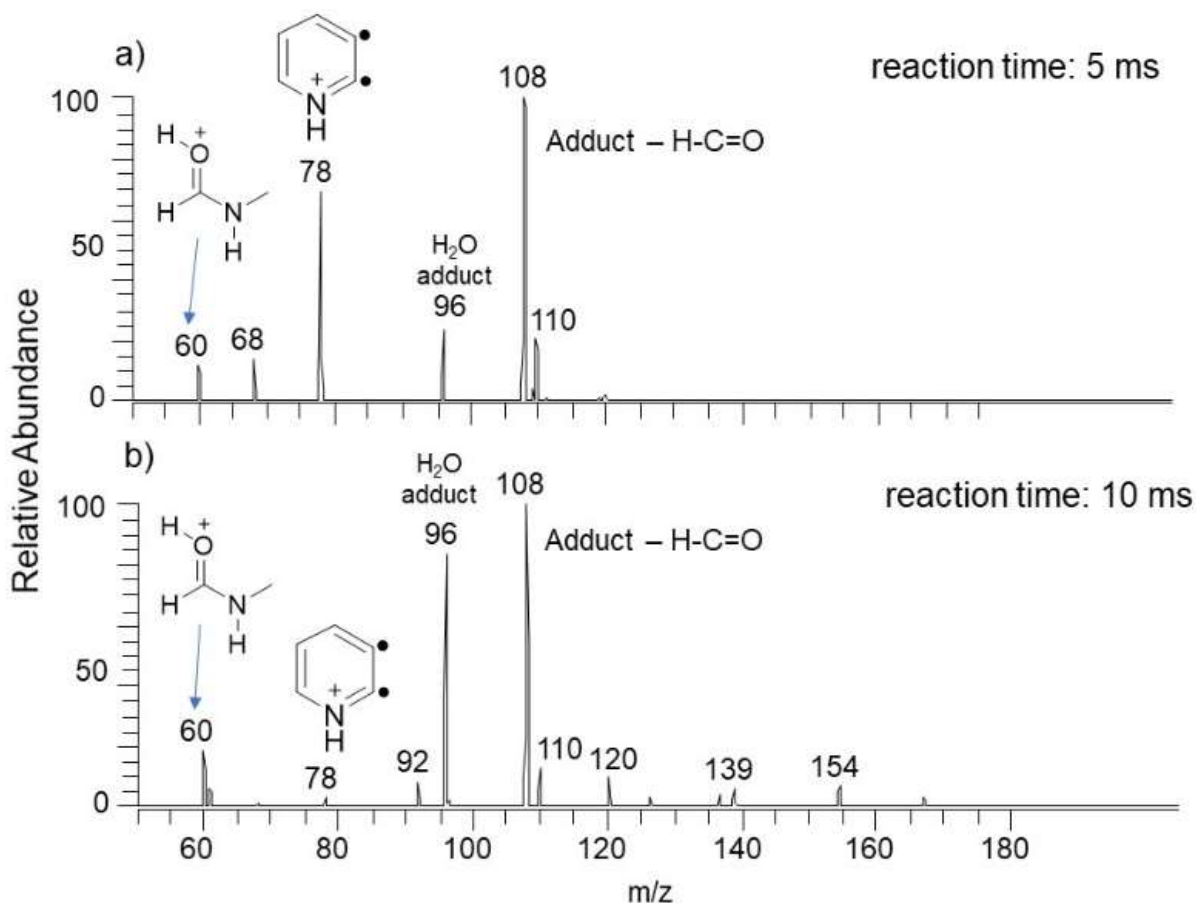
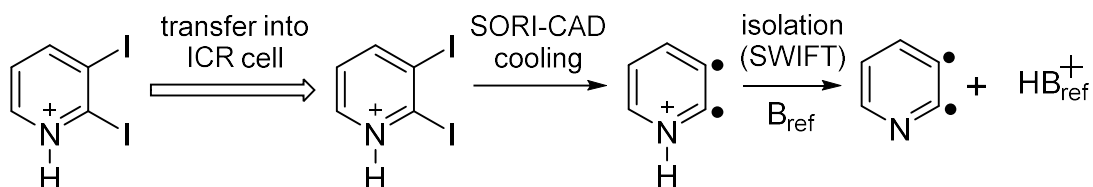


Figure 5.4 Mass spectra (MS<sup>3</sup>) recorded using the LQIT after (a) 5 ms and (b) 10 ms reaction of protonated 2,3-didehydropyridine with *N*-methylformamide. Proton transfer is endothermic

The PAs of the same biradicals were also determined in FT-ICR. The biradical precursors were introduced into FT-ICR cell, protonated using chemical ionization using methanol as reagent followed by sustained off-resonance irradiation collision-activated dissociation (SORI-CAD) to generate the radical sites (**Scheme 5.3**). The protonated biradicals were then cooled for 5 s using collisions with Ar, followed by isolation and ion-molecule reactions with various reference bases (**Table 5.3**). The results obtained are reported in **Table 5.5** and it is noteworthy that proton transfer reactions with endothermicity less than 1.8 kcal mol<sup>-1</sup> cannot be differentiated from exothermic reactions using this approach. The results obtained in FT-ICR are in agreement with those obtained in LQIT except one.



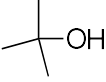
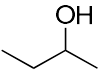
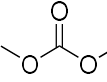
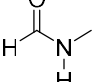
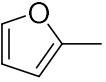
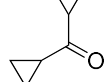
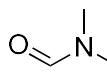
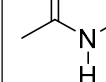
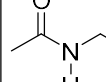
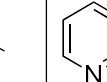
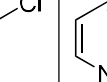
Scheme 5.3 Transfer of protonated 2,3-diiodopyridine from the first cell into the second cell of the FT-ICR, followed by SORI-CAD in order to generate the protonated 2,3-didehydropyridine biradical, cooling of the biradical for either 1 s or 5 s, isolation (using the SWIFT

The experimentally determined PA values for 2,3-didehydropyridine, 2,4-didehydropyridine, 2,6-didehydropyridine, 3,4-didehydropyridine and 3,5-didehydropyridine are  $205.3 \pm 2.5$  kcal mol<sup>-1</sup>,  $209.6 \pm 2.5$  kcal mol<sup>-1</sup>,  $196.6 \pm 2.5$  kcal mol<sup>-1</sup>,  $213.4 \pm 2.5$  kcal mol<sup>-1</sup> and  $214.0 \pm 2.5$  kcal mol<sup>-1</sup>, respectively (**Table 5.5**).

#### 5.4.4 Calculated Proton Affinities for Mono- and Biradicals

PAs of the radicals discussed above were calculated by Dr. Nash at several levels of theory and compared to those obtained experimentally. Geometries were optimized at both the (U)B3LYP/cc-pVTZ and RHF-(U)CCSD(T)/cc-pVTZ levels of theory while energies were computed at the (U)B3LYP/cc-pVTZ, RHF-(U)CCSD(T)/cc-pVTZ, and CASPT2/cc-pVTZ levels of theory. The PA values calculated at the (U)B3LYP//RHF-(U)CCSD(T) level of theory have the largest range of error ( $-5.0$  to  $+2.6$  kcal mol<sup>-1</sup>) compared to other levels of theory examined and PAs calculated by using (U)B3LYP//RHF-(U)CCSD(T) may only be reliable to 4–5 kcal mol<sup>-1</sup>. The performance of CASPT2 using RHF-(U)CCSD(T) optimized geometries appears to be about

Table 5.5. Structures of Reference Bases, Proton Affinities (PA) of the Bases,<sup>a</sup> Proton Transfer Observations When Using the Fourier-transform Ion Cyclotron Resonance Mass Spectrometer, <sup>b</sup> and the Linear Quadrupole Ion Trap Mass Spectrometer,<sup>c</sup> and the Final PA (in Bold Red)

reference base											
PA (kcal mol <sup>-1</sup> )	191.8	194.8	198.4	203.5	207.0	210.4	212.1	212.4	214.6	215.9	217.5
		(no proton transfer)	-(0.02)	-( <b>0.05</b> )	+( <b>0.65</b> ) <b>205.3</b>	(0.62)	+		(0.69)		
			(no proton transfer)	-(0.13)	-( <b>0.07</b> )		+ <sup>e</sup> <b>209.6</b>	(0.66)	+(0.61)		
	-(no proton transfer)	-(no proton transfer) <sup>f</sup>	+( <b>0.70</b> ) <b>196.6</b>	+(0.92)	(0.82)	+	(0.77)		(0.88)		
				-	-	(0.12)	-( <b>0.32</b> )		+( <b>0.75</b> ) <b>213.4</b>	+(0.67)	
				-	(no proton transfer)		-( <b>0.13</b> )		-(0.62) <b>214.0<sup>g</sup></b>	+( <b>0.60</b> )	+(0.65)

<sup>a</sup>Reference 5. Note that each of these values has an uncertainty of  $\pm 2.5$  kcal mol<sup>-1</sup>. <sup>b</sup>+ Indicates observation of an exothermic proton transfer in FT-ICR; - indicates not. <sup>c</sup>Abundance ratios in parenthesis if proton transfer was observed in LQIT. <sup>d</sup>The final PA is the average of the PA values of the reference bases whose ratios are given in bold, with two exceptions. <sup>e</sup>The PA of this base undergoing the least exothermic proton transfer reaction based on ICR results (+) was taken as the upper limit for the unknown PA. <sup>f</sup>This base showed no proton transfer reaction so no ratio could be determined. <sup>g</sup>See discussion on this assignment in the FT-ICR results section.

Table 5.6 Calculated<sup>a,b,c</sup> Proton Affinities (PA) for Mono- and Biradicals at Different Levels of Theory and Differences Between Calculated and Experimental Values ( $\Delta PA$ )

	(U)B3LYP// (U)B3LYP	$\Delta PA^d$	RHF-(U)CCSD(T)// (U)B3LYP	$\Delta PA^d$	RHF-(U)CCSD(T)// RHF-(U)CCSD(T)	$\Delta PA^d$	CASPT2// RHF-(U)CCSD(T)	$\Delta PA^d$	exp.
2-DP <sup>e</sup>	209.3	-5.0	210.2	-4.1	210.2	-4.1	211.1	-3.2	214.3 $\pm$ 2.5
3-DP	216.2	+0.9	216.5	+1.2	215.3	-0.0	217.2	+1.9	215.3 $\pm$ 2.5
4-DP	217.3	+1.1	217.7	+1.5	217.6	+1.4	218.1	+1.7	216.2 $\pm$ 2.5
2,3-DDP <sup>e</sup>	203.6 (198.3)	-1.7	206.8 (200.4)	+1.5	207.0 (200.3)	+1.7	207.7 (202.9)	+2.4	205.3 $\pm$ 2.5
2,4-DDP	211.7 (206.4)	+2.1	208.2 (207.4)	-1.4	207.4 (207.3)	-2.2	206.0 (208.3)	-3.6	209.6 $\pm$ 2.5
2,6-DDP	204.1 ( <b>195.9</b> )	-0.7	217.3 ( <b>196.9</b> )	0.3	208.0 ( <b>196.9</b> )	0.3	207.4 ( <b>198.4</b> )	+1.8	<b>196.6</b> $\pm$ 2.5
3,4-DDP	209.4 (212.0)	-4.0	209.8 (211.3)	-3.6	209.8 (211.2)	-3.6	212.1 (213.1)	-1.3	213.4 $\pm$ 2.5
3,5-DDP	216.6 (207.8)	+2.6	215.1 (207.8)	+1.1	214.3 (207.7)	+0.3	213.5 (211.5)	-0.5	214.0 $\pm$ 2.5
MUE <sup>f</sup>		2.3		1.8		1.7		2.1	
max. error		+2.6		+1.5		+1.7		+2.4	
min. error		-5.0		-4.1		-4.1		-3.6	
Range		7.6		5.6		5.8		6.0	

*a*All values in kcal mol<sup>-1</sup>; the cc-pVTZ basis set was used for all calculations. *b*Proton affinities were calculated by using an isodesmic equation involving proton transfer from the protonated (bi)radical to pyridine to produce the neutral (bi)radical and pyridinium cation. *c*PA values for the triplet states of the biradicals are given in parentheses. *d* $\Delta PA = PA_{calc} - PA_{exp}$ . *e*"DP": dehydroypyridine; "DDP": didehydroypyridine. *f*Mean Unsigned Error.

the same as that for the RHF-(U)CCSD(T)//(U)B3LYP and RHF-(U)CCSD(T)//RHF-(U)CCSD(T) levels of theory with the range of error being  $-3.6$  to  $+2.4$  kcal mol<sup>-1</sup> and this level of theory is expected to be reliable to ca. 3–4 kcal mol<sup>-1</sup>.

Among the biradicals, 2,6-didehydropyridine is particularly interesting because protonated 2,6-didehydropyridine is known<sup>10</sup> to undergo proton transfer from its lowest-energy excited triplet state, which is more acidic (by ca. 10 kcal mol<sup>-1</sup>; **Table 5.5**) than its (ground) singlet state. The experimentally determined PA value ( $196.6 \pm 2.5$  kcal mol<sup>-1</sup>) is in much better agreement with the calculated PA for the triplet state than that for the singlet state (CASPT2//RHF-(U)CCSD(T): 198.4 and 207.4 kcal mol<sup>-1</sup> for the triplet and singlet states, respectively; **Table 5.6**). Hence the present study is consistent with the previously published study.<sup>10</sup>

## 5.5 Conclusions

The proton affinities (PA) of several mono- and biradicals of pyridine were experimentally determined and compared to PA values derived after calculations at various levels of theory. Both LQIT and FT-ICR mass spectrometers were used for the experimental studies. A modified bracketing technique has been developed in both the instruments to distinguish between endo- and exothermic proton transfer reactions. The PAs of the monoradicals lie between 214–217 kcal mol<sup>-1</sup> while the PAs of the biradicals are lower (205–214 kcal mol<sup>-1</sup>). It is noteworthy that the PAs of all the mono- and biradicals are considerably lower than that of pyridine (222 kcal mol<sup>-1</sup>) which maybe because of the electron deficient nature of the radical site(s) and species containing more radical sites are expected to have a lower PA. Mono- and biradicals that had a radical site (s) farther from the basic pyridine nitrogen were observed to have greater PA. Among the monoradicals, 4-dehydropyridine was found to have the largest PA ( $216.2 \pm 2.5$  kcal mol<sup>-1</sup>) while 2-dehydropyridine was found to have the smallest PA ( $214.3 \pm 2.5$  kcal mol<sup>-1</sup>). The same applies to the biradicals except in case of 3,5-didehydropyridine. In overall the experimentally determined PA values are in good agreement with the calculated PA values. Among the levels of theory used for calculation of PAs, (U)B3LYP// (U)B3LYP is the least reliable (estimated error: 4–5 kcal mol<sup>-1</sup>) while the performance of the RHF-(U)CCSD(T)//(U)B3LYP, RHF-(U)CCSD(T) and CASPT2//RHF-(U)CCSD(T) levels of theory are slightly better.

## 5.6 References

- (1) Nicolaou, K. C.; Stabila, P.; Esmaeli-Azad, B.; Wrasidlo, W.; Hiatt, A. Cell-Specific Regulation of Apoptosis by Designed Enediynes. *Proc. Natl. Acad. Sci. U. S. A.* 1993, 90 (8), 3142–3146.
- (2) Smith, A. L.; Nicolaou, K. C. The Eneidyne Antibiotics. *J. Med. Chem.* 1996, 39 (11), 2103–2117. <https://doi.org/10.1021/jm9600398>.
- (3) Gredičak, M.; Jerić, I. Eneidyne Compounds - New Promises in Anticancer Therapy. *Acta Pharm.* 2007, 57 (2), 133–150. <https://doi.org/10.2478/v10007-007-0011-y>.
- (4) Widjaja, F.; Jin, Z.; Nash, J. J.; Kenttämaa, H. I. Comparison of the Reactivity of the Three Distonic Isomers of the Pyridine Radical Cation Toward Tetrahydrofuran in Solution and in the Gas Phase. *J. Am. Soc. Mass Spectrom.* 2013, 24 (4), 469–480. <https://doi.org/10.1007/s13361-012-0543-3>.
- (5) Informatics, N. O. of D. and. NIST Chemistry WebBook <https://webbook.nist.gov/chemistry/> (accessed Sep 15, 2019). <https://doi.org/10.18434/T4D303>.
- (6) DeFrees, D. J.; McIver, R. T.; Hehre, W. J. Heats of Formation of Gaseous Free Radicals via Ion Cyclotron Double Resonance Spectroscopy. *J. Am. Chem. Soc.* 1980, 102 (10), 3334–3338. <https://doi.org/10.1021/ja00530a005>.
- (7) Chowdhury, A. K.; Wilkins, C. L. Fourier Transform Mass Spectrometric Generation and Studies of Carboethoxycarbene Anion Radical (EtOCOCH.Cntdot.-). *J. Am. Chem. Soc.* 1989, 111 (9), 3150–3155. <https://doi.org/10.1021/ja00191a006>.
- (8) Fossey, J.; Mourgues, P.; Thissen, R.; Audier, H. E. Proton Affinity of Some Radicals of Alcohols, Ethers and Amines. *Int. J. Mass Spectrom.* 2003, 227 (3), 373–380. [https://doi.org/10.1016/S1387-3806\(03\)00084-8](https://doi.org/10.1016/S1387-3806(03)00084-8).
- (9) Chen, G.; Kasthurikrishnan, N.; Cooks, R. G. Proton Affinity of the Stable Free Radical 2,2,6,6-Tetramethyl-1-Piperidinyloxy Measured by the Kinetic Method. *Int. J. Mass Spectrom. Ion Process.* 1995, 151 (1), 69–75. [https://doi.org/10.1016/0168-1176\(95\)04308-4](https://doi.org/10.1016/0168-1176(95)04308-4).
- (10) Jankiewicz, B. J.; Vinueza, N. R.; Kirkpatrick, L. M.; Gallardo, V. A.; Li, G.; Nash, J. J.; Kenttämaa, H. I. Does the 2,6-Didehydropyridinium Cation Exist? *J. Phys. Org. Chem.* 2013, 26 (9), 707–714. <https://doi.org/10.1002/poc.3120>.
- (11) Meot-Ner (Mautner), M. The Proton Affinity Scale, and Effects of Ion Structure and Solvation. *Int. J. Mass Spectrom.* 2003, 227 (3), 525–554. [https://doi.org/10.1016/S1387-3806\(03\)00100-3](https://doi.org/10.1016/S1387-3806(03)00100-3).

- (12) Cooks, R. G.; Wong, P. S. H. Kinetic Method of Making Thermochemical Determinations: Advances and Applications. *Acc. Chem. Res.* 1998, 31 (7), 379–386. <https://doi.org/10.1021/ar960242x>.
- (13) Meot-Ner, M. Entropy-Driven Proton-Transfer Reactions. *J. Phys. Chem.* 1991, 95 (17), 6580–6585. <https://doi.org/10.1021/j100170a039>.
- (14) Wiseman, A.; Sims, L. A.; Snead, R.; Gronert, S.; Maclagan, R. G. A. R.; Meot-Ner Mautner, M. Protonation Energies of 1-5-Ring Polycyclic Aromatic Nitrogen Heterocyclics: Comparing Experiment and Theory. *J. Phys. Chem. A* 2015, 119 (1), 118–126. <https://doi.org/10.1021/jp506913r>.
- (15) Gronert, S. Estimation of Effective Ion Temperatures in a Quadrupole Ion Trap. *J. Am. Soc. Mass Spectrom.* 1998, 9 (8), 845–848. [https://doi.org/10.1016/S1044-0305\(98\)00055-5](https://doi.org/10.1016/S1044-0305(98)00055-5).
- (16) Gronert, S. Quadrupole Ion Trap Studies of Fundamental Organic Reactions. *Mass Spectrom. Rev.* 2005, 24 (1), 100–120. <https://doi.org/10.1002/mas.20008>.
- (17) Habicht, S. C.; Vinueza, N. R.; Amundson, L. M.; Kenttämä, H. I. Comparison of Functional Group Selective Ion–Molecule Reactions of Trimethyl Borate in Different Ion Trap Mass Spectrometers. *J. Am. Soc. Mass Spectrom.* 2011, 22 (3), 520–530. <https://doi.org/10.1007/s13361-010-0050-3>.
- (18) Price, J. M.; Kenttämä, H. I. Characterization of Two Chloro-Substituted m-Benzyne Isomers: Effect of Substitution on Reaction Efficiencies and Products. *J. Phys. Chem. A* 2003, 107 (42), 8985–8995. <https://doi.org/10.1021/jp035285r>.
- (19) Gauthier, J. W.; Trautman, T. R.; Jacobson, D. B. Sustained Off-Resonance Irradiation for Collision-Activated Dissociation Involving Fourier Transform Mass Spectrometry. Collision-Activated Dissociation Technique That Emulates Infrared Multiphoton Dissociation. *Anal. Chim. Acta* 1991, 246 (1), 211–225. [https://doi.org/10.1016/S0003-2670\(00\)80678-9](https://doi.org/10.1016/S0003-2670(00)80678-9).
- (20) Dunning, T. H. Gaussian Basis Sets for Use in Correlated Molecular Calculations. I. The Atoms Boron through Neon and Hydrogen. *J. Chem. Phys.* 1989, 90 (2), 1007–1023. <https://doi.org/10.1063/1.456153>.
- (21) Gorman, G. S.; Amster, I. J. Kinetic and Thermodynamic Considerations of the Bracketing Method: Entropy-Driven Proton-Transfer Reactions in a Fourier Transform Mass Spectrometer. *Org. Mass Spectrom.* 1993, 28 (12), 1602–1607. <https://doi.org/10.1002/oms.1210281236>.
- (22) Bouchoux, G.; Salpin, J. Y.; Leblanc, D. A Relationship between the Kinetics and Thermochemistry of Proton Transfer Reactions in the Gas Phase. *Int. J. Mass Spectrom. Ion Process.* 1996, 153 (1), 37–48. [https://doi.org/10.1016/0168-1176\(95\)04353-5](https://doi.org/10.1016/0168-1176(95)04353-5).

- (23) Gorman, G. S.; Speir, J. P.; Turner, C. A.; Amster, I. J. Proton Affinities of the 20 Common Alpha -Amino Acids. *J. Am. Chem. Soc.* 1992, 114 (10), 3986–3988. <https://doi.org/10.1021/ja00036a062>.
- (24) Bliznyuk, A. A.; Schaefer, H. F.; Amster, I. J. Proton Affinities of Lysine and Histidine: A Theoretical Consideration of the Discrepancy between Experimental Results from the Kinetic and Bracketing Methods. *J. Am. Chem. Soc.* 1993, 115 (12), 5149–5154. <https://doi.org/10.1021/ja00065a029>.
- (25) Wittrig, A. M.; Archibold, E. F.; Sheng, H.; Nash, J. J.; Kenttämää, H. I. Polar Effects Control the Gas-Phase Reactivity of Charged Para-Benzyne Analogs. *Int. J. Mass Spectrom.* 2015, 377, 39–43. <https://doi.org/10.1016/j.ijms.2014.04.017>.

## CHAPTER 6. COMPARISON OF SOLUTION AND GAS-PHASE REACTIONS OF 1,4-DIDEHYDROPHENAZINE BIRADICAL WITH VARIOUS NEUTRAL REAGENTS

### 6.1 Introduction

Certain drugs such as calicheamicin  $\gamma_1$ <sup>1</sup> and dynemicin A undergo nucleophile-induced Bergman cyclization to generate *para*-benzyne biradicals. The *para*-benzyne biradicals can irreversibly abstract hydrogen atoms from DNA strands, causing DNA degradation which may eventually lead to apoptosis of healthy cells.<sup>1,2</sup> This mechanism of action of the enediyne drugs has brought increased attention and interest to the Bergman cyclization reaction. The mechanism of enediyne drugs involving Bergman cyclization has been utilized for development of clinical drugs, but the drugs have been found to be too toxic for human use.<sup>3-9</sup> Hence, an improved understanding of *para*-benzynes is necessary for designing and development of synthetic anticancer drugs.

The Bergman cyclization of enediyne containing compounds has been known to be triggered by heat, protons or nucleophiles.<sup>10-12</sup> Heat-induced Bergman cyclization has been explored extensively both theoretically and experimentally.<sup>13-16</sup> Reaction conditions involving high temperature are not suitable for biological systems. However, inside target cancer cells photo-induced cyclization can be triggered at normal temperature and.<sup>17,18</sup> Although the first photo-induced Bergman cyclization was discovered by Campbell in 1968, photochemistry of enediynes was not investigated until 1990s.<sup>19</sup> Since 1994, substantial research has been carried out on the photochemistry of enediynes.<sup>20-23</sup>

The kinetics and mechanisms of enediyne cyclization have been investigated extensively in the past few decades and parameters such as the nature of substituents at the alkyne termini of the enediynes.<sup>24-29</sup> For example, photon irradiation of propyl substituted enediynes in isopropanol produced both Bergman cyclization products and photoreduction products of a triple bond of enediyne whereas the phenyl-substituted enediynes under similar conditions produced only Bergman cyclization products.<sup>12</sup> Triplet sensitization of enediynes with propyl substituents on the triple bonds using xanthenes as the triplet sensitizer yielded higher amount of photoreduction products compared to the Bergman cyclization products.<sup>12</sup> These results suggested that the Bergman cyclization reactions likely involved either excited singlet or triplet states.

Electronic repulsion between the in-plane  $\pi$ -orbitals of the alkyne groups was proposed to lower the activation enthalpy for Bergman cyclization of enediynes with electron withdrawing groups at the alkyne termini.<sup>30-32</sup> Computational studies showed that the electronic repulsion caused by substituent-induced structural perturbation resulted in the acceleration of Bergman cyclization in both cyclic and acyclic enediynes.<sup>33</sup>

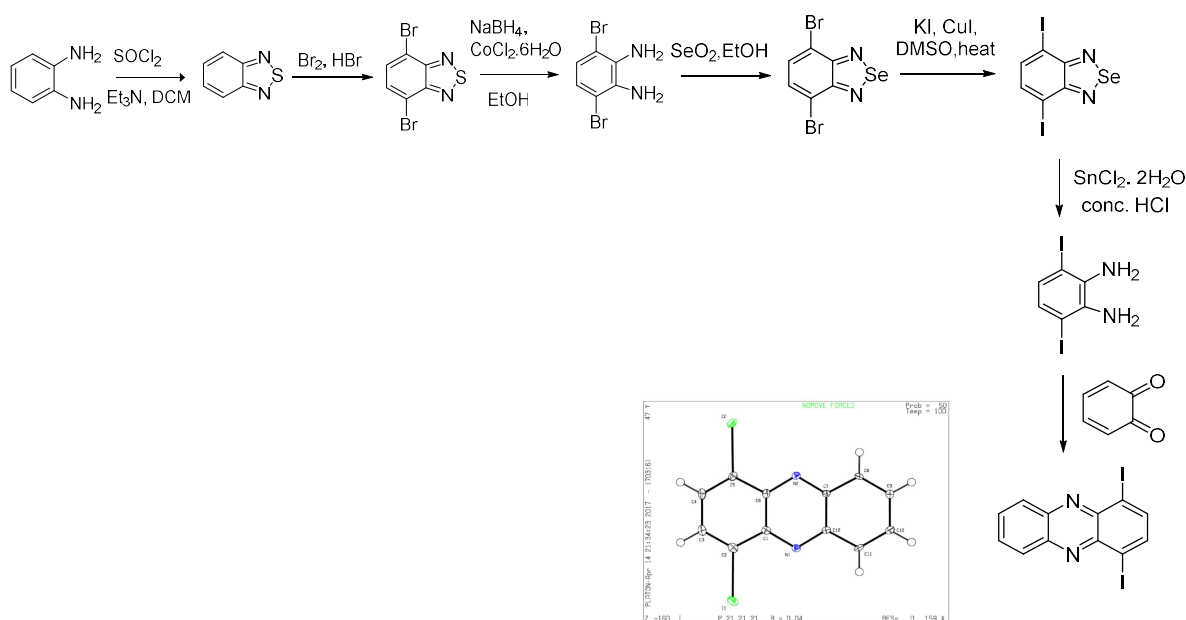
Previous studies also reported that the architecture of the enediyne also affects the activation energy of the Bergman cyclization. Experimental results suggested that the activation energy of Bergman cyclization is lower for conformationally rigid enediynes than for less rigid systems, leading to higher yield of cyclization products in rigid systems. For example, nine-membered enediynes were found to undergo photon-induced Bergman cyclization more efficiently than ten-membered cyclodeca-1,5-diyne-3-ene.<sup>34</sup> In the case of heteroarene-fused enediynes, electron deficient heteroenediynes, e.g., pyridine-fused enediynes, were found to have lower activation energy compared to the benzene-fused enediynes.<sup>16</sup> However, very few studies regarding photochemistry of heteroaromatic enediynes have been reported so far. In this study both heat-induced and photon-induced Bergman cyclization of 2,3-diethynylquinoxaline have been investigated in the presence of different reagents: allyl iodide (AI), dimethyldisulfide (DMDS) and tetrahydrofuran (THF). The products were ionized using atmospheric pressure chemical ionization (APCI) and characterized using tandem mass spectrometry, high resolution accurate mass analysis and gas-phase ion-molecule reactions. A comparison between gas-phase and solution reactivities of the generated *para*-benzyne (1,4-didehydrophenazine) has been explored in this study using the same reagents. The above reagents have been chosen because they have been extensively used for decades to investigate the reactivities of radical cations in the gas phase.<sup>35,36</sup>

## 6.2 Experimental

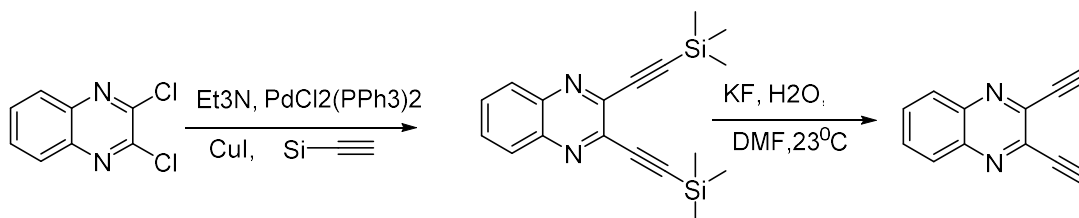
The *para*-benzyne analog (1,4-didehydrophenazine) was generated both in solution and gas-phase. 1,4-Didehydrophenazine was then allowed to react with neutral reagents such as allyl iodide (AI), dimethyldisulfide (DMDS) and tetrahydrofuran (THF). The details of such experiments are discussed sequentially.

## 6.2.1 Chemicals

1,4-Diiodophenazine was used as the precursor for the generation of 1,4-didehydrophenazine. 1,4-Diiodophenazine was synthesized from benzene-1,2-diamine using a previously published procedure<sup>37</sup> as shown in **Scheme 6.1**. All the chemicals were purchased from Sigma Aldrich and were used without further purification. The structure of the final product (1,4-didehydrophenazine) was verified by using X-ray crystallography and the corresponding data are shown in Scheme 6.1. A *para*-benzyne analog, protonated 1,4-didehydrophenazine, was generated from protonated 1,4-diiodophenazine in the gas phase in a linear quadrupole ion trap (LQIT) by using a procedure described in the experimental section (6.2.2).



Scheme 6.1 Scheme showing synthesis of 1,4-diiodophenazine along with the X-ray crystallographic data for the synthesized product



Scheme 6.2 Chemical synthesis of 2,3-diethynylquinoxaline from 2,3-dichloroquinoxaline

1,4-Didehydrophenazine was generated in solution by heat-induced and photon-induced Bergman cyclization of 2,3-diethynylquinoxaline. 2,3-Diethynylquinoxaline was synthesized from 2,3-dichloroquinoxaline by using a previously published synthetic procedure (**Scheme 6.2**).<sup>38</sup> The reagents allyl iodide (AI), dimethyldisulfide (DMDS) and tetrahydrofuran (THF) were all purchased from Sigma Aldrich and had purity of > 98 %. All the reagents were used without further purification. N<sub>2</sub> used for atmospheric pressure chemical ionization was purchased from Linde.

## 6.2.2 Experimental Section

Investigation of the gas-phase reactivity of *para*-benzyne analog was performed in a linear quadrupole ion trap (LQIT) equipped with an atmospheric pressure chemical ionization (APCI) source operating in positive ion mode. 1,4-Diiodophenazine was dissolved in 1-1 (v/v) methanol-water at a concentration of 0.01 mM and injected into APCI source. After ionization, protonated 1,4-diiodophenazine was transferred into the ion trap. Ions corresponding to protonated 1,4-diiodophenazine were isolated in the ion trap using an isolation width of 2 m/z units and a q value of 0.25. The isolated ions were then subjected to collision-activated dissociation (CAD) using a collision energy of 30 (arbitrary units) and helium as the collision gas. Upon CAD, protonated 1,4-diiodophenazine lost an iodine atom and generated a monoradical. The monoradical was again isolated and subjected to CAD, which led to the loss of the second iodine atom and generation of the desired biradical (protonated 1,4-didehydrophenazine). The biradical was again isolated and allowed to react for variable times with neutral reagents introduced into the trap by using an external manifold. The neutral reagents were introduced into the ion trap by using a home-built manifold described elsewhere.<sup>39-41</sup> The manifold was maintained at a temperature of 160 °C and the reagents were diluted with helium

A Rayonet reactor chamber (Model RPR-200, Southern New England Ultraviolet Co.) equipped with sixteen 253 nm wavelength UV lamps was used for photon-induced Bergman cyclization. Solutions containing 2,3-diethynylquinoxaline and allyl iodide (AI) or dimethyldisulfide (DMDS) or tetrahydrofuran (THF) were prepared and deoxygenated by purging with argon for 5 mins. The solutions were then transferred into quartz tubes and irradiated for variable times. “Dark control” experiments were also performed where an aliquot of the sample solution was placed into a vial, the vial was wrapped with aluminum foil and subjected to irradiation under the same experimental conditions as the reaction solutions. The photolysis

reaction chamber was maintained at 15 °C to ensure that the reaction products are produced by photolysis of the irradiated reaction mixture and not by thermal activation of the mixture. The reaction mixtures were analyzed using a linear quadrupole ion trap coupled with a high resolution orbitrap mass spectrometer (LTQ-Orbitrap XL). In some cases, gas-phase ion-molecule reactions were also used to identify the products formed by Bergman cyclization products.

Heat-induced Bergman cyclization of 2,3-diethynylquinoxaline was also investigated. Solutions of 2,3-diethynylquinoxaline in allyl iodide (AI) or tetrahydrofuran (THF) were prepared and purged with argon for 10 mins. Solutions of 2,3-diethynylquinoxaline in allyl iodide or in THF were heated to 60 °C. Both the reactions were carried out under inert atmosphere (in the presence of argon). Aliquots containing reaction mixture were withdrawn at intervals of one hour, ionized using positive mode APCI and analyzed using LTQ-orbitrap-XL. Following conditions were used upon APCI: vaporizer temperature 300 °C, capillary temperature 250 °C, capillary voltage 5 (arbitrary units), sheath gas (N<sub>2</sub>) 30-40 (arbitrary units), auxiliary gas (N<sub>2</sub>) 10-15 (arbitrary units), tube lens voltage 20 Volts

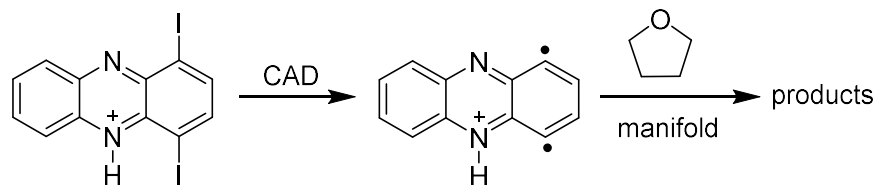
### 6.3 Results and Discussion

The *para*-benzyne analog 1,4-didehydrophenazine was generated in solution by photon-induced and heat-induced Bergman cyclization of 2,3-diethynylquinoxaline in the presence of tetrahydrofuran (THF) or dimethyldisulfide (DMDS) or allyl iodide (AI). The reaction products were analyzed using tandem mass spectrometry and high-resolution mass analysis. Protonated 1,4-didehydrophenazine was generated in the gas phase by collision-activated dissociation (CAD) of protonated 1,4-diiodophenazine and was allowed to react with the same reagents mentioned above. Reactivities of various reagents towards protonated 1,4-didehydrophenazine in the gas phase and towards 1,4-didehydrophenazine in solution are discussed below.

#### 6.3.1 Reactivity of *para*-Benzyne Toward Tetrahydrofuran in the Gas Phase and in Solution

Protonated 1,4-diiodophenazine was isolated in the ion trap and subjected to two CAD events to generate protonated 1,4-didehydrophenazine which was again isolated and allowed to react with THF for various times. Mass spectra recorded at 1 s and 5 s reaction times are shown in

**Figure 6.1.** As shown in **Figure 6.1**, THF addition is the major reaction and abstraction of 2 H atoms also occurs, albeit slowly. The efficiency for the reaction was measured to be 1.1 %.



Scheme 6.3 Generation of protonated 1,4-didehydrophenazine by CAD followed by ion-molecule reactions with tetrahydrofuran (introduced into the ion-trap by using a manifold)

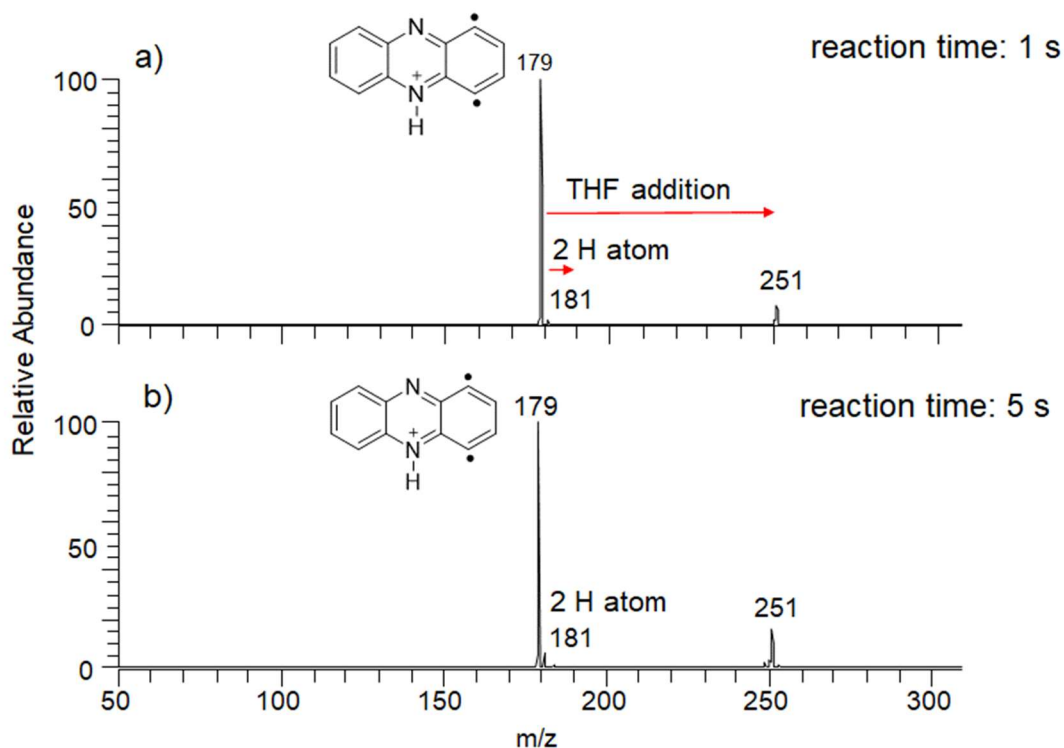
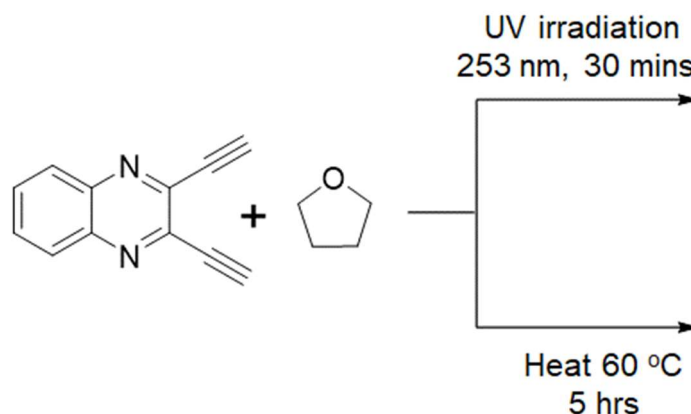


Figure 6.1 Mass spectra showing gas-phase ion-molecule reaction products when protonated 1,4-didehydrophenazine biradical was allowed to react with tetrahydrofuran (introduced through manifold) for a) 1 s and b) 5 s

The *para*-benzyne analog 1,4-didehydrophenazine was also generated in solution using photon-induced and heat-induced Bergman cyclization (**Scheme 6.4**). Photon-induced Bergman cyclization was carried out by irradiating a solution of 2,3-diethynylquinoxaline in tetrahydrofuran for 30 mins by UV light of wavelength 253 nm. The products were diluted using methanol and ionized using positive mode APCI before being analyzed by LQIT. A ‘dark control’ experiment was also performed under the same experimental conditions. A solution containing neat THF was

also irradiated under the same experimental conditions. Mass spectrum measured for the products generated in solution reactions by the products of photon-induced Bergman cyclization of 2,3-diethynylquinoxaline is shown in **Figure 6.2**.



Scheme 6.4 Generation of 1,4-didehydrophenazine by photon-induced and heat-induced Bergman cyclization of 2,3-diethynylquinoxaline

As shown in **Figure 6.2b**, 2,3-diethynylquinoxaline does not undergo any reactions under dark control experiments. In the presence of UV irradiation protonated 2,3-diethynylquinoxaline undergoes Bergman cyclization to generate 1,4-didehydrophenazine in solution. 1,4-Didehydrophenazine reacts with THF to generate products corresponding to THF-addition ( $m/z$  251) and 2 THF-addition ( $m/z$  323) (**Figure 6.2**).

Heat-induced Bergman cyclization of 2,3-diethynylquinoxaline was carried out by heating a solution of 2,3-diethynylquinoxaline dissolved in THF at 60 °C for 5 hours. The products were analyzed using APCI as the ionization source and the LTQ-orbitrap XL as mass analyzer. Mass spectra showing the solution reaction products at various reaction times are shown in **Figure 6.3**. THF addition is the major product, with the product corresponding to 2 THF-addition being the minor product. The reaction was almost complete after 5 hours. As shown in Figures 2 and 3, 2,3-diethynylquinoxaline underwent photon-induced and heat-induced Bergman cyclization to generate 1,4-didehydrophenazine which reacted with THF in solution to generate a product corresponding to THF addition. This indicated that both photon-induced and heat-induced Bergman cyclization yielded the same biradical species. It is noteworthy that protonated 1,4-didehydrophenazine biradical reacts with THF in the gas phase to generate the same product ion

corresponding to THF addition (**Figure 6.1**). This finding suggests that the reactivity of protonated 1,4-didehydrophenazine in the gas phase is similar to the reactivity of neutral 1,4-didehydrophenazine in solution.

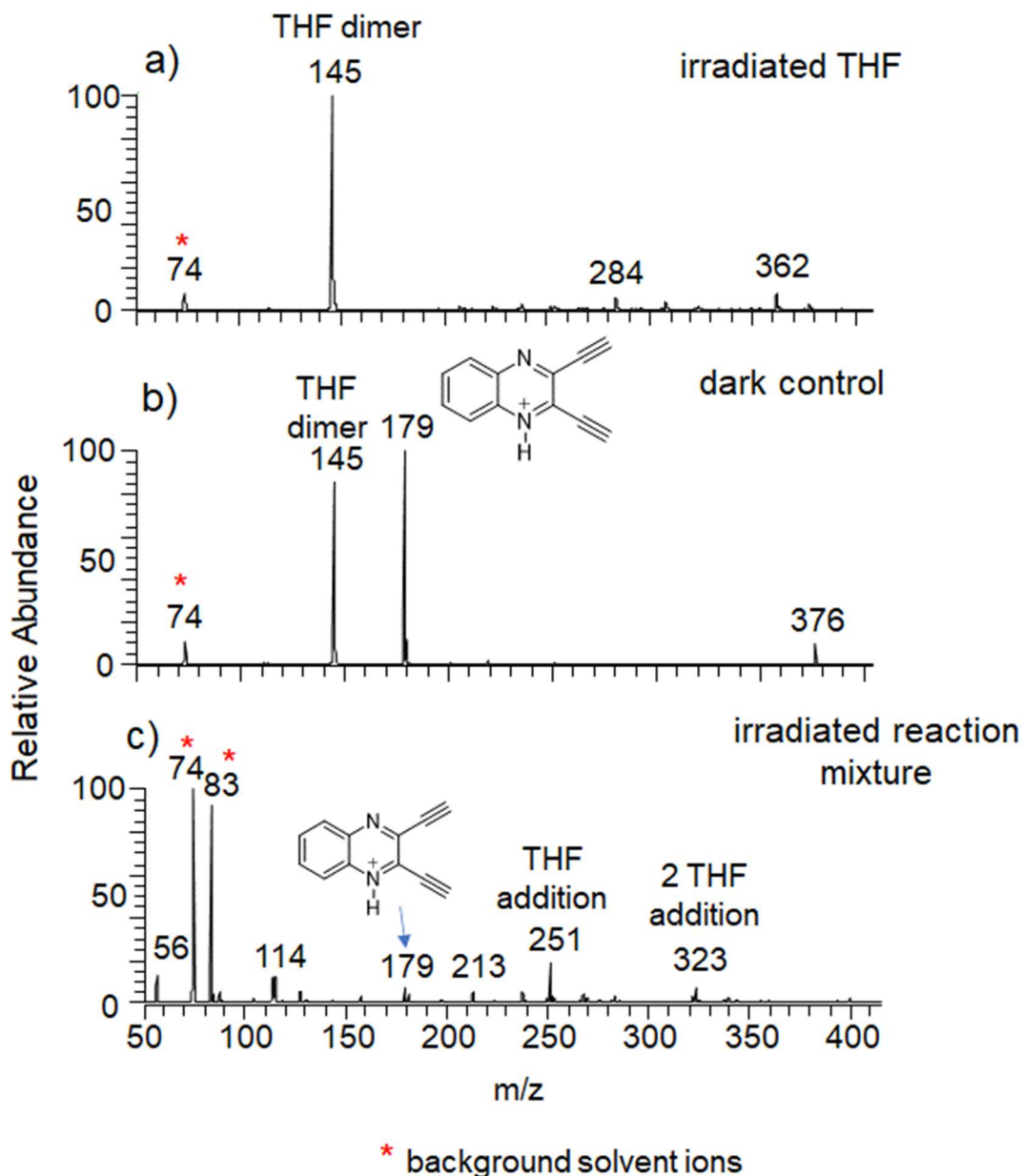


Figure 6.2 Figure showing mass spectra measured a) for ionized photolysis products when THF was irradiated for 30 mins, b) in dark control experiments and c) when 2,3-diethynylquinoxaline was subjected to photon-induced Bergman cyclization induced using an UV irradiation of 253 nm for 30 mins in the presence of THF

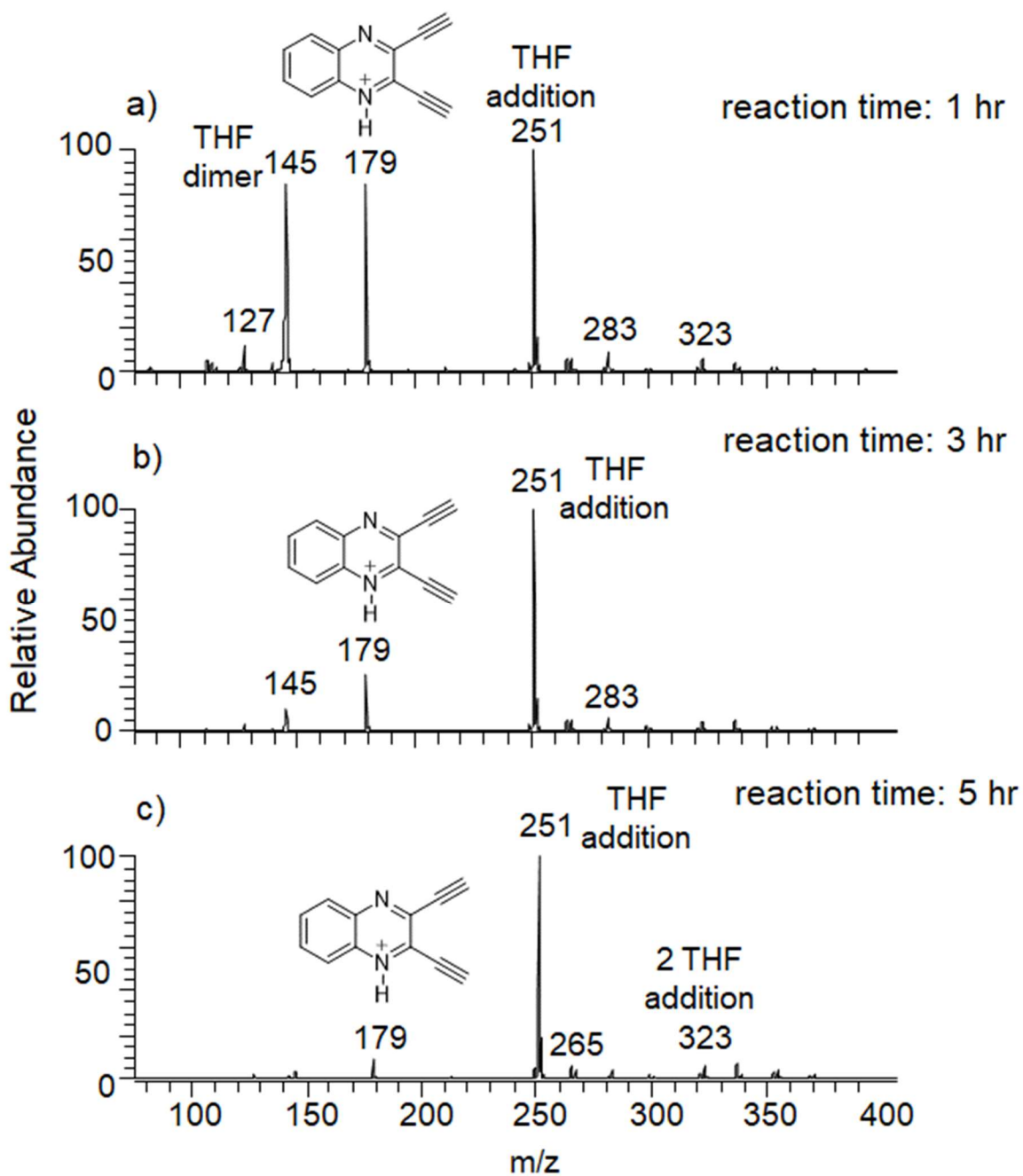
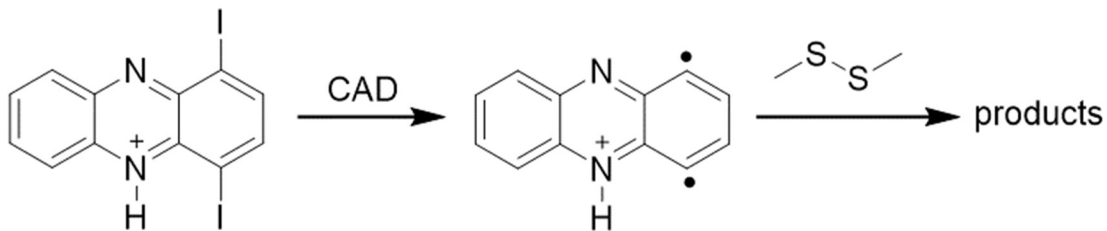


Figure 6.3 Figure showing mass spectra measured for thermally induced (60 °C) Bergman cyclization of 2,3-diethynylquinoxaline in presence of THF after a) 1 hour, b) 3 hours and c) 5 hours

### 6.3.2 Reactivity of para-Benzyne Toward Dimethyldisulfide in the Gas phase and in Solution



Scheme 6.5 Generation of protonated 1,4-didehydrophenazine by CAD followed by ion-molecule reactions with dimethyldisulfide in the gas phase

Protonated 1,4-didehydrophenazine was generated using two successive CAD events on protonated 1,4-diiiodophenazine. The biradical was isolated and allowed to react with DMDS for various reaction times. **Figure 6.4** shows the mass spectra recorded after 1 s and 10 s reactions. As shown in **Figure 6.4**, product corresponding to 2-thiomethyl abstraction ( $m/z$  273) was the major product. It is noteworthy that product corresponding to two SCH<sub>3</sub> abstraction is a secondary reaction product of mono-SCH<sub>3</sub> abstraction product ( $m/z$  226). The efficiency for the total reaction was measured to be 35 %. Water addition products ( $m/z$  197) from residual moisture in the trap were also observed.

DMDS is known to undergo thermal decomposition.<sup>42</sup> Hence, experiments leading to heat-induced Bergman cyclization of 2,3-diethynylquinoxaline were not performed. Photon-induced Bergman cyclization of 2,3-diethynylquinoxaline in the presence of DMDS were performed using UV irradiation at 253 nm for 45 mins (**Scheme 6.6**). The products were ionized using positive mode APCI. The mass spectra recorded for irradiated DMDS experiments, dark control experiments and irradiated reaction mixture containing 2,3-diethynylquinoxaline in DMDS are shown in **Figure 6.5**. As shown in **Figure 6.5 c** and **Figure 6.4**, product corresponding to abstraction of two SCH<sub>3</sub> groups was the major product obtained both in the gas phase and in solution. This finding indicated similar reactivities for protonated 1,4-didehydrophenazine biradical in the gas phase and for the neutral 1,4-didehydrophenazine (generated by photon-induced Bergman cyclization) towards DMDS in solution.

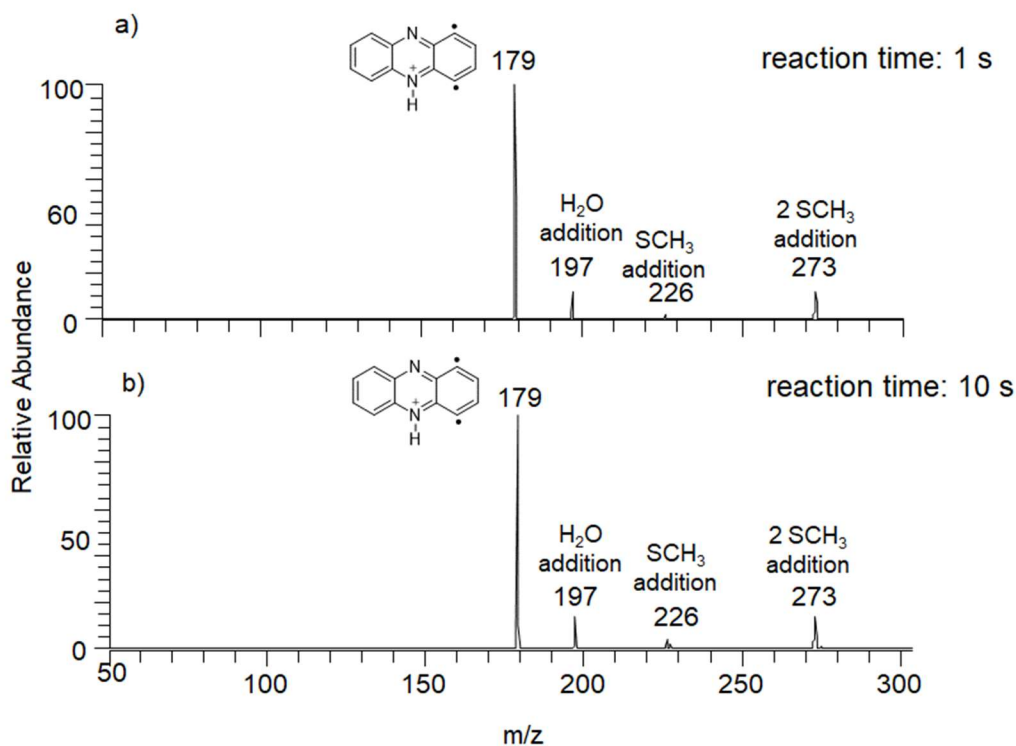
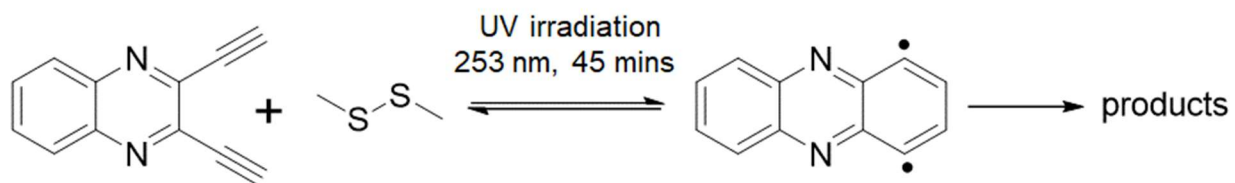


Figure 6.4 Mass spectra measured after protonated 1,4-didehydrophenazine biradical was allowed to react with dimethyldisulfide for a) 1 s and b) 10 s in the gas phase



Scheme 6.6 Generation of 1,4-didehydrophenazine by photon-induced Bergman cyclization of 2,3-diethynylquinoxaline induced by UV irradiation at 253 nm for 45 mins in the presence of DMDS.

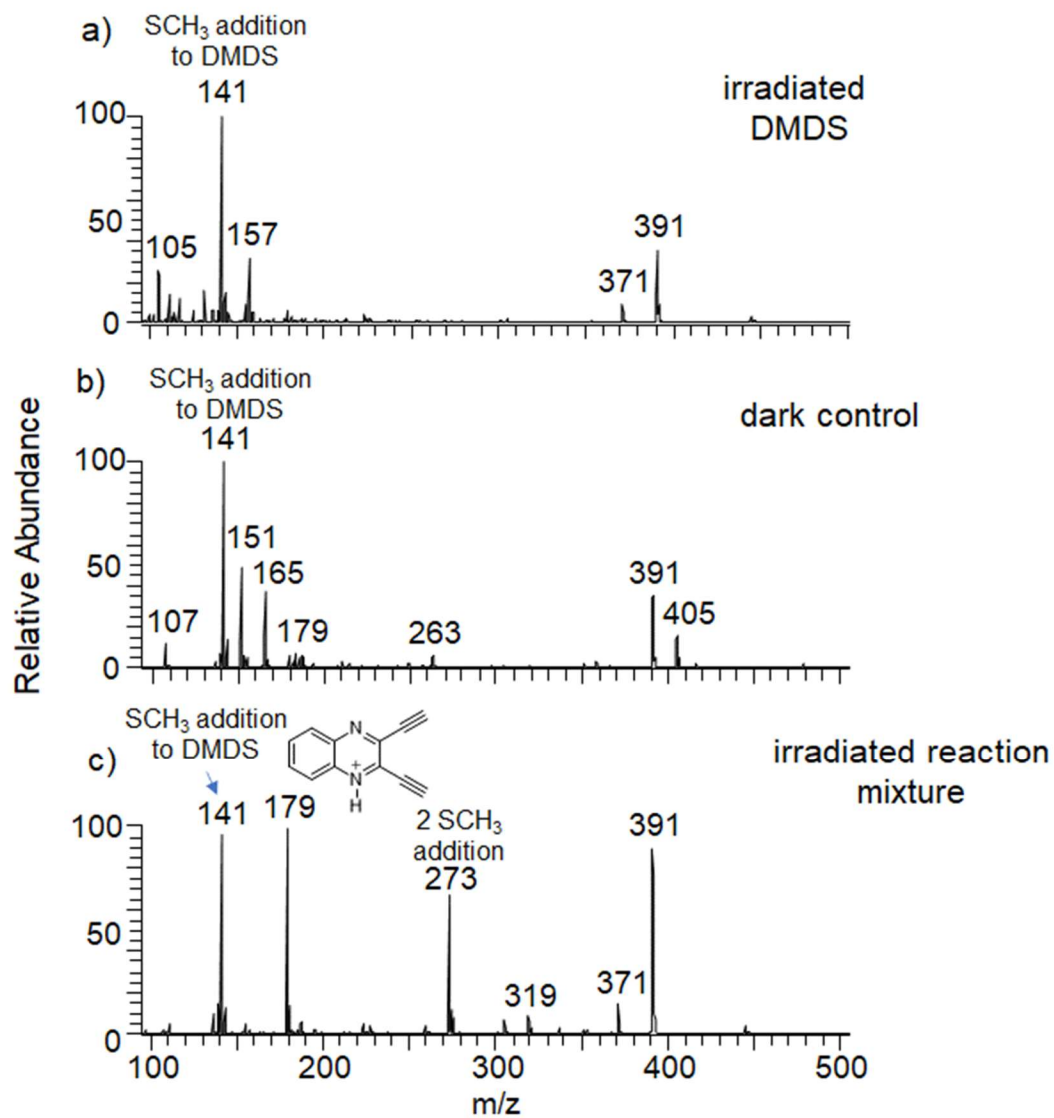
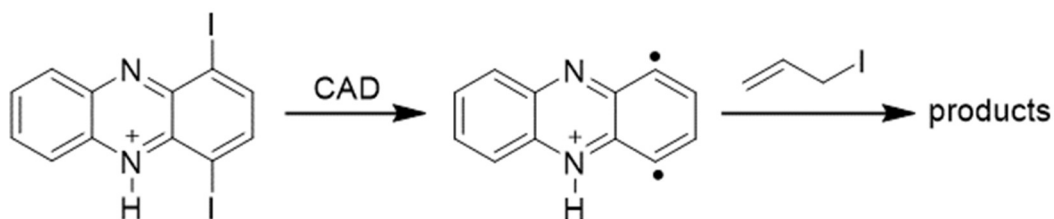


Figure 6.5 Figure showing mass spectra measured a) after DMDS was irradiated for 45 mins, b) in dark control experiments and c) after 2,3-diethynylquinoxaline was subjected to photon-induced Bergman cyclization induced using an UV irradiation of 253 nm for 45 mins in the presence of DMDS

### 6.3.3 Reactivity of para-Benzynes Toward Allyl Iodide in the Gas Phase and in Solution



Scheme 6.7 Generation of protonated 1,4-didehydrophenazine by CAD of protonated 1,4-diiodopyridine followed by ion-molecule reactions with allyl iodide

Protonated 1,4-diiodophenazine was isolated in the ion trap and subjected to two successive CAD events to generate protonated 1,4-didehydrophenazine biradical which was isolated and allowed to react with AI for varying reaction times. The mass spectra recorded after 5 s and 10 s are shown in **Figure 6.6**. As shown in **Figure 6.6**, the major reaction observed was allyl iodide addition to protonated 1,4-didehydrophenazine whereas product ions corresponding to abstraction of two iodine atoms were also formed, albeit slowly. The efficiency of the reaction was measured to be 14 %.

1,4-Didehydrophenazine biradical was also generated by photon-induced and heat-induced Bergman cyclization of 2,3-diethynylquinoxaline in the presence of allyliodide. In the case of photon-induced Bergman cyclization, a solution containing 2,3-diethynylquinoxaline and allyliodide was irradiated with UV light at 253 nm wavelength at 15 °C for 30 mins (**Scheme 6.6**). A solution containing neat allyl iodide was also irradiated. ‘Dark control’ experiments were also performed. The mass spectra recorded are shown in **Figure 6.7**. As shown in **Figure 6.7c**, the major product ion ( $m/z$  433) corresponds to abstraction of two iodine atoms which is an indication of successful generation of the biradical by photon-induced Bergman cyclization in solution. Product ion ( $m/z$  687) corresponding to abstraction of four iodine atoms was also observed. However, CAD studies (**Figure 6.8**) indicate that ion of  $m/z$  687 is a weakly bonded I<sub>2</sub> adduct of the product ion with  $m/z$  433. Heat-induced Bergman cyclization of 2,3-diethynylquinoxaline was carried out by heating a mixture of 2,3-diethynylquinoxaline and allyl iodide at 60 °C for 12 hours (**Scheme 6.6**). Aliquots of the reaction mixture were withdrawn every hour and analyzed. Mass spectra recorded at three different reaction times are shown in **Figure 6.9**.

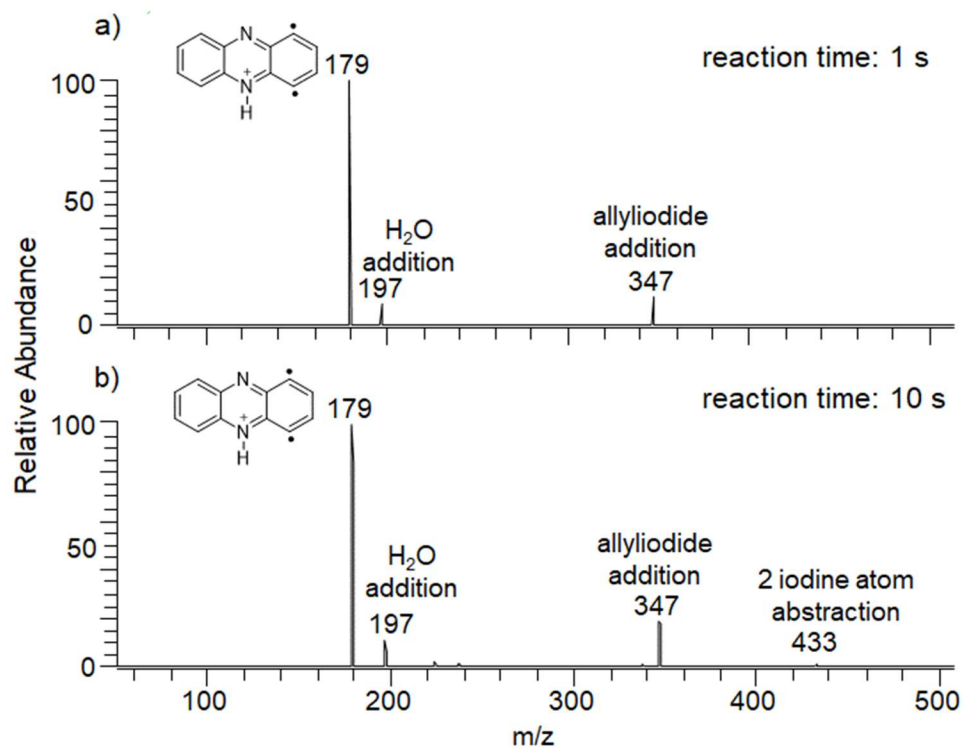
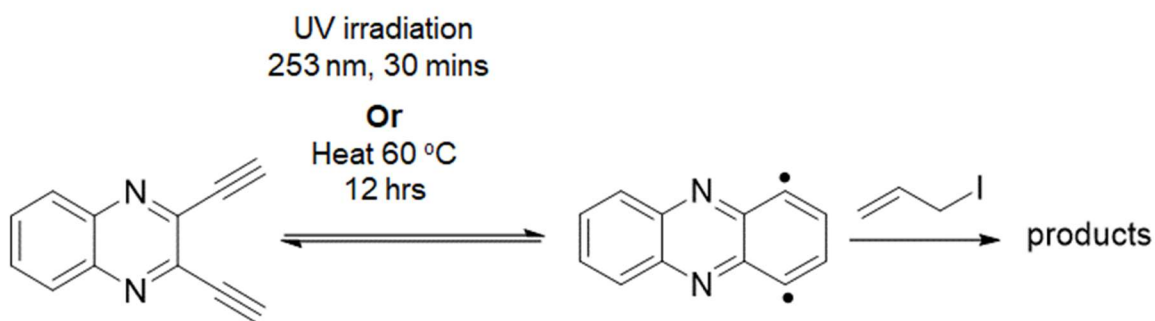


Figure 6.6 Mass spectra measured after protonated 1,4-didehydrophenazine biradical was allowed to react with allyl iodide for a) 1 s and b) 10 s in the gas phase



Scheme 6.8 Generation of 1,4-didehydrophenazine by photon-induced and heat-induced Bergman cyclization of 2,3-diethynylquinoxaline in the presence of allyl iodide

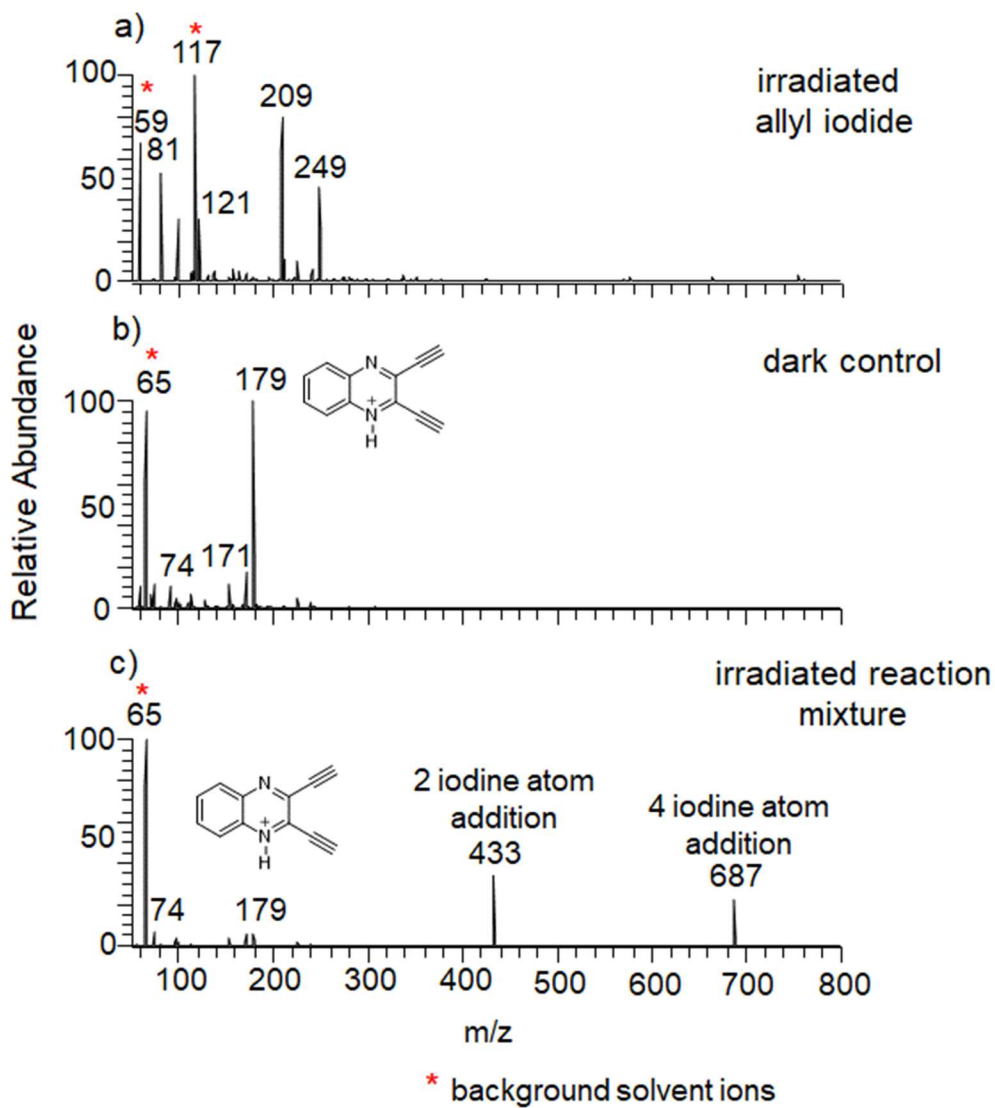


Figure 6.7 Figure showing mass spectra measured a) after allyl iodide was irradiated for 30 mins, b) in dark control experiments and c) after 2,3-diethynylquinoxaline was subjected to photon-induced Bergman cyclization induced using UV irradiation of 253 nm for 30 mins in the presence of allyl iodide

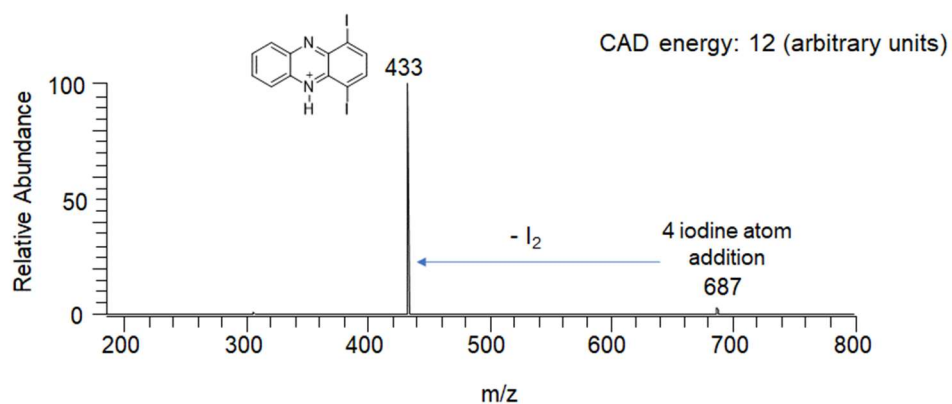


Figure 6.8 Mass spectra measured after product ion of  $m/z$  687 was subjected to CAD at a collision energy of 12 (arbitrary units)

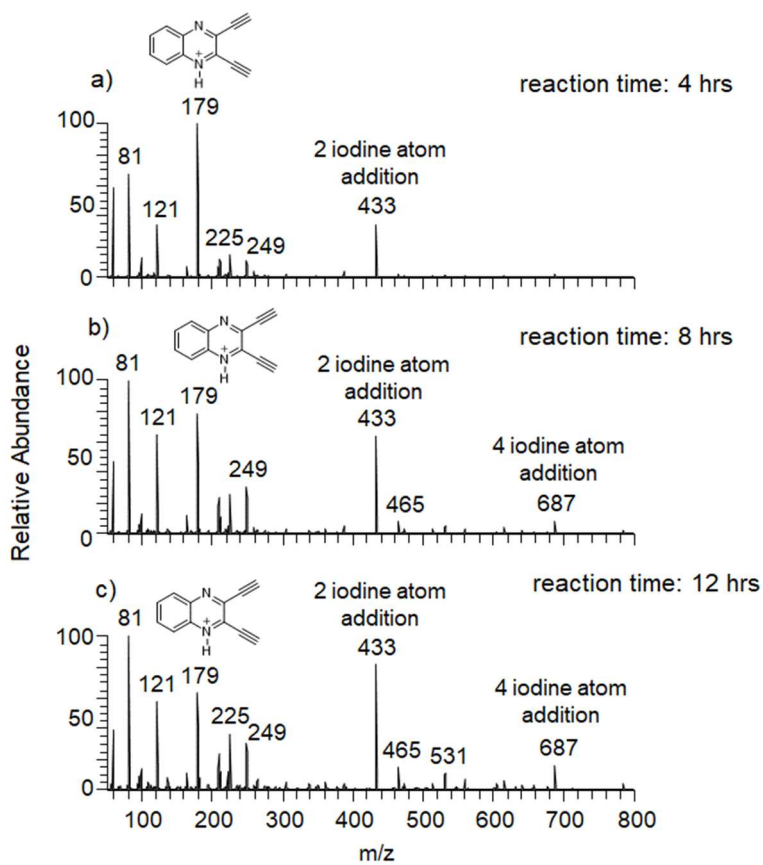
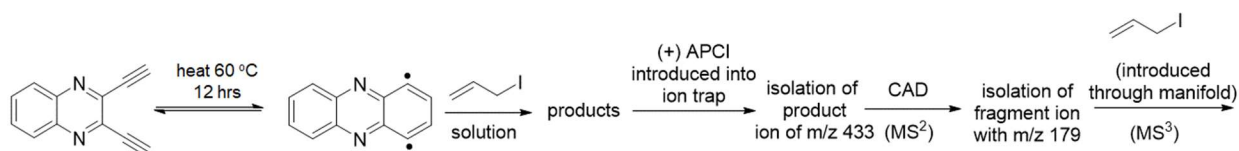


Figure 6.9 Figure showing mass spectra measured after heat-induced ( $60\text{ }^{\circ}\text{C}$ ) Bergman cyclization of 2,3-diethynylquinoxaline in the presence of allyl iodide after a) 4 hours, b) 8 hours and c) 12 hours.

As shown in **Figure 6.9**, the major product formed after heat-induced Bergman cyclization of 2,3-diethynylquinoxaline in solution corresponds to addition of two iodine atoms ( $m/z$  433). Product corresponding to abstraction of four iodine atoms ( $m/z$  687) was also formed. However, CAD experiments suggest that ion with  $m/z$  687 is an  $I_2$  adduct of ion of  $m/z$  433. It is noteworthy that in solution after photon-induced and heat-induced Bergman cyclization reactions, the major reaction was abstraction of 2 iodine atoms (**Figures 6.7 and 6.9**) whereas in the gas phase, the major reaction was addition of allyl iodide. The structure of the product ion of  $m/z$  433 (**Figure 6.7 and 6.9**) was verified by gas-phase ion-molecule reactions with allyl iodide. A solution containing the reaction mixture after heat-induced Bergman cyclization of 2,3-diethynylquinoxaline was introduced into the LQIT. Product ions corresponding to abstraction of two iodine atoms ( $m/z$  433) were isolated and subjected to CAD (**Scheme 6.7**) ( $MS^2$ ).  $MS^2$  spectra recorded showed that the ion  $m/z$  433 lost one iodine atom and two iodine atoms upon CAD (**Figure 6.10 a**). The fragment ions corresponding to the loss of two iodine atoms were isolated ( $MS^3$ ) and allowed to react with allyl iodide. The mass spectra recorded after 10 s is shown in **Figure 6.10 b**. Allyl iodide addition was observed to be the major reaction, which is similar to the reactivity of protonated 1,4-didehydrophenazine biradical in the gas phase.



Scheme 6.9 Ionization of products of heat-induced Bergman cyclization of 2,3-diethynylquinoxaline, followed by isolation of product ion of  $m/z$  433. The isolated ion ( $m/z$  433) was then fragmented using CAD, followed by isolation of fragment ion of  $m/z$  179. The isolated ion ( $m/z$  179) was then allowed to react with allyl iodide.

The mass spectra shown in **Figure 6.10 b** indicate formation of allyl iodide addition products to ion with  $m/z$  179, similar to the gas-phase reactivity of 1,4-didehydrophenazine with allyl iodide (**Figure 6.6**). This finding confirms that the structure of the product ion of  $m/z$  179 is the same as that of protonated 1,4-didehydrophenazine. This evidence suggests that the Bergman cyclization of 2,3-diethynylquinoxaline was successful under the current experimental conditions

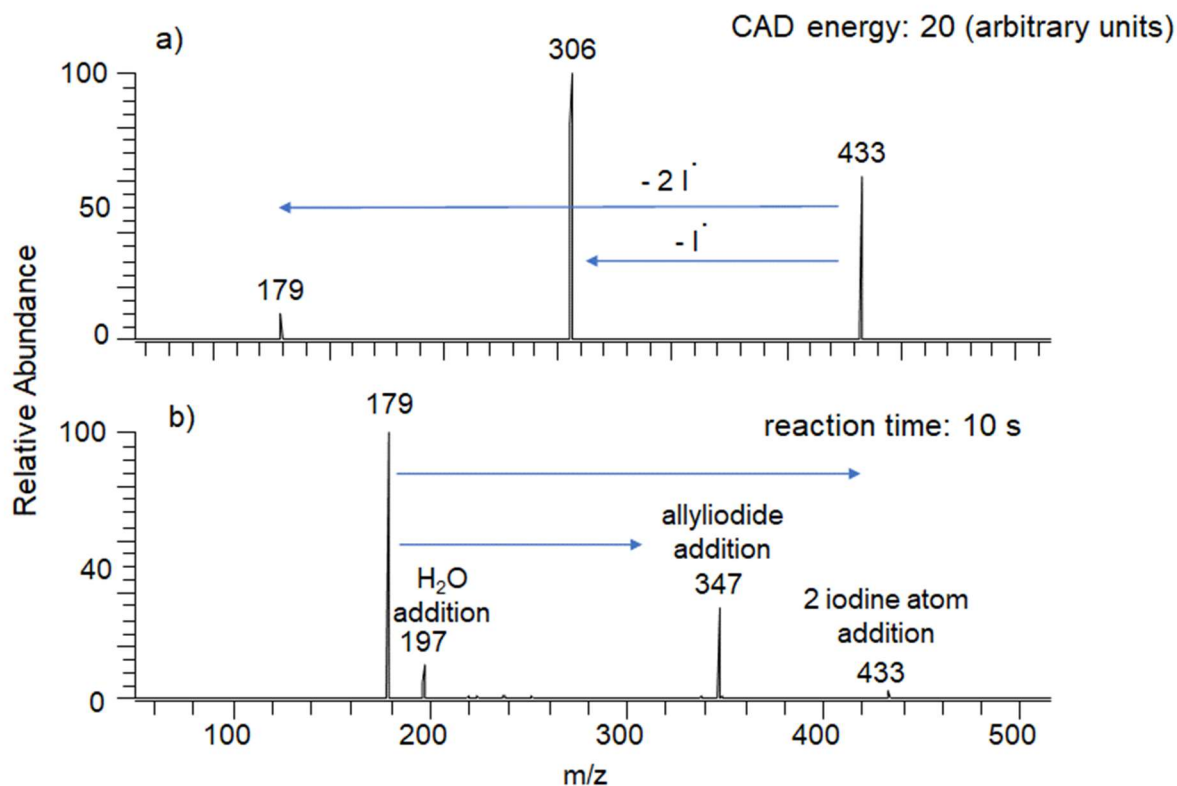


Figure 6.10. a) Figure showing mass spectra after product ion of  $m/z$  433 obtained upon heat-induced Bergman cyclization of 2,3-diethynylquinoxaline in the presence of allyl iodide was subjected to CAD. b) Mass spectrum measured after fragment ion of  $m/z$  179 was isolated and allowed to react with allyl iodide for 10 s in the ion trap.

## 6.4 Conclusions

A *para*-benzyne analog (1,4-didehydrophenazine) was successfully generated in solution using both photon-induced and heat-induced Bergman cyclization. Reactivity of protonated 1,4-didehydrophenazine biradical towards THF and DMDS in the gas phase is similar to the reactivity of neutral 1,4-dehydrophenazine towards the same reagents in solution. In contrast, protonated 1,4-didehydrophenazine biradical reacts with allyl iodide in the gas phase to form an addition product whereas 1,4-dehydrophenazine generated via Bergman cyclization reacted with allyl iodide in solution by predominant abstraction of two iodine atoms. Further fragmentation experiments on the product and additional gas-phase ion-molecule reactions support the successful generation of a *para*-benzyne (1,4-didehydrophenazine) via photon-induced and heat-induced Bergman cyclization of 2,3-diethynylquinoxaline in solution. Further, this study indicates that the

as-phase ion-molecule reactions of radical cations studied so far can be used to predict the reactivities of the corresponding neutral radical species in solution.

## 6.5 References

- (1) Zein, N.; Sinha, A. M.; McGahren, W. J.; Ellestad, G. A. Calicheamicin Gamma II: An Antitumor Antibiotic That Cleaves Double-Stranded DNA Site Specifically. *Science* **1988**, *240* (4856), 1198–1201. <https://doi.org/10.1126/science.3240341>.
- (2) Konishi, M.; Ohkuma, H.; Matsumoto, K.; Tsuno, T.; Kamei, H.; Miyaki, T.; Oki, T.; Kawaguchi, H.; Vanduyne, G. D.; Clardy, J. Dynemicin A, A Novel Antibiotic with the Anthraquinone and 1, 5-Diyn-3-ene Subunit. *J. Antibiot. (Tokyo)* **1989**, *42* (9), 1449–1452. <https://doi.org/10.7164/antibiotics.42.1449>.
- (3) Nicolaou, K. C.; Dai, W.-M. Chemistry and Biology of the Eneidyne Anticancer Antibiotics. *Angew. Chem. Int. Ed. Engl.* **1991**, *30* (11), 1387–1416. <https://doi.org/10.1002/anie.199113873>.
- (4) Bergman, R. G. Reactive 1,4-Dehydroaromatics. *Acc. Chem. Res.* **1973**, *6* (1), 25–31. <https://doi.org/10.1021/ar50061a004>.
- (5) Pratviel, G.; Bernadou, J.; Meunier, B. Carbon—Hydrogen Bonds of DNA Sugar Units as Targets for Chemical Nucleases and Drugs. *Angew. Chem. Int. Ed. Engl.* **1995**, *34* (7), 746–769. <https://doi.org/10.1002/anie.199507461>.
- (6) Song, D.; Sun, S.; Tian, Y.; Huang, S.; Ding, Y.; Yuan, Y.; Hu, A. Maleimide-Based Acyclic Eneidyne for Efficient DNA-Cleavage and Tumor Cell Suppression. *J. Mater. Chem. B* **2015**, *3* (16), 3195–3200. <https://doi.org/10.1039/C4TB02018A>.
- (7) Beerman, T. A.; Gawron, L. S.; Shin, S.; Shen, B.; McHugh, M. M. C-1027, A Radiomimetic Eneidyne Anticancer Drug, Preferentially Targets Hypoxic Cells. *Cancer Res.* **2009**, *69* (2), 593–598. <https://doi.org/10.1158/0008-5472.CAN-08-2753>.
- (8) Kennedy, D. R.; Ju, J.; Shen, B.; Beerman, T. A. Designer Eneidynes Generate DNA Breaks, Interstrand Cross-Links, or Both, with Concomitant Changes in the Regulation of DNA Damage Responses. *Proc. Natl. Acad. Sci. U. S. A.* **2007**, *104* (45), 17632–17637. <https://doi.org/10.1073/pnas.0708274104>.
- (9) Shen, B.; Hindra, null; Yan, X.; Huang, T.; Ge, H.; Yang, D.; Teng, Q.; Rudolf, J. D.; Lohman, J. R. Eneidynes: Exploration of Microbial Genomics to Discover New Anticancer Drug Leads. *Bioorg. Med. Chem. Lett.* **2015**, *25* (1), 9–15. <https://doi.org/10.1016/j.bmcl.2014.11.019>.
- (10) Perrin, C. L.; Reyes-Rodríguez, G. J. Reactivity of Nucleophiles toward a *p*-Benzyne Derived from an Eneidyne: Reactivity of Nucleophiles Toward A *p*-Benzyne Derived from an Eneidyne. *J. Phys. Org. Chem.* **2013**, *26* (2), 206–210. <https://doi.org/10.1002/poc.2994>.

- (11) Perrin, C. L.; Rodgers, B. L.; O'Connor, J. M. Nucleophilic Addition to a *p*-Benzyne Derived from an Eneidyne: A New Mechanism for Halide Incorporation into Biomolecules. *J. Am. Chem. Soc.* **2007**, *129* (15), 4795–4799. <https://doi.org/10.1021/ja070023e>.
- (12) Evenzahav, A.; Turro, N. J. Photochemical Rearrangement of Eneidyne: Is a “Photo-Bergman” Cyclization a Possibility? *J. Am. Chem. Soc.* **1998**, *120* (8), 1835–1841. <https://doi.org/10.1021/ja9722943>.
- (13) Kraka, E.; Cremer, D. Computer Design of Anticancer Drugs. A New Eneidyne Warhead. *J. Am. Chem. Soc.* **2000**, *122* (34), 8245–8264. <https://doi.org/10.1021/ja001017k>.
- (14) Spence, J. D.; Rios, A. C.; Frost, M. A.; McCutcheon, C. M.; Cox, C. D.; Chavez, S.; Fernandez, R.; Gherman, B. F. Syntheses, Thermal Reactivities, and Computational Studies of Aryl-Fused Quinoxalenediynes: Effect of Extended Benzannulation on Bergman Cyclization Energetics. *J. Org. Chem.* **2012**, *77* (22), 10329–10339. <https://doi.org/10.1021/jo302009c>.
- (15) Alabugin, I. V.; Kovalenko, S. V. C1–C5 Photochemical Cyclization of Eneidyne. *J. Am. Chem. Soc.* **2002**, *124* (31), 9052–9053. <https://doi.org/10.1021/ja026630d>.
- (16) Kim, C.-S.; Russell, K. C. Solvent Dependent Bergman Cyclization of 2,3-Diethynylquinoxaline. *Tet. Lett.* **1999**, *40* (20), 3835–3838. [https://doi.org/10.1016/S0040-4039\(99\)00634-6](https://doi.org/10.1016/S0040-4039(99)00634-6).
- (17) Kar, M.; Basak, A.; Bhattacharjee, M. Photoisomerization as a Trigger for Bergman Cyclization: Synthesis and Reactivity of Azoenediynes. *Bioorg. Med. Chem. Lett.* **2005**, *15* (24), 5392–5396. <https://doi.org/10.1016/j.bmcl.2005.09.005>.
- (18) Nicolaou, K. C.; Smith, A. L. Molecular Design, Chemical Synthesis, and Biological Action of Eneidyne. *Acc. Chem. Res.* **1992**, *25* (11), 497–503. <https://doi.org/10.1021/ar00023a003>.
- (19) Uesawa, Y.; Kuwahara, J.; Sugiura, Y. Light-Induced DNA Cleavage by Esperamicin and Neocarzinostatin. *Biochem. Biophys. Res. Commun.* **1989**, *164* (2), 903–911. [https://doi.org/10.1016/0006-291X\(89\)91544-1](https://doi.org/10.1016/0006-291X(89)91544-1).
- (20) Kagan, J.; Wang, X.; Chen, X.; Lau, K. Y.; Batac, I. V.; Tuveson, R. W.; Hudson, J. B. DNA Cleavage, Antiviral and Cytotoxic Reactions Photosensitized by Simple Eneidyne Compounds. *J. Photochem. Photobiol. B* **1993**, *21* (2), 135–142. [https://doi.org/10.1016/1011-1344\(93\)80175-9](https://doi.org/10.1016/1011-1344(93)80175-9).
- (21) Poloukhine, A.; Popik, V. V. Two-Photon Photochemical Generation of Reactive Eneidyne. *J. Org. Chem.* **2006**, *71* (19), 7417–7421. <https://doi.org/10.1021/jo061285m>.
- (22) Kauffman, J. F.; Turner, J. M.; Alabugin, I. V.; Breiner, B.; Kovalenko, S. V.; Badaeva, E. A.; Masunov, A.; Tretiak, S. Two-Photon Excitation of Substituted Eneidyne. *J. Phys. Chem. A* **2006**, *110* (1), 241–251. <https://doi.org/10.1021/jp056127y>.

- (23) Polukhtine, A.; Popik, G. K. and V. V. Towards Photoswitchable Eneidyne Antibiotics: Single and Two-Photon Triggering of Bergman Cyclization <http://www.eurekaselect.com/82479/article> (accessed Apr 22, 2020).
- (24) Grissom, J. W.; Calkins, T. L.; McMillen, H. A.; Jiang, Y. Determination of the Activation Parameters for the Bergman Cyclization of Aromatic Eneidyne. *J. Org. Chem.* **1994**, *59* (19), 5833–5835. <https://doi.org/10.1021/jo00098a055>.
- (25) Alabugin, I. V.; Manoharan, M.; Kovalenko, S. V. Tuning Rate of the Bergman Cyclization of Benzannelated Eneidyne with ortho Substituents. *Org. Lett.* **2002**, *4* (7), 1119–1122. <https://doi.org/10.1021/ol0255054>.
- (26) Nicolaou, K. C.; Ogawa, Y.; Zuccarello, G.; Schweiger, E. J.; Kumazawa, T. Cyclic Conjugated Eneidyne Related to Calicheamicins and Esperamicins: Calculations, Synthesis, and Properties. *J. Am. Chem. Soc.* **1988**, *110* (14), 4866–4868. <https://doi.org/10.1021/ja00222a077>.
- (27) Nath, M.; Pink, M.; Zaleski, J. M. Controlling Both Ground- and Excited-State Thermal Barriers to Bergman Cyclization with Alkyne Termini Substitution. *J. Am. Chem. Soc.* **2005**, *127* (2), 478–479. <https://doi.org/10.1021/ja045979t>.
- (28) Prall, M.; Wittkopp, A.; Fokin, A. A.; Schreiner, P. R. Substituent Effects on the Bergman Cyclization of (Z)-1,5-Hexadiyne-3-Enes: A Systematic Computational Study. *J. Comput. Chem.* **2001**, *22* (13), 1605–1614. <https://doi.org/10.1002/jcc.1114>.
- (29) Jones, G. B.; Warner, P. M. Electronic Control of the Bergman Cyclization: The Remarkable Role of Vinyl Substitution. *J. Am. Chem. Soc.* **2001**, *123* (10), 2134–2145. <https://doi.org/10.1021/ja0033032>.
- (30) Schmittel, M.; Kiau, S. Polar Effects in the Transition State of the Bergman Cyclization. *Chem. Lett.* **1995**, *24* (10), 953–954. <https://doi.org/10.1246/cl.1995.953>.
- (31) Zhao, Z.; Peacock, J. G.; Gubler, D. A.; Peterson, M. A. Photoinduced Bergman Cycloaromatization of Imidazole-Fused Eneidyne. *Tetrahedron Lett.* **2005**, *46* (8), 1373–1375. <https://doi.org/10.1016/j.tetlet.2004.12.136>.
- (32) Pandithavidana, D. R.; Poloukhine, A.; Popik, V. V.; Photochemical Generation and Reversible Cycloaromatization of a Nine-Membered Ring Cyclic Eneidyne *J. Am. Chem. Soc.* **2009**, *131* (1), 351-356.
- (33) Alabugin, I. V.; Manoharan, M. Reactant Destabilization in the Bergman Cyclization and Rational Design of Light- and PH-Activated Eneidyne. *J. Phys. Chem. A* **2003**, *107* (18), 3363–3371. <https://doi.org/10.1021/jp026754c>.
- (34) Kaneko, T.; Takahashi, M.; Hirama, M. Photochemical Cycloaromatization of Non-Benzenoid Eneidyne. *Angew. Chem. Int. Ed.* **1999**, *38* (9), 1267–1268.

- (35) Adeuya, A.; Price, J. M.; Jankiewicz, B. J.; Nash, J. J.; Kenttamaa, H. I. Gas-Phase Reactivity of Protonated 2-, 3-, and 4-Dehydropyridine Radicals Toward Organic Reagents. *J Phys Chem A*. **2009**, *113* (49), 13663-13674
- (36) Jankiewicz, B. J.; Adeuya, A.; Yurkovich, M. J.; Vinueza, N. R.; Gardner, S. J.; Zhou, M.; Nash, J. J.; Kenttamaa, H. I. Reactivity of an Aromatic  $\sigma,\sigma,\sigma$ -Triradical: The 2,4,6-Tridehydropyridinium Cation. *Angew. Chem.* *119* (48), 9358–9361. <https://doi.org/10.1002/ange.200701732>.
- (37) Tsubata, Y.; Suzuki, T.; Miyashi, T.; Yamashita, Y. Single-Component Organic Conductors Based on Neutral Radicals Containing the Pyrazino-TCNQ Skeleton. *J. Org. Chem.* **1992**, *57* (25), 6749–6755. <https://doi.org/10.1021/jo00051a015>.
- (38) Kim, C.-S.; Russell, K. C. Rapid Bergman Cyclization of 1,2-Diethynylheteroarenes. *J. Org. Chem.* **1998**, *63* (23), 8229–8234. <https://doi.org/10.1021/jo980879p>.
- (39) Gronert, S. Mass Spectrometric Studies of Organic Ion/Molecule Reactions. *Chem. Rev.* **2001**, *101* (2), 329–360. <https://doi.org/10.1021/cr9900836>.
- (40) Gronert, S. Quadrupole Ion Trap Studies of Fundamental Organic Reactions. *Mass Spectrom. Rev.* **2005**, *24* (1), 100–120. <https://doi.org/10.1002/mas.20008>.
- (41) Habicht, S. C.; Vinueza, N. R.; Amundson, L. M.; Kenttamaa, H. I. Comparison of Functional Group Selective Ion–Molecule Reactions of Trimethyl Borate in Different Ion Trap Mass Spectrometers. *J. Am. Soc. Mass Spectrom.* **2011**, *22* (3), 520–530. <https://doi.org/10.1007/s13361-010-0050-3>.
- (42) Vandeputte, A. G.; Reyniers, M.-F.; Marin, G. B. Theoretical Study of the Thermal Decomposition of Dimethyl Disulfide. *J. Phys. Chem. A* **2010**, *114* (39), 10531–10549. <https://doi.org/10.1021/jp103357z>.

## VITA

Rashmi Kumar was born in Kolkata, India. She completed her Bachelor of Science from Presidency College, Kolkata with major in Chemistry. After completing her undergraduate degree, she moved to Chennai, India to pursue Master of Science at Indian Institute of Technology, Madras. During her masters, she joined Dr. Sundarababu Baskaran's group to pursue research in organic chemistry synthesis. After completing her masters, she enrolled at Purdue Chemistry to pursue her doctoral degree.

## PUBLICATIONS

**Effects of Residual Water in a Linear Quadrupole Ion Trap on the Protonation Sites of 4-Aminobenzoic Acid; *Rashmi Kumar, Ravikiran Yerabolu, Hilkka I. Kenttämää\** Journal of the American Society for Mass Spectrometry 2020, (31), 124-131**

**Measurements of the Proton Affinities of a Series of Mono- and Biradicals of Pyridine, *Rashmi Kumar, Guannan Li, Vanessa A. Gallardo, Anyin Li, Jacob Milton, John J. Nash, Hilkka I. Kenttämää\** Journal of the American Chemical Society; 2020, 142 (19), 8679–8687**

**The Effects of Analyte Concentration on the Protonation Sites of 4-Aminobenzoic Acid Upon Atmospheric Pressure Chemical Ionization as Revealed by Gas-phase Ion-molecule Reactions, *Rashmi Kumar, Hilkka I. Kenttämää\** (submitted)**

**Gas Phase Fragmentation of Adducts between Dioxygen and *closo*-Borate Radical Anions, *Jonas Warneke, \*, Markus Rohdenburg, Judy K.Y. Liu, Erynn Johnson, Xin Ma, Rashmi Kumar, Pei Su, Edoardo Aprà, Xue-Bin Wang, Carsten Jenne, Maik Finze, Hilkka I. Kenttämää, Julia Laskin; International Journal of Mass Spectrometry, 2019 (436), 71-78***

**Integration of a Multichannel Pulsed-Valve Inlet System to a Linear Quadrupole Ion Trap Mass Spectrometer for the Rapid Consecutive Introduction of Nine Reagents for Diagnostic Ion/Molecule Reactions, *John Y. Kong, Ryan T. Hilger, Chunfen Jin, Ravikiran Yerabolu, James R. Zimmerman, Randall W. Replogle, Tiffany M. Jarrell, Leah Easterling, Rashmi Kumar, Hilkka I. Kenttämää\** Analytical Chemistry, 2019 (91), 15652-15660**

**Factors Affecting the Limit of Detection for HPLC/Tandem Mass Spectrometry Experiments Based On Gas-phase Ion-molecule Reactions *Leah F. Easterling, Ravikiran Yerabolu, Rashmi Kumar, Kawthar ALzarieni, Hilkka I. Kenttämää* Analytical Chemistry, 2020, 92 (11), 7471-7477**